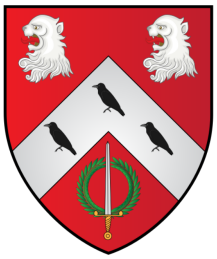


Ferromagnetism in Atomically Thin van der Waals Materials

Ryuji Hiro Fujita
St Anne's College



University of Oxford
A thesis presented for the degree of
Doctor of Philosophy

Michaelmas 2023

Copyright © 2023 by Ryuji Hiro Fujita
All Rights Reserved

Acknowledgements

Over the past several years, far-reaching effects incurred by a global pandemic have changed our daily lives. In the face of such challenges, I am both privileged and humbled to have been able to devote my time and energy to my DPhil within the Thin Film Quantum Materials group at the University of Oxford.

Firstly, I would like to thank my supervisor, Professor Thorsten Hesjedal, for mentoring me throughout my DPhil. Thorsten's enthusiasm and dedication for the topics discussed in my dissertation are unparalleled, and he consistently went out of his way to train and support me with numerous aspects of my research. I greatly look forward to continuing as a postdoc in his group.

I would like to thank Professor Gerrit van der Laan for suggesting the use of synchrotron radiation for my research, which has led to many fruitful results. Moreover, Gerrit has consistently provided me with invaluable feedback on the countless drafts of proposals and papers I prepared, and has also been my host at the Diamond Light Source for the past four years. Gerrit's support has enabled my research to an incalculable degree.

I would like to thank Dr. Florian Kronast, Dr. Mohammad A. Mawass, and Dr. Alevtina Smekhova at BESSY for their extensive support of the numerous projects which I have been involved in. Their enthusiasm and unparalleled expertise in XPEEM has resulted in several publications, and I greatly look forward to future XPEEM beamtimes at BESSY.

I would like to thank Dr. Michael Högen, Dr. Anthony K.C. Tan, and Professor Mete Atatüre at the University of Cambridge for performing NV magnetometry on numerous samples which I have prepared. Their initiative on several fronts has recently resulted in a publication, and I greatly look forward to continued collaborative work in the areas of NV magnetometry and 2D materials.

I would like to thank Dr. Matthew Watson, Dr. Timur Kim and Dr. Cephise Cacho at Diamond Light Source for allowing me to prepare samples for beamtimes inside of the glovebox at I05. I look forward to continued joint work, especially in ARPES measurements, as a postdoc for the next several years.

I would like to thank Dr. Jieyi Liu for his help and guidance regarding XAS and XMCD measurements. In particular, Jieyi helped me analyze the XMCD data of few-layer $CrSiTe_3$.

I would like to thank Mr. Jheng-Cyuan Lin for his invaluable help and expertise regarding XPEEM measurements and data analysis. In particular, JC provided much-needed assistance in the characterization of vortices and antivortices in Fe_5GeTe_2.

I would like to thank Professor Anjan Soumyanarayanan, Dr. Alexander Kang-Jun Toh, and Dr. Pin Ho at A*STAR and IMRE in Singapore for performing PFM measurements. Their contribution was instrumental in data interpretation and analysis, and will result in future publications.

I would like to thank Dr. Dirk Backes and Dr. Francesco Maccherozzi at Diamond Light Source for involving me in a variety of projects, and also for extensive assistance during beamtimes at I06.

I would like to thank Mr. Mark Sussmuth at Diamond Light Source for taking the time out of his schedule to help me with numerous construction projects and repairs for the glovebox. His attention to precision and detail motivated me to implement high standards in my own work.

I would like to thank Dr. Gautam Gurung at Trinity College, University of Oxford for performing DFT calculations in support of the experimental work I have done. His contribution was vital for a broader and comprehensive understanding of our results, and will result in future publications.

I would like to thank Dr. Zhengxian Li, Mr. Xiaofei Hou, and Professor Yanfeng Guo at ShanghaiTech University, Dr. Daniel Mayoh and Professor Geetha Balakrishnan at the University of Warwick, Dr. Andrew May at the Oak Ridge National Laboratory, Professor Jin Hu at the University of Arkansas, and Dr. Takashi Taniguchi and Dr. Kenji Watanabe at the National Institute of Materials Science in Tsukuba, Japan for taking the time out of their own schedules to provide me with high-quality crystals for my research. Their contributions have directly enabled my experimental research, and have resulted in several

publications or currently ongoing projects.

I would like to thank my partner, Yuting, for her unwavering support, despite her own professional commitments and hectic schedule. She has consistently put my needs before her own, and her selfless attitude motivates me to improve myself on a daily basis.

Finally, I would like to thank my parents for strongly encouraging me to study abroad, and for funding my studies in Oxford for the entire duration of my DPhil. They have single-handedly enabled the most transformative, rewarding and cherished experience I will have, and for that, I am most grateful.

Abstract

The characterization of two-dimensional materials, which have different properties compared to those of their bulk counterparts, has intensified in the last two decades. Moreover, the ability to stack atomically thin sheets into heterostructures is enabled by the van der Waals interaction, which weakly binds atomic layers together within a broader class of van der Waals materials. Fascinating two-dimensional physics, in addition to the relative ease of fabricating atomically thin van der Waals heterostructures of high structural quality, has arguably made two-dimensional materials the most studied area of condensed matter physics in recent years. Despite the rich physics, technical challenges will likely limit the implementation of two-dimensional materials to niche purposes, and will more generally obfuscate their incorporation in practical devices. Nevertheless, the integration of two-dimensional materials into nascent technologies such as quantum computing strongly motivate further characterization and subsequent device optimization.

The two-dimensional magnet is a relatively recent addition to the broader van der Waals class, consisting of two-dimensional semiconductors, ferroelectrics and superconductors. In particular, two-dimensional ferromagnetism is generally stabilized by a large magnetic anisotropy. This thesis examines if such an anisotropic magnetic state can be tuned in the atomically thin limit, and if other magnetic states exist in two dimensions.

Firstly, it is shown that ferromagnetism is fundamentally distinct in two dimensions compared to in the bulk. In detail, the magnetic orbital moment m_l and magnetic spin moment m_s are estimated for $CrSiTe_3$, a 2D Ising ferromagnet for which the magnetic exchange interaction is mostly limited to within the *ab* plane. An enhancement of the m_l/m_s ratio in atomically thin $CrSiTe_3$ demonstrates that even for a 2D Ising ferromagnet with limited interlayer interactions, dimensionality effects are non-negligible.

Secondly, a novel method of tuning the magnetic state in Fe_3GeTe_2, a van der Waals ferromagnet with a large unaxial anisotropy, is demonstrated. In partic-

ular, the inclusion of α-In_2Se_3, a van der Waals piezoelectric, is shown to strain Fe_3GeTe_2, resulting in a reduced critical temperature and domain wall energy. The straining of other van der Waals materials with α-In_2Se_3, including graphite, is also demonstrated.

Thirdly, a search for two-dimensional magnetic states with weak anisotropy is thoroughly discussed. In particular, magnetic domains are characterized in few-layer Fe_5GeTe_2, a van der Waals ferromagnet with a small unaxial anisotropy compared to its counterpart Fe_3GeTe_2. The observation of such domains in two-dimensional Fe_5GeTe_2 is counterintuitive, as the magnetic anisotropy energy is usually too large to accomodate domain walls. These domains, as well as deviations from the easy axis, are discussed in terms of different energetic quantities and domain wall pinning. It is concluded that for Fe_5GeTe_2, the magnetism is characterized by intercompetition among the magnetic anisotropy and stray field energy, meaning that it should be possible to stabilize magnetic domains with varying properties in the atomically thin limit.

Lastly, easy-plane ferromagnetism is considered for Fe_5GeTe_2. In detail, a temperature-induced magnetostructural transition is utilized to induce easy-plane magnetic anisotropy in Fe_5GeTe_2. In the atomically thin limit, magnetic domains with an in-plane orientation, as well as magnetic vortices and antivortices are observed. This is a significant finding which demonstrates the formation of spin textures in an atomically thin 2D material, potentially for the first time. Future work includes the characterization of the topological properties of these spin textures, as well as incorporating them in ferromagnet-superconductor van der Waals heterostructures to test proposals regarding the Majorana bound state, which holds relevance for quantum computing.

Table of Contents

1 Introduction to Two-Dimensional Materials and Ferromagnetism **1**

1.1 Background . . . 1
1.2 Two-dimensional Heisenberg model . . . 3
1.3 Mean field theory and critical exponents . . . 5
1.4 Mermin-Wagner theorem . . . 6
1.5 XY model and Berezenskii-Kosterlitz-Thouless theory . . . 6
1.6 Ferromagnetic domains and domain wall energy . . . 8
1.7 Ferromagnetic hysteresis . . . 8
1.8 Bloch and Néel-type type domain walls . . . 9
1.9 Thesis outline . . . 10

2 Methods **12**

2.1 Surface-sensitive microscopies . . . 12
2.2 Mechanical exfoliation . . . 12
2.3 Optical characterization . . . 14
2.4 Atomic force microscopy . . . 15
2.5 Raman microscopy . . . 17
2.6 X-ray magnetic circular dichroism . . . 19
2.6.1 Sum rule analysis . . . 19
2.7 X-ray photoelectron emission microscopy . . . 22
2.8 Nitrogen-vacancy center scanning magnetometry . . . 23

3 X-ray spectroscopy of atomically thin $CrSiTe_3$ **25**

3.1 $CrSiTe_3$: A quasi-two-dimensional ferromagnetic semiconductor 25
3.2 Methods . . . 26
3.2.1 Crystal growth and exfoliation of bulk $CrSiTe_3$ . . . 26
3.2.2 High-field X-ray magnetic circular dichroism . . . 26

3.3 Spatial mapping of large-scale exfoliated $CrSiTe_3$ . . . 27
3.4 Layer-dependent X-ray absorption spectroscopy and X-ray magnetic circular dichroism of atomically thin $CrSiTe_3$ . . . 28
3.5 Layer-dependent spin and orbital magnetic moments . . . 29
3.6 Layer-dependent ferromagnetic hysteresis . . . 31
3.7 Saturation magnetization and spin moment . . . 34
3.8 Orbital to spin moment ratio . . . 34
3.9 Conclusion . . . 35

4 Strained ferromagnetism at a Fe_3GeTe_2/α-In_2Se_3 heterojunction 36
4.1 Magnetism in bulk and two-dimensional Fe_3GeTe_2 . . . 36
4.2 Strain-tuning of two-dimensional materials . . . 36
4.3 Methods . . . 37
4.3.1 Single crystal growth . . . 37
4.3.2 Mechanical exfoliation . . . 38
4.3.3 Piezoresponse force microscopy characterization of a α-In_2Se_3 heterojunction . . . 38
4.3.3.1 Instrumentation and setup . . . 38
4.3.3.2 Measurement procedures . . . 38
4.3.4 Raman characterization of α-In_2Se_3 heterojunctions . . . 39
4.3.5 Density functional theory calculations of effective exchange interaction, uniaxial anisotropy, Curie temperature and lattice parameter . . . 39
4.4 Magnetic domain structure in a Fe_3GeTe_2/α-In_2Se_3 heterojunction 40
4.5 Reduction of ferromagnetic Curie temperature in a Fe_3GeTe_2/α-In_2Se_3 heterojunction . . . 43

4.6 Density functional theory calculations of effective exchange interaction, uniaxial anisotropy and estimation of ferromagnetic Curie temperature for varying lattice parameter . . . 45
4.7 Enhancement of magnetic coercivity in a Fe_3GeTe_2/α-In_2Se_3 heterojunction . . . 46
4.8 Interfacial strain in α-In_2Se_3 heterojunctions . . . 47
4.9 Magnetostriction effects in a Fe_3GeTe_2/α-In_2Se_3 heterojunction 52
4.10 Conclusion . . . 56

5 Layer-dependent magnetic domains in atomically thin Fe_5GeTe_2 57
5.1 Fe_5GeTe_2: a weak-anisotropy van der Waals ferromagnet with high Curie temperature . . . 57
5.2 Synthesis and preliminary characterization of few-layer Fe_5GeTe_2 58
5.3 X-ray photoelectron emission microscopy characterization of Fe_5GeTe_2 . . . 60
5.3.1 Ferromagnetic domains in bulk Fe_5GeTe_2 . . . 60
5.3.2 Ferromagnetic domains in atomically thin Fe_5GeTe_2 . . 64
5.4 Nitrogen-vacancy center scanning magnetometry study of domain pinning in few-layer Fe_5GeTe_2 . . . 72
5.5 Defects and magnetism in atomically thin Fe_5GeTe_2 . . . 79
5.6 Spin Reorientation in 5 L and 6 L Fe_5GeTe_2 . . . 84
5.7 Conclusion . . . 85

6 Vortex-antivortex pairs in atomically thin Fe_5GeTe_2 86
6.1 Easy-plane ferromagnetism in Fe_5GeTe_2 . . . 86
6.2 Vortices in magnetic systems . . . 87
6.3 Methods . . . 88
6.3.1 Bulk sample characterization . . . 88

6.3.2 Exfoliation of atomically thin Fe_5GeTe_2 89
6.4 Vector imaging of vortex-antivortex pairs in 4 L Fe_5GeTe_2 90
6.4.1 Vortex-antivortex formation in 4 L Fe_5GeTe_2 92
6.4.2 Localized vortex-antivortex pairs in 4 L Fe_5GeTe_2 95
6.4.3 Helicity variations in vortex-antivortex pairs 101
6.5 Conclusion 104

7 Conclusions and outlook **106**
7.1 Summary of results 106
7.2 Outlook and perspective 109

List of Abbreviations

2D: Two-dimensional

1 L, 2 L, 3 L, etc.: Monolayer, bilayer, trilayer, etc.

σ_{w}: Domain wall energy

A: Exchange stiffness

AFM: Atomic force microscopy

BKT: Berezenskii-Kosterlitz-Thouless

CVT: Chemical vapor transport

D: Dimensionality of the order parameter

DFT: Density functional theory

DMI: Dzyaloshinskii-Moriya interaction

EDX: Energy-dispersive X-ray spectroscopy

H_{c}: Coercive field

H_{sat}: Saturation field

IP: In-plane

J: Exchange interaction

J_{ij}: Exchange interaction between i^{th} and j^{th} spins

$\vec{k}$: X-ray propagation vector

K_{d}: Demagnetization energy

K_{u}: Uniaxial magnetic anisotropy energy

LCP: Left circular polarization

$\vec{m}$: Magnetization vector

MFM: Magnetic force microscopy

m_l: Orbital magnetic moment

m_s: Spin magnetic moment

$\widetilde{M}_{\mathrm{sat}}$: Saturation magnetization

MTJ: Magnetic tunnel junction

n_h: Number of $3d$ holes

NQ: Non-quenched

NVSM: Nitrogen-vacancy center scanning magnetometry

OOP: Out-of-plane

PDMS: Polydimethylsiloxane

PFM: Piezoresponse force microscopy

PMA: Perpendicular magnetic anisotropy

ppm: Parts per million

QC: Quench-cooled

RCP: Right circular polarization

SQUID: Superconducting quantum interference device

T_{C}: Curie temperature

T_{KT}: Kosterlitz-Thouless transition

TMD: Transition metal dichalcogenide

UHV: Ultrahigh vacuum

vdW: van der Waals

w: Helicity

W_{d}: Domain wall width

XAS: X-ray absorption spectroscopy

XMCD: X-ray magnetic circular dichroism

XPEEM: X-ray photoemission electron microscopy

XRD: X-ray diffraction

Publications

1. A.S. Kumar, M.Y. Wang, Y.C. Li, R. Fujita, X.P.A. Gao. "Interfacial Charge Transfer and Gate-Induced Hysteresis in Monochalcogenide InSe/GaSe Heterostructures." *ACS Appl. Mater. Interfaces* **12**, 41 (2020)

2. D.M. Burn, L.B. Duffy, R. Fujita, S.L. Zhang, A.I. Figueroa, J. Herrero-Martin, G. van der Laan, T. Hesjedal. "Cr_2Te_3 Thin Films for Integration in Magnetic Topological Insulator Heterostructures." *Sci. Rep.* **9**, 10793 (2019).

3. G. Awana, R. Fujita, A. Frisk, P. Chen, Q. Yao, A.J. Caruana, C.J. Kinane, N.J. Steinke, S. Langridge, P. Olalde-Velasco, S.S. Dhesi, G. van der Laan, X.F. Kou, S.L. Zhang, T. Hesjedal, D. Backes. "Critical analysis of proximity-induced magnetism in $MnTe/Bi_2Te_3$ heterostructures." *Phys. Rev. Mater.* **6**, 053402 (2022).

4. B. Achinuq, R. Fujita, W. Xia, Y. Guo, P. Bencok, G. van der Laan, T. Hesjedal. "Covalent mixing in the two-dimensional ferromagnet $CrSiTe_3$ evidenced by magnetic x-ray circular dichroism". *Phys. Status Solidi RRL* **16**, 4 (2021).

5. R. Fujita, J. Liu, X. Hu, Y. Guo, J. Herrero-Martín, G. van der Laan, T. Hesjedal. "X-ray spectroscopy for the magnetic study of the van der Waals ferromagnet $CrSiTe_3$ in the few- and monolayer limit". *2D Mater.* **9**, 4 (2022).

6. R. Fujita, P. Bassirian, Z. Li, Y. Guo, M.A. Mawass, F. Kronast, G. van der Laan, T. Hesjedal. "Layer-dependent magnetic domains in atomically thin Fe_5GeTe_2". *ACS Nano* **16**, 7 (2022).

7. M. Högen$^{\perp}$, R. Fujita$^{\perp}$, A.K.C. Tan$^{\perp}$, A. Geim, M. Pitts, Z. Li, Y. Guo, L. Stefan, T. Hesjedal, M. Atatüre. "Imaging Nucleation and Propagation of Pinned Domains in Few-Layer Fe_5GeTe_2". *ACS Nano* **17**, 17 (2023).

8. R. Fujita, G. Gurung, M.A. Mawass, A. Smekhova, F. Kronast, A.K.J. Toh, A. Soumyanarayanan, P. Ho, A. Singh, E. Heppell, D. Backes, F. Maccherozzi, K. Watanabe, T. Taniguchi, D.A. Mayoh, G. Balakrishnan, G. van der Laan,

T. Hesjedal. "Strain-Modulated Ferromagnetism at an Intrinsic van der Waals Heterojunction". *Adv. Funct. Mater.* (2024).

[⊥]Equal contribution denoted.

1 | Introduction to Two-Dimensional Materials and Ferromagnetism

1.1 Background

Research of layered van der Waals (vdW) compounds has intensified since pioneering characterizations of atomically thin graphene [1] and transition metal dichalcogenides (TMDs) [2, 3], which demonstrated changes in fundamental properties in the atomically thin limit, compared to that of their bulk counterparts. However, questions regarding the stability of two-dimensional (2D) magnetic order at any finite temperature have been postulated by the Mermin-Wagner theorem, which states that within the thermodynamic limit, long-range magnetic order of the Heisenberg type cannot exist in two dimensions or less [4]. Thus, initial studies were mostly limited to epitaxially grown ultrathin films of transition metals, for which three-dimensional (3D) island-type growth modes and substrate-induced film morphology limited the characterization of 2D magnetism [5].

The discovery and characterization of magnetism in 2D vdW materials has occurred only within the last five years [6–8]. In detail, a large uniaxial anisotropy opens a gap in the magnon dispersion, helping to stabilize 2D magnetism at finite temperatures. Indeed, the initial studies of magnetism in vdW materials focused on bulk compounds with strong magnetocrystalline anisotropy [6–8].

Magnetic vdW materials have several advantages compared to conventionally grown thin films. Firstly, the anisotropic crystal structure means that it is possible to exfoliate atomically thin flakes of vdW magnetic materials of extremely high structural quality. Additionally, interfacial diffusion is negligible due to the intrinsically weak vdW interaction, meaning that vdW heterostructures with atomically smooth interfaces can be created.

However, several technical aspects need to be considered. Specifically, exfoliated vdW materials are limited in lateral size, and typically span only some tens of

μm, limiting their scalability for wafer-scale applications [9, 10]. Another technical issue is the general lack of reproducibility from sample to sample. Interfacial strain and relaxation of the lattice at a vdW heterointerface are two outstanding problems which heavily influence the lattice structure, and electronic and magnetic properties [11].

In general, vdW interfaces are characterized by atomic abruptness and lack of interfacial diffusion. However, a central question is to what extent interfacial coupling between different vdW materials occurs at a vdW interface. For example, exchange splitting on the order of 10 T of the otherwise degenerate spin-polarized K and K' valleys have been observed at the interface of CrI_3 and WSe_2 [12]. In essence, interfacing two atomically thin crystals together will change properties such as lattice potential, Fermi surface, electron or hole effective mass, dipole field, and other fundamental quantities. In other words, despite a structurally weak interaction between adjacent vdW layers, it is possible to fundamentally alter the properties of vdW interfaces. This is most famously demonstrated by the observation of superconductivity [13], ferromagnetism [14], and ferroelectricity [15] in magic angle graphene and TMDs.

Many ferromagnetic vdW materials have large magnetic anisotropy, as demonstrated by their implementation in magnetic tunnel junctions (MTJs) [16], where (anti)-parallel magnetizations in adjacent magnetic layers form the '0' and '1' states in magnetic memory. For MTJs, it is necessary for the magnetization to be strongly anisotropic for the magnetoresistance ratio to well-defined. A way to tune the magnetic properties of vdW materials with such large anisotropy is desirable. A strain-modulated interface between Fe_3GeTe_2, an easy-axis vdW ferromagnet, and α-In_2Se_3, a vdW piezoelectric, is demonstrated in Chapter 4 of this thesis.

For 2D vdW magnets with large uniaxial anisotropy, the magnetic domains point (anti)-parallel to the anisotropy axis, while a smooth transition between the magnetic domains are found within the domain walls. In the atomically thin limit, the uniaxial anisotropy will usually force a single domain state [6, 8, 17]. The characterization of atomically thin materials with easy-plane anisotropy

is less straightforward. Strictly speaking, easy-plane anisotropy is insufficient to stabilize long-range 2D magnetic order. Instead, Berezenskii [18], Kosterlitz and Thouless [19] predicted vortex-antivortex pairs to form at finite temperatures. Such vortices have been observed in bulk Fe_5GeTe_2 [20], but not in the 2D limit, for which the strong magnetic anisotropy would likely confine non-collinear spin textures to within the domain walls. The experimental observation of vortex-antivortex pairs in a monolayer material would verify the Berezenskii-Kosterlitz-Thouless (BKT) theory, and would also demonstrate the intercompetition of the magnetic anisotropy [6, 8], demagnetization [21, 22] and dipolar interaction [23], rather than a dominant anisotropy. These vortex-antivortex pairs can be used as information bits in magnetic memory [24, 25], and could also form topological qubits based on Majorana bound states when coupled with a superconductor [26]. The characterization of easy-plane ferromagnetism, vortices and antivortices in atomically thin Fe_5GeTe_2 will be discussed extensively in Chapter 6.

1.2 Two-dimensional Heisenberg model

Fundamental aspects of magnetism, including domain energetics and dimensionality effects, will be discussed extensively in this thesis. In order to facilitate such a discussion, it is necessary to introduce several models describing magnetic behavior. The most fundamental of these is the isotropic Heisenberg model (Figure 1.1a), which considers the microscopic behavior of neighboring spins. In detail, for spins arranged in a lattice,

$$H = -\sum_{ij} J_{ij} \vec{S}_i \cdot \vec{S}_j \tag{1.1}$$

where the exchange interaction (J_{ij}) between spins on the i^{th} and j^{th} lattice sites are summed. For this particular case, the spins are isotropic, meaning that the dimensionality D of the order parameter is 3. Although Mermin and Wagner [4] postulate the lack of a phase transition at finite temperature for a 2D Heisenberg lattice, this prediction applies only for astronomical sample sizes; the finite size

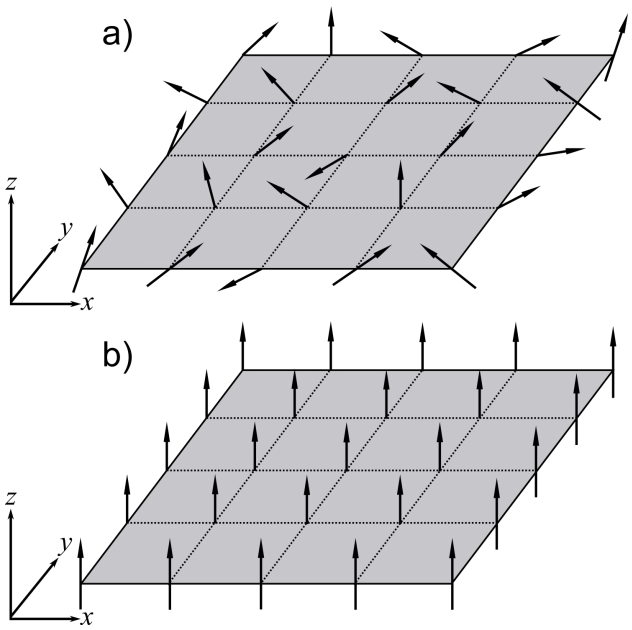


Figure 1.1: Schematic diagrams of 2D **a)** Heisenberg and **b)** Ising models. In the thermodynamic limit, a ferromagnetic phase transition at finite temperatures occurs only for **b)**, the 2D Ising model.

of real experimental systems precludes the application of the Mermin-Wagner theorem in most cases [27].

A special case of the isotropic Heisenberg model is the Ising model (Figure 1.1b), for which the spins are constrained to point only up or down by a magnetic anisotropy. In this case, $D = 1$, and the Hamiltonian can be written as:

$$H = -\sum_{ij} J_{ij} \vec{S}_i^z \cdot \vec{S}_j^z. \tag{1.2}$$

For a 2D lattice of Ising type, a phase transition to a magnetically ordered state is possible at finite temperatures regardless of sample size, as the magnetic anisotropy induces a gap in the magnon dispersion. The temperature at which ferromagnetic order is stabilized is known as the Curie temperature (T_C).

1.3 Mean field theory and critical exponents

Consideration of interactions on macroscopic length scales is also helpful for developing models describing ferromagnetism. Particularly, mean field theory, which assumes that all magnetic spins are subject to an identical exchange field from its neighbors, is implemented in Landau's theory of magnetism, where

$$M = \pm \left[\frac{a_0(T_C - T)}{2b} \right]^{\frac{1}{2}} \tag{1.3}$$

for $T < T_C$. The constants a_0 and b are positive.

Mean field theory adequately describes the magnetic behavior of systems for temperatures above or below T_C. However, the magnetism for temperatures close to T_C is characterized by fluctuations, rather than long-range order, and is best described by the characteristic length scale of such fluctuations, otherwise known as a correlation function. For temperatures below T_C, the correlation function will diverge to infinity.

More generally, mean-field theory can be refined by defining a set of critical exponents [28]. In detail,

$$\chi \propto (T - T_C)^{-\gamma} \qquad T > T_C \tag{1.4}$$

$$M \propto (T - T_C)^{\beta} \qquad T < T_C \tag{1.5}$$

$$M \propto (T - T_C)^{\frac{1}{\delta}} \qquad T = T_C \tag{1.6}$$

Here, χ is the magnetic susceptibility. The critical exponents of the Ising and Heisenberg models are tabulated in Table 1.1. Critical behavior of $CrSiTe_3$, a vdW ferromagnet described by the 2D Ising model, will be discussed in greater detail in Chapter 3.

Model	β	γ	δ
2D Ising	1/8	7/4	15
3D Ising	0.326	1.2378(6)	1.388(3)
3D Heisenberg	0.367	1.388	4.78

Table 1.1: Critical exponents β, γ and δ for Ising and Heisenberg models [28]. In the thermodynamic limit, there is no phase transition for the 2D Heisenberg model.

1.4 Mermin-Wagner theorem

In the thermodynamic limit, the stabilization of long-range 2D magnetic order is fundamentally constrained by the formalism postulated by Mermin and Wagner [4]. In detail, a uniaxial anisotropy is required to stabilize long-range magnetic order in a 2D lattice at finite temperatures. Without the uniaxial anisotropy, gapless magnon modes, which are quantized fluctuations of the magnetic moment, will prevent the formation of long-range magnetic order [4]. However, the Mermin-Wagner theorem applies only for astronomical sample sizes; real experimental 2D materials can still undergo a phase transition at finite temperature even without a magnetic anisotropy [27], as demonstrated by the stabilization of ferromagnetism in atomically thin bilayer $CrGeTe_3$ with soft ferromagnetism and Heisenberg-type behavior [7].

1.5 XY model and Berezenskii-Kosterlitz-Thouless theory

The 2D Heisenberg and Ising models describe the interaction among spins with $D = 3$ and $D = 1$, respectively. In magnetic systems, such dimensionality is determined by the magnetic anisotropy. As stated above, there is no phase transition at finite temperatures for the Heisenberg model, for which $D = 3$. It is worth examining the behavior of a 2D lattice for which $D = 2$. In other words, the spins are constrained to lie within the xy plane in the so-called XY model (Figure 1.2) [18]. Ferromagnetic materials for which $D = 2$ are said to have

easy-plane anisotropy. The Hamiltonian for the XY model can be expressed as

$$H = -\sum_{ij} J_{ij}\vec{S}_i \cdot \vec{S}_j = -\sum_{ij} J_{ij} cos(\phi_i - \phi_j) \tag{1.7}$$

where ϕ_i and ϕ_j are the azimuthal angles of the i^{th} and j^{th} spins, respectively. Counter-intuitively, the XY model is not sufficient to induce a transition to 2D long range order [18]. Instead, a quasi-ordered state for which the correlation length decays algebraically is found at low temperatures. The correlation length at high temperatures decays exponentially, resulting in a disordered state. In between the low temperature and high temperature regimes, bound pairs of vortices and antivortices have been predicted to be thermally stable. In detail, the Helmholtz free energy of the system is the difference between the energy of the vortices and the entropy,

$$F = (\pi J - 2k_B T) ln(R/a). \tag{1.8}$$

Here, R is the size of the system and a is the lattice parameter. F is negative for temperatures below the Kosterlitz-Thouless transition, $T_{\text{KT}} < 2k_B T/J$, at which a divergence of the magnetic susceptibility has been predicted [19]. At temperatures below T_{KT}, vortices and antivortices are bound to one-another, while at temperatures above T_{KT}, vortices and antivortices will dissociate into isolated constituents [28].

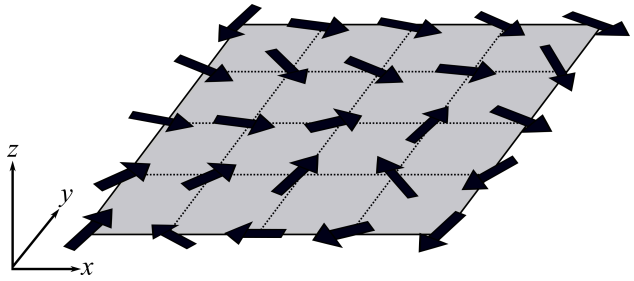


Figure 1.2: 2D XY model, for which the magnetic spins are constrained to lie within the xy plane.

1.6 Ferromagnetic domains and domain wall energy

The magnetization in materials will often break up into smaller domains, each with their own magnetic orientation. For magnetic materials with uniaxial magnetic anisotropy energy K_u and exchange stiffness A, one may question why such domains, which incur an additional domain wall energy $\sigma_w \propto \sqrt{AK_u}$ [21], form at all. Here, A is a material-dependent constant quantifying the strength of the exchange interaction and T_C within the material rather than among microscopic spins [21]. In such materials, it is energetically favorable for the magnetization to separate into smaller domains, as this minimizes the demagnetization energy within a volume V [21],

$$K_d = \frac{1}{2}\mu_0 \int_V (\vec{H}_d \cdot \vec{M}) dV \tag{1.9}$$

which originates from the interaction between the magnetization $\vec{M}$, and the stray field produced by this magnetization, $\vec{H}_d$. For magnetic materials, K_d is minimized at the expense of σ_w.

1.7 Ferromagnetic hysteresis

The magnetic domain structure within a material is dependent on the external magnetic field. In zero applied field, the magnetization will generally break up into domains and the material will remain in a demagnetized state. Upon application of an external field $H_{applied}$, the magnetization exhibits a hysteretic response (Figure 1.3) [29]. In detail, the magnetization will initially follow the field, transitioning from a demagnetized state to a saturated state at $H = B_s$. After saturation, the magnetization only switches polarity at a coercive field, H_c. For a certain saturation field $H_{sat} > H_c$, the magnetization will fully point in the direction of $H_{applied}$. For zero magnetic field, there will be a remnant magnetization B_r. H_c characterizes the field required to switch a ferromagnet, and gives insight into fundamental parameters and characteristics, including the magnetic

anisotropy (Chapter 4) and domain wall pinning (Chapter 5).

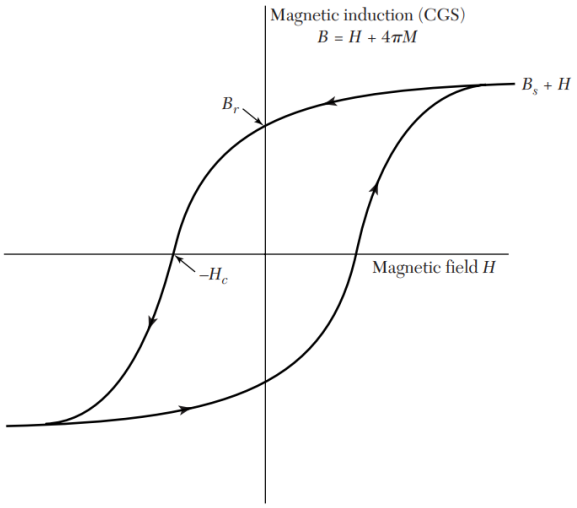


Figure 1.3: Ferromagnetic hysteresis with coercive field H_c, saturation magnetization B_s and remnant magnetization B_r. Figure adapted from Ref. [29].

1.8 Bloch and Néel-type type domain walls

Magnetic domains are separated by domain walls. Within a domain wall, the magnetization smoothly varies, facilitating a continuous variation of the magnetization between adjacent domains. Furthermore, domain walls can be categorized as Bloch-type or Néel-type domain walls. For Bloch-type domain walls, the magnetization at the center of the wall points perpendicular to the direction of the wall, while for Néel-type domain walls, the magnetization at the center of the wall points parallel. The magnetism in a material will be separated by Bloch or Néel domain walls depending on the total energy. In detail, for Bloch walls, the magnetic dipoles remain separated along the wall, meaning that the dipolar energy is satisfied at the expense of K_d. In other words, Bloch-type domain walls are favorable for thicker films for which the stray field from a domain wall are negligible. However, K_d becomes relevant for thin films, for which Néel domain walls are preferable [29].

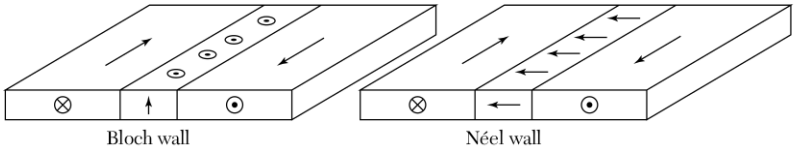


Figure 1.4: Bloch and Néel-type domain walls in an easy-plane ferromagnet. Figure adapted from Ref. [29].

1.9 Thesis outline

The aims of this thesis are to characterize intrinsic properties of 2D ferromagnetism in atomically thin vdW materials, as well as to develop methods of tuning such intrinsic magnetic properties in the 2D limit. Additionally, this thesis also utilizes the analysis of magnetic domain structures to make inferences regarding fundamental parameters including K_u, K_d and T_C.

In Chapter 3, changes in fundamental properties in $CrSiTe_3$, a 2D Ising-type vdW ferromagnet, are characterized as a function of layer thickness. In detail, an enhancement of the ratio of the spin magnetic moment (m_l) to the orbital magnetic moment (m_s), is found in atomically thin $CrSiTe_3$, demonstrating a non-negligible interlayer exchange interaction for this 2D Ising-type ferromagnet.

In Chapter 4, the strain-tuning of magnetism is demonstrated at an interface between a uniaxial vdW ferromagnet, Fe_3GeTe_2, and a vdW piezoelectric, α-In_2Se_3. Specifically, a reduction of T_C and σ_w are observed for Fe_3GeTe_2 which is interfaced with α-In_2Se_3. Strain-tuning by implementation of α-In_2Se_3 is also demonstrated for graphite.

In Chapter 5, thickness-dependent domain structures in Fe_5GeTe_2, a vdW ferromagnet which can have weak K_u, suggest intercompetition of energy terms in the atomically thin limit rather than ferromagnetism stabilized by K_u. Domain wall pinning is found to be the dominant mechanism in the magnetic hysteresis, resulting in an enhanced H_c in the atomically thin limit [30].

In Chapter 6, easy-plane ferromagnetism, and vortices and antivortices are characterized in atomically thin Fe_5GeTe_2. In detail, vortices and antivortices are found within close proximity to one-another in 4 L Fe_5GeTe_2. These spin textures could potentially be topologically non-trivial. Future work includes the characterization of topological properties and implementation in hybrid ferromagnet-superconductor heterostructures.

2 | Methods

2.1 Surface-sensitive microscopies

Mechanically exfoliated 2D materials usually have small lateral sizes and atomic thickness, making characterizations of atomically thin magnetism somewhat challenging. It is important to select characterization techniques with high surface sensitivity, which are capable of resolving small flakes. These constraints preclude macroscopic characterization techniques, such as bulk vibrating sample magnetometry based on the superconducting quantum interference device (SQUID), which does not have the capability to spatially resolve the magnetic signal. This is contrast to scanning SQUID microscopy, which consists of scanning a SQUID with a small pickup area over the sample surface [31]. X-ray and neutron-based scattering techniques, which depend on 3D structure factors [32], would also struggle to detect magnetic order in the atomically thin limit.

This thesis utilizes surface-sensitive microscopies to characterize magnetic order in 2D vdW magnetic materials. In detail, X-ray photoelectron emission microscopy (XPEEM), which is used to obtain spatial images of the X-ray magnetic circular dichroism (XMCD) [33], and nitrogen-vacancy center scanning magnetometry (NVSM) [34], which employs a single-spin magnetometer to detect stray fields, are employed to image the magnetic domains in 2D magnets. Other methods, including magneto-optical Kerr effect (MOKE) microscopy [6, 8] and transport measurements have also been used to characterize the ferromagnetism in 2D vdW magnets [17, 35]. However, the advantages of real-space imaging include direct visualization and characterization of magnetic phenomena with weak or indirect signatures, such as domain pinning (Chapter 5) or non-collinear spin textures (Chapter 6).

2.2 Mechanical exfoliation

The commonly used mechanical exfoliation techniques are well-documented in the literature [36–38]. In short, bulk vdW materials are mechanically separated

into thin layers with adhesive tape. The tape holding the exfoliated material can be placed over a substrate and slowly peeled, leaving behind atomically thin sheets on the substrate. Alternatively, the tape can also be placed and peeled over a polymer stamp, allowing for the deterministic placement of 2D materials onto a target substrate [36, 37].

Conversely, exfoliation over Au films significantly improves the size and yield of atomically thin layers [39], but does not allow for the deterministic placement of thin flakes.

Several technical issues exist for mechanically exfoliated 2D materials. Contamination from polydimethylsiloxane (PDMS) residues [38] and the presence of interfacial contaminants, which coalesce into blisters, can degrade properties, such as the carrier mobility, in 2D materials. An alternative is to use a polypropylene carbonate liftoff technique [36], for which the atomically thin layers do not come into contact with the polymer. However, this technique only works for vdW materials with low cleavage energy, as the material must first be exfoliated over SiO_2 or some other inert substrate. Direct exfoliation of few-layer $Fe_{3,5}GeTe_2$ is not feasible over bare Si/SiO_2 substrates, as the cleavage energy is too large.

Methods of limiting the degree of contamination from the polymer residue include transferring layers as slowly as possible at temperatures of 150° C or higher [38]. By employing this technique, the contaminants migrate towards the sides of the flake, and interfacial contamination can be greatly reduced.

The air sensitivity of magnetic 2D materials [40] necessitates their exfoliation within an inert environment. The samples discussed throughout this thesis were prepared in a glovebox filled with Ar, with oxygen and moisture levels less than 10 parts per million (ppm). Furthermore, the flakes must be encapsulated between thin layers of hexagonal boron nitride (hBN). The flakes must be completely encapsulated, leaving no parts exposed. Furthermore, only capping the flakes with top hBN will not prevent degradation [40], necessitating complete encapsulation from both above and below.

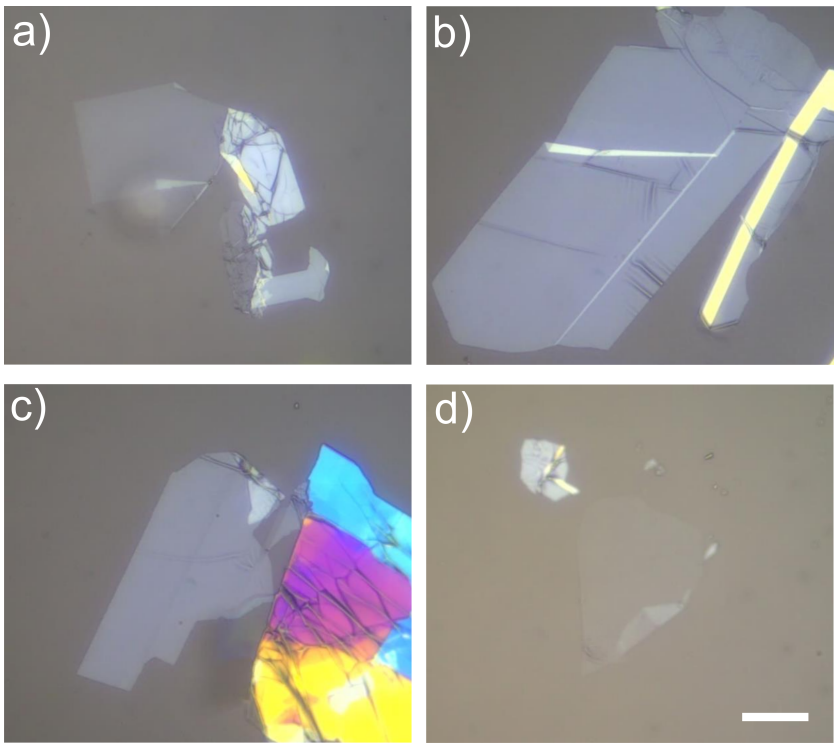


Figure 2.1: Optical microscopy of thin hBN flakes **a-d)**, which are semi-transparent in the atomically thin limit. Bulk hBN flakes, each with a characteristic reflectance resulting from constructive interference of light reflected from the top and bottom interfaces, are visible in **c)**. Scale bar=50 µm. Bulk single crysals were provided by Dr. Takashi Taniguchi and Dr. Kenji Watanabe at the National Institute of Materials Science.

2.3 Optical characterization

Although the thickness of 2D materials can be determined by atomic force microscopy (AFM) (Section 2.4) or transmission electron microscopy (TEM), it can be difficult and time-consuming to locate a small flake on a substrate. For TEM, additional steps are required, further adding to this lengthy process.

Thicknesses of 2D materials are readily estimated by their reflectance under a reflected light microscope. For bulk vdW semiconductors and metals with a skin depth of some tens of nm, all of the incident light will be completely reflected. For wide-gap bulk vdW semiconductors which are optically transparent such

as hBN, reflection from the top and bottom interfaces will result in constructive interference for path length differences which are integer multiples of the wavelength λ. Therefore, for bulk hBN flakes of varying thickness, the reflected optical contrast will simply differ in color when exposed to white incident light (Figure 2.1c).

In the atomically thin limit, vdW materials will generally become semi-transparent, regardless of their optical properties in the bulk limit. For such bulk vdW materials, light is reflected from the top and bottom interfaces. However, there is no constructive interference from atomically thin 2D materials, as the thickness $d \ll \lambda$. When light is incident upon an interface, a change in electrical permittivity and the refractive index leads to the refraction of the light as it propagates across the interface. In the case of the substrate-2D material interface for which the thickness of the 2D material is atomically thin, an effective permittivity can be empirically determined [41]. In practice, the refraction and reflectivity can also be optimized by proper substrate selection.

It is common to place 2D materials over Si substrates with an oxide thickness of 300 nm. The correlation between the number of layers and the reflectance can be determined for a given wavelength of incident light. Such a correlation is also dependent on the material. For example, hBN will progressively become more transparent as the thickness is reduced (Figure 2.1). Monolayer hBN has an extremely weak optical contrast even when placed over oxidized Si substrates, making the identification of monolayer hBN an extremely challenging task [42].

2.4 Atomic force microscopy

AFM utilizes the mechanical interaction between a nanoscale tip mounted on a cantilever and the sample to characterize the surface topography, which is useful for the determination of layer thicknesses of 2D materials. Moreover, different types of tip-sample interactions, including magnetic and electrostatic interactions, are implemented in magnetic force microscopy (MFM) and piezoresponse force microscopy (PFM) (Chapter 4) in the characterization of ferroic materials. For all cases, the spatial resolution is limited by the diameter of tip, and varies

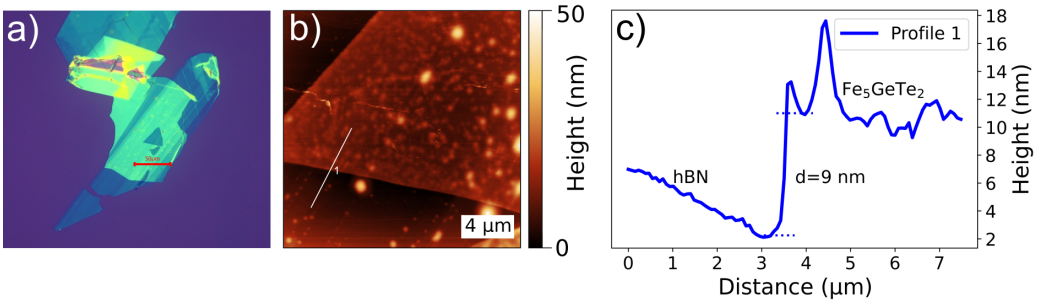


Figure 2.2: AFM data showing surface topography and thickness of a flake of Fe_5GeTe_2 encapsulated between hBN. **a)** Optical micrograph of the sample. Scale bar = 50 µm. **b)** Surface topography of the encapsulated flake. The location is indicated by the scale bar in **a)**. **c)** The thickness of the Fe_5GeTe_2 flake is determined to be approximately 9 nm, or 11 monolayers [46], as shown by the line profile. Bulk Fe_5GeTe_2 crystals were provided by Dr. Andrew May at Oak Ridge National Laboratory, and the bulk hBN crystals were provided by Dr. Kenji Watanabe and Dr. Takashi Taniguchi at the National Institute of Materials Science.

from 10 to 100 nm. AFM measurements can be performed in ambient conditions, allowing for the characterization of 2D materials without the stringent requirements posed by ultrahigh vacuum techniques (UHV). However, the lateral resolution is limited compared to UHV techniques including scanning tunneling microscopy, which can spatially resolve individual atoms, defects, and moíre potentials [43]. Moreover, the detection of stray fields emanating from atomically thin materials with MFM is also challenging. Several reviews [44, 45] can be referenced for a detailed explanation of the basic working principles of AFM.

An exemplary AFM measurement of exfoliated Fe_5GeTe_2 encapsulated between thin hBN is shown in Figure 2.2. The atomically smooth surface topography of hBN is in marked contrast to that of the encapsulated Fe_5GeTe_2, also a nominally atomically smooth 2D material. Reasons for the enhanced surface roughness within the encapsulated Fe_5GeTe_2 could be some trapped interfacial contaminants [38] or lattice relaxation resulting in local strains. Strained vdW heterojunctions will be discussed extensively in Chapter 4.

2.5 Raman microscopy

Raman microscopy, which probes vibrational modes of atoms characteristic of certain phenomena or properties such as strain [47, 48], magnetic state as a function of temperature [49], oxidation state [40], surface degradation [40] and carrier doping [50], is an indispensable method for characterizing 2D materials, as it is non-destructive and is also relatively quick. Several extensive reviews [51] discuss the application of Raman microscopy to graphene and other 2D vdW materials. Exemplary Raman data obtained from a heterostructure of α-In_2Se_3 and graphite are shown in Figure 2.3. In detail, spatial maps of the graphene D mode reveal a finite defect density in the graphene lattice. The Tuinstra-Koenig relation, given by the intensity ratio of the D and G modes, $I(D)/I(G)$, show that incorporating α-In_2Se_3 reduces the defect density in graphene. Raman spectroscopy can be used to determine other fundamental quantities including the number of layers in graphite [51].

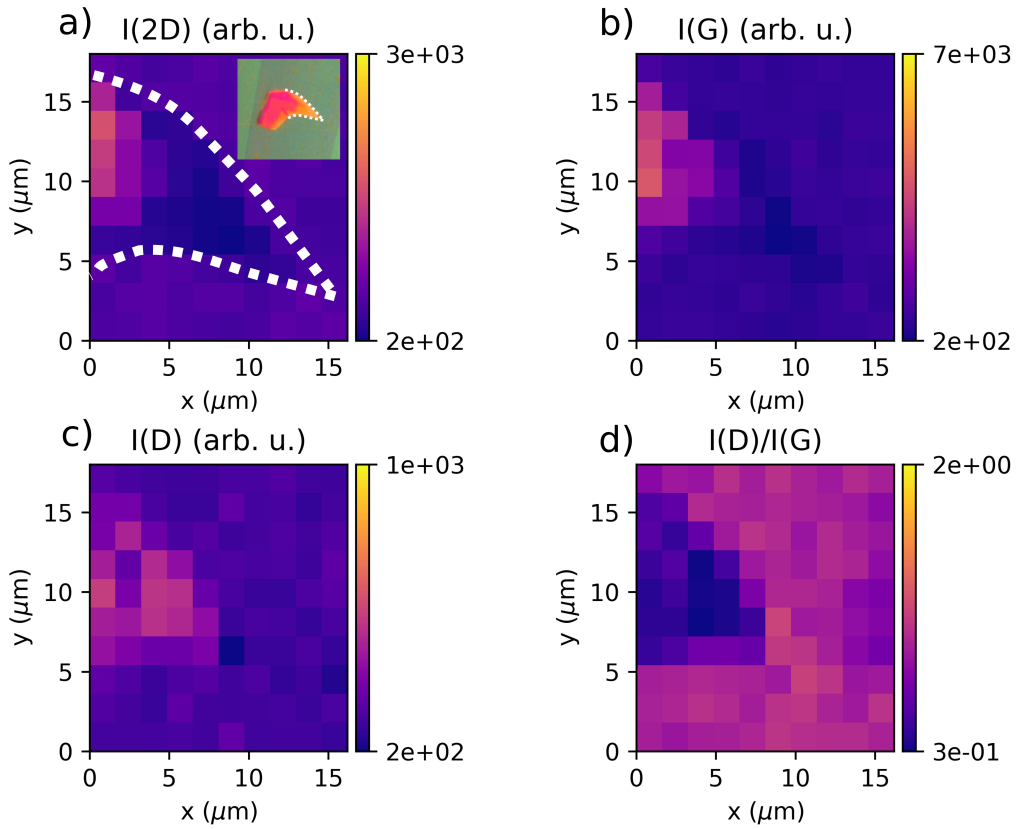


Figure 2.3: Spatial mapping of the **a)** $2D$, **b)** G and **c)** D Raman modes and **d)** the Tuinstra-Koenig relation, $I(D)/I(G)$, in a graphite/α-In_2Se_3 heterostructure. The Tuinstra-Koenig relation is sensitive to the defect concentration in graphite. Bulk α-In_2Se_3 crystals were provided by Dr. Daniel Mayoh and Prof. Geetha Balakrishnan at the University of Warwick. The graphite was purchased from HQ Graphene.

2.6 X-ray magnetic circular dichroism

XMCD is a spectroscopy technique used for the characterization of magnetic materials. In short, the empty states above the Fermi level are split into spin-up and spin-down states in a magnetic material. X-rays with right circular polarization (RCP) and left circular polarization (LCP) will resonantly excite spin-polarized electrons from core level states to above the Fermi level, where there exists an imbalance in spin population because of the magnetization of the material. In other words, XMCD probes the population imbalance of spins above the Fermi level by utilizing the $2p$-$3d$ transition.

Photons with RCP (LCP) will preferentially excite $2p$ core levels with spin-up (spin-down) polarization. The $2p$ core levels are split by the spin orbit coupling into $2p_{3/2}$ and $2p_{1/2}$ states, resulting in two distinct resonances in the X-ray absorption spectroscopy (XAS) spectra, which are the L_3 and L_2 absorption edges. From the $2p_{3/2}$ core level, photons with RCP will excite 62.5% of spin-up electrons, while photons with LCP will excite 37.5% of spin-up electrons. However, for the $2p_{1/2}$ core level, photons with RCP will excite just 25% of spin-up electrons, while photons with LCP will excite 75% of spin-up electrons.

Next, the electrons must find an empty $3d$ state. If the $3d$ states are spin-polarized, then an imbalance in the differential absorption of photons with opposing circular polarizations, which is the XMCD, will occur. Because the transition probabilities for spin-up electrons vary in an inverse sense between the $2p_{3/2}$ and $2p_{1/2}$ core levels, the XMCD at the L_3 and L_2 edges will be opposite in sign.

2.6.1 Sum rule analysis

XMCD finds application in the estimation of the magnetic spin moment m_s and magnetic orbital moment m_l in transition metal atoms. In detail, relations between m_s and m_l and the integrated areas of the XAS and XMCD spectra [53, 54] are listed in Equations 2.1-2.3.

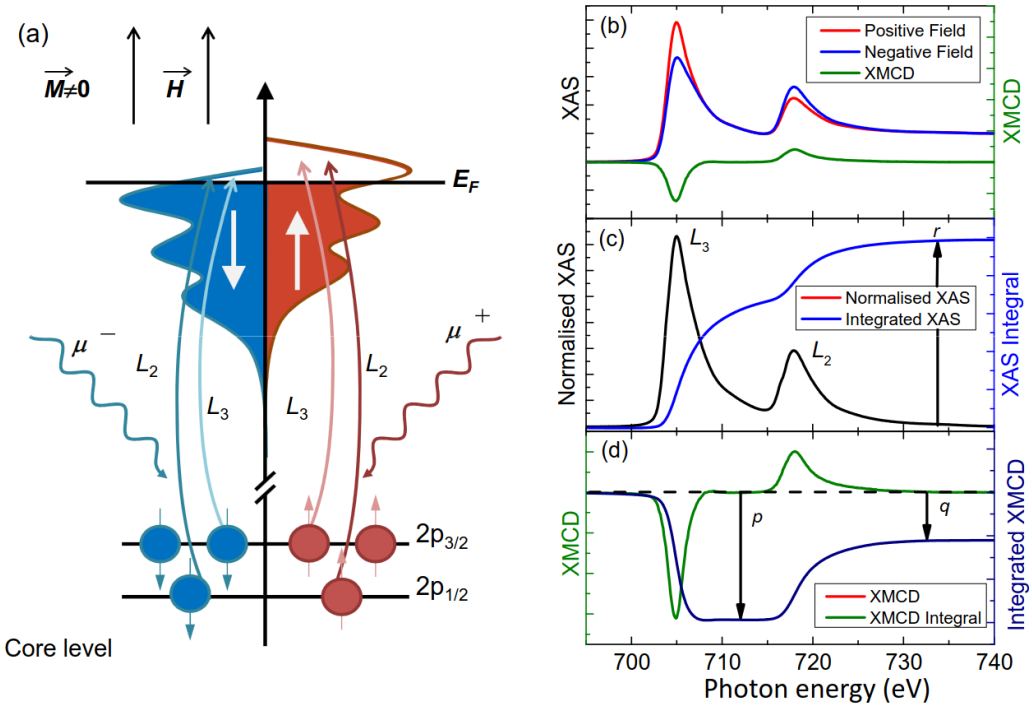


Figure 2.4: a) XMCD is a spectroscopy which employs the $2p$ to $3d$ transition as a probe of the spin imbalance of empty $3d$ states above the Fermi level. In detail, spin-orbit coupling splits the $2p$ states into $2p_{3/2}$ and $2p_{1/2}$ core levels. For photons with RCP, 62.5% of spin-up electrons are excited from the $2p_{3/2}$ core level, while only 25% of spin-up electrons are excited from the $2p_{1/2}$ core level. **b)** XAS spectra obtained at RCP and LCP, and the XMCD, which is obtained from the difference, is shown. The net effect of the differing transition probabilities from the core levels is that the XMCD signals at the L_3 and L_2 edges, which respectively originate from the $2p_{3/2}$ to $3d$ and $2p_{1/2}$ to $3d$ transitions, will be of opposite sign, as seen in the XMCD spectra. **c)** The sum of the XAS spectra obtained at RCP and LCP is shown. The integral r, which is implemented in the sum rules, is explicitly denoted. **d)** The XMCD is shown once more, with the integrals p and q explicitly denoted. Figure adapted from Ref. [52].

$$p = \int_{L_3} (\mu^- - \mu^+)\, dE \tag{2.1}$$

$$q = \int_{L_3} (\mu^- - \mu^+)\, dE + \int_{L_2} (\mu^- - \mu^+)\, dE \tag{2.2}$$

$$r = \int_{L_3+L_2} (\mu^- + \mu^+)\, dE \tag{2.3}$$

The values p and q are related to the integrated areas of the XMCD ($\mu^- - \mu^+$) over the L_3 and $L_3 + L_2$ edges, respectively, and r, which is the integrated area of the sum of the XAS spectra ($\mu^- + \mu^+$) over the $L_3 + L_2$ edges (Figure 2.4d), are used to determine m_l and m_s:

$$\frac{m_l}{n_h} = -\frac{4}{3}\frac{q}{r} \tag{2.4}$$

$$\frac{m_s}{n_h} = -\frac{6p - 4q}{r} \tag{2.5}$$

Here, n_h, the number of $3d$ holes, is usually estimated by first-principle band structure calculations [55]. Generally, a background subtraction in the form of a step function is implemented for the sum of the XAS spectra prior to the calculation of r [55]. The ratio,

$$\frac{m_l}{m_s} = \frac{1}{(9/2)(p/q) - 3} \tag{2.6}$$

which is independent of the number of holes n_h, is a particularly useful indicator of electronic and magnetic properties. This ratio will be implemented to characterize changes in the ferromagnetic and electronic ordering in atomically thin $CrSiTe_3$ (Chapter 3).

2.7 X-ray photoelectron emission microscopy

XPEEM is a technique based on XMCD (Section 2.6) used to characterize the magnetic and chemical states of materials on microscopic length scales. In other words, it can be considered as a type of XMCD-based microscopy. For magnetic materials, XPEEM can be used to obtain images of magnetic domains. In detail, the XMCD signal is proportional to $\vec{m} \cdot \vec{k}$, where $\vec{m}$ is the magnetization vector and $\vec{k}$ is the propagation vector of the incoming X-ray beam [33].

In practice, the angle of incidence of $\vec{k}$ with respect to the sample surface is 16°, which means that 28% of the sample's OOP magnetization component is projected along $\vec{k}$ [56]. The XMCD asymmetry is defined as $(\sigma_- - \sigma_+)/(\sigma_- + \sigma_+)$, where σ_- and σ_+ are spatially resolved images of the XAS spectra taken with LCP and RCP X-rays, respectively.

XPEEM has several distinct advantages regarding 2D materials, including being able to determine the oxidation state of transition-metal based compounds, such as Fe_3GeTe_2 or Fe_5GeTe_2, which is not possible with other techniques as they are not simultaneously sensitive to both the chemical composition and magnetic state.

In XPEEM, it is also possible to characterize complex magnetic phases by the construction of vector maps of the magnetization. In practice, this is done by obtaining XMCD images taken at different azimuths, and determining the azimuthal dependence of the XMCD signal as a function of real space.

In detail, for samples with an easy-plane anisotropy, the orientation of in-plane (IP) magnetic domains is readily resolved by the vector addition of the XMCD images taken at 0° and 90° azimuths [33]. For samples with easy-axis anisotropy, IP and OOP components of the magnetization can be resolved by subtracting the XMCD images taken at 0° and 90° azimuths [22]. In practice, an algorithm is applied to correct for distortions of the images obtained at 0° and 90° azimuths. Vector mapping will be used extensively to characterize the magnetism in few-

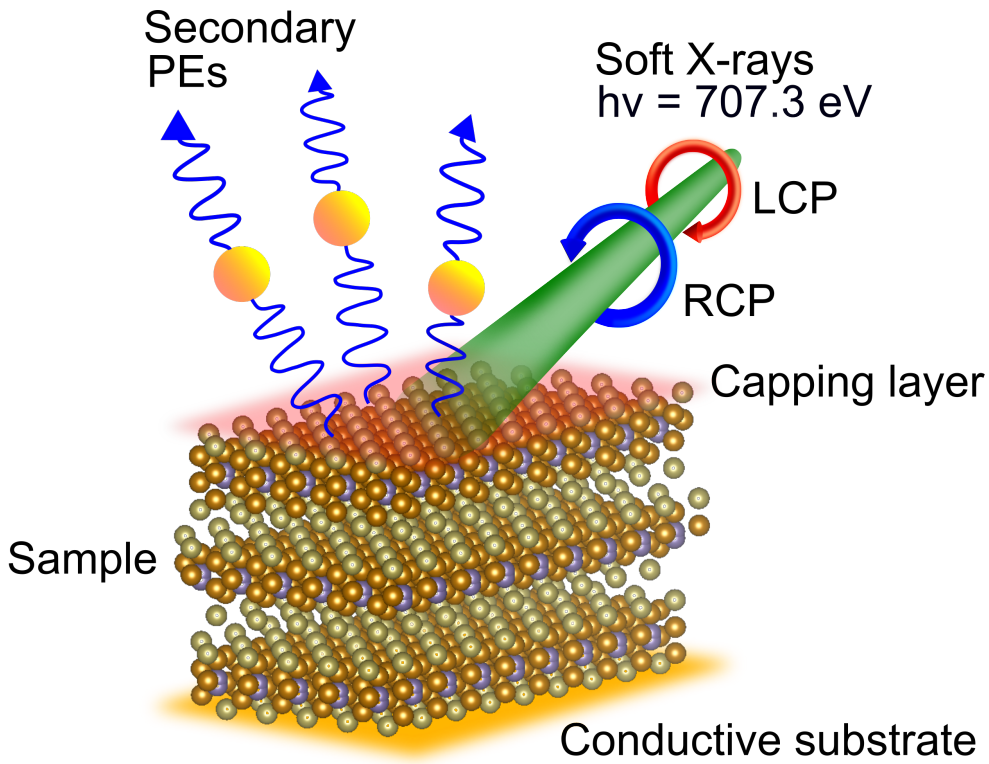


Figure 2.5: Microscopic images with fields of view ranging from ≈ 3 to 50 µm are obtained with RCP and LCP photons. The XMCD signal is obtained by subtracting the images obtained with RCP from those obtained with LCP. For XPEEM, it is preferable to place the sample on a conductive substrate which is used to ground the sample to the sample holder. For 2D materials, a capping layer is also necessary to prevent oxidation, but must be thin enough to allow secondary photoelectrons to reach the detector.

layer Fe_5GeTe_2 in Chapter 6.

2.8 Nitrogen-vacancy center scanning magnetometry

NVSM utilizes a nitrogen substitution adjacent to a lattice vacancy in diamond, which acts as a single-spin defect, to sense the magnetic stray fields emanating from the surface of a sample. In detail, the energy levels within the defect, $m_S =$

+1 and $m_S = -1$, undergo a Zeeman splitting which is linearly proportional to the external field present along the NV axis. This splitting can be optically read out, or addressed, with a laser. Thus, stray fields can be determined by the splitting of energy levels of the $m_S = +1$ and $m_S = -1$ states, otherwise known as the optically detected magnetic resonance (ODMR). The sensitivity of NVSM ranges from pT-μT $Hz^{-1/2}$, and sub-nm spatial resolutions have also been achieved [57]. For comparison, SQUIDs have sensitivities on the order of fT $Hz^{-1/2}$ and a spatial resolution of approximately 100 nm.

One limitation of NVSM is the inability to apply large fields *in-situ*, or to detect stray fields larger than 100 G, which quenches the spin readout [34]. In practice, a small bias field is applied to distinguish the polarity of the stray field, allowing for the spatial mapping of the stray field and estimation of the spatial magnetization via an inverse Fourier transform. Despite the aforementioned condition, NVSM is an extremely successful technique for characterizing static domain arrangements and field-induced domain motion [11, 30], domain walls [58], and static currents [59]. A detailed and comprehensive review regarding the working principles of NVSM and its application to condensed matter systems can be found in Refs. [34, 60].

The NVSM measurements and analysis in Chapter 5 were performed by Dr. Michael Högen, Dr. Anthony K.C. Tan, and Prof. Mete Atatüre at the Cambridge Nanoscale Sensing and Imaging Suite (CANSIS) at the University of Cambridge. In detail, the setup consists of a confocal optical microscope and AFM housed in a closed-cycle cryostat (attoDRY1000, Attocube Systems).

3 | X-ray spectroscopy of atomically thin $CrSiTe_3$

3.1 $CrSiTe_3$: A quasi-two-dimensional ferromagnetic semiconductor

$CrSiTe_3$ is a vdW ferromagnetic semiconductor belonging to the $R\bar{3}$ space group with a bulk T_C of 31 K with a weak OOP magnetic anisotropy [61]. Compared to $CrSiTe_3$, $CrGeTe_3$, a closely related vdW ferromagnetic semiconductor, has a smaller vdW gap, resulting in an enhanced bulk T_C of 61 K and critical exponents which suggest that the magnetism is described by the tricritical mean-field model, where the phase transition lies on a 2D to 3D tricritical point [62]. In a seminal characterization of the magnetic properties of atomically thin $CrGeTe_3$ [7], a small bias field was applied to open a gap in the magnon dispersion, stabilizing magnetism down to the bilayer.

Although somewhat varying reports of the magnetic critical behavior of $CrSiTe_3$ exist in the literature [63, 64], the magnetic interactions are mostly limited to within the *ab* plane below T_C, in contrast to the magnetic interactions described by the tricritical mean field model in $CrGeTe_3$. In detail, the critical exponents $\beta = 0.170 \pm 0.008$, $\gamma = 1.532 \pm 0.001$, and $\delta = 9.917 \pm 0.008$ [63] are consistent with the 2D Ising model coupled with exponentially decaying long-range interactions. Apart from a reduction of T_C, the weakly coupled vdW layers and insulating character of $CrSiTe_3$ below T_C suggest that the magnetic properties should not strongly depend on the number of layers. Indeed, conventional characterization techniques, which suffer from limited magnetic sensitivity and spatial resolution, would be unable to distinguish changes in the few-layer magnetism. Here, high-field XMCD shows that despite the weak interlayer coupling, the magnetic moments m_l and m_s strongly depend on the thickness, demonstrating that magnetism in the few-layer limit is not as trivial as a simple reduction in T_C even for weakly coupled vdW materials. In detail, the ratio m_l/m_s increases in magnitude for $CrSiTe_3$ below 10 L, potentially indicating an enhanced Cr-Te

hybridization in the atomically thin limit [65].

3.2 Methods

3.2.1 Crystal growth and exfoliation of bulk $CrSiTe_3$

Single crystals of $CrSiTe_3$ were grown with chemical vapor transport (CVT) by Xiaofei Hou and Prof. Yanfeng Guo at ShanghaiTech University. More details regarding the growth methods can be found in Ref. [61]. To produce atomically thin $CrSiTe_3$ flakes, the adhesive interaction between a thin Au film and vdW chalcogenides was utilized to exfoliate atomically thin $CrSiTe_3$ flakes across relatively large length scales of several hunded µm. In detail, bulk $CrSiTe_3$ crystals were cleaved with adhesive tape inside of a glovebox. The tape loaded with the cleaved crystals was then placed over oxidized Si wafers covered with a Au (10 nm) film deposited over a Cr (3 nm) adhesion layer. The wafer was then heated at 100° C. After allowing the sample to cool to room temperature, the tape was slowly removed, leaving behind large flakes of atomically thin $CrSiTe_3$. More details can be found in Ref. [39].

3.2.2 High-field X-ray magnetic circular dichroism

XAS and XMCD measurements were performed at the HECTOR endstation (BOREAS) at BL29 at the ALBA Synchrotron. The beam size was reduced to 13×58 µm^2. A spatial map of the sample was obtained by raster-scanning the beam over an area with large $CrSiTe_3$ flakes. XAS spectra at the Cr $L_{2,3}$ edges (570-590 eV) were recorded with RCP and LCP at normal incidence in a magnetic field of ±6 T applied along the beam. The XAS signal I_{sum} is defined as $I^- + I^+$ with $I^- = \frac{1}{2}[\, I_{\text{LCP}}(H) + I_{\text{RCP}}(-H)\,]$ and $I^+ = \frac{1}{2}[\, I_{\text{LCP}}(-H) + I_{\text{RCP}}(H)\,]$. The XMCD signal is defined as $I^- - I^+$ [66]. The measurements were performed in total electron yield (TEY) mode at a temperature of 10 K. The photon energy was calibrated using a Cr_2O_3 reference sample.

The spin and orbital moment, m_l and m_s, were estimated with sum rule analysis (Chapter 2.6.1) [67]. In detail, p and q were obtained by integrating the XMCD

spectra over the L_3 and $L_{2,3}$ edges. The normalization factor r was obtained by integrating I_{sum} over the $L_{2,3}$ edges. Taking into account the number of d holes, $n_h = 10 - n_d$, the spin and orbital moments per Cr atom are $m_s = -\langle 2S_{eff,z}\rangle = -(6p - 4q)Cn_h/r$, where $C = 2$ is a correction factor for Cr [68] and $-\langle L_z\rangle = -\frac{4}{3}qn_h/r$. The effective spin moment $\langle 2S_{eff,z}\rangle = \langle 2S_z\rangle + \langle 7T_z\rangle$, where $\langle 2S_z\rangle$ is the isotropic spin moment and $\langle T_z\rangle$ is the z component of the magnetic dipole term $T = \sum_i \vec{s_i} - 3\hat{r_i}(\hat{r_i} \cdot \hat{s_i})$, where $\vec{s_i}$ and $\hat{r}$ are the spin and positition of the i^{th} electron in the atom [53]. The tensor T gives the anisotropy of the spin moment due to coupling with the charge quadrupole moment, and can be finite for non-cubic environments.

3.3 Spatial mapping of large-scale exfoliated $CrSiTe_3$

Bulk $CrSiTe_3$ was exfoliated using a Au-assisted exfoliation method [39] inside of a glovebox. The optical micrograph shows few-layer flakes (Figure 3.1a). AFM, which was performed after the experiment, demonstrates that the flakes range in thickness from 1-10 layers. The thickness of one monolayer of $CrSiTe_3$ is 0.7 nm [69]. After the exfoliation of large-area few-layer flakes was confirmed by optical microscopy, the sample was transferred *in-situ* to the high-field end-station.

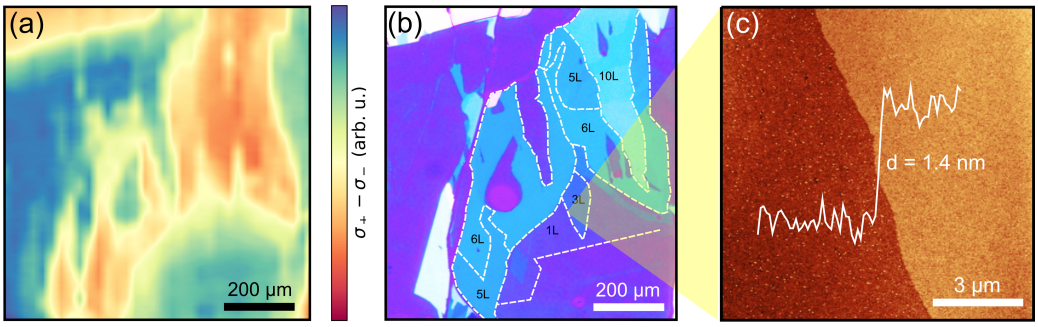


Figure 3.1: a) Spatial map of the magnetic asymmetry obtained at the Cr L_3 edge at 10 K in zero applied field. These data were obtained by Ryuji Fujita and Dr. Javier Herrero-Martin at BOREAS (BL29) at ALBA Synchrotron. **b)** Optical micrograph of exfoliated few-layer $CrSiTe_3$ flakes. **c)** An *ex-situ* AFM measurement demonstrating a bilayer (1.4 nm) step height. Thicknesses for each optical contrast were determined with AFM accordingly. Different layers are demarcated by the white dashed lines in **b)**.

3.4 Layer-dependent X-ray absorption spectroscopy and X-ray magnetic circular dichroism of atomically thin $CrSiTe_3$

XAS (Figure 3.2a) and XMCD (Figure 3.2b) measurements of different thicknesses of $CrSiTe_3$ (1 L, 3 L, 10 L and bulk) were performed at 2 K in an applied OOP field of 3 T . Although the XAS spectra qualitatively look similar, slight deviations in the Cr L_3 pre-edge and L_2 higher-energy edge occur for 10 L and below. Contrarily, the XMCD signal progressively decreases in magnitude for the thinner flakes (Figure 3.2a). In Figure 3.2b, which shows the XMCD spectra from the different thicknesses normalized to the respective peak amplitudes, a small Te M_5 peak can be seen at a photon energy of about 574 eV, confirming a hybridization between the Te $5p$ and Cr e_g bonding states. This is in contrast to $CrGeTe_3$, which has a larger single-ion anisotropy and much smaller XMCD signal at the Te M_5 edge [70]. In $CrSiTe_3$, the hybridization and superexchange between the Cr and Te could reflect the 2D aspect of the magnetic ordering, which manifests as 2D Ising-type ferromagnetism in the bulk limit [63, 64].

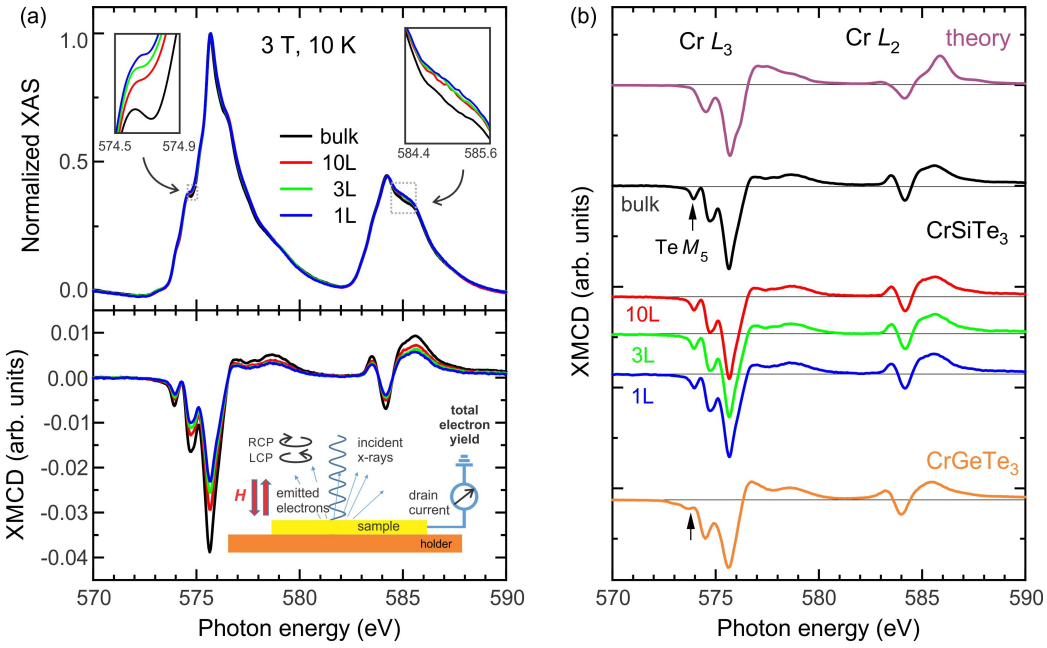


Figure 3.2: a) Cr $L_{2,3}$ XAS and XMCD data of 1 L, 3 L, and 10 L and bulk $CrSiTe_3$ obtained at 10 K in an applied field $\mu_0 H$ =3 T. The inset shows the experimental geometry consisting of normally incident X-rays and a field H applied along the beam. In TEY mode, the drain current is recorded. A small layer dependence of the XAS can be seen at photon energies of 574.5—574.9 eV and 584.4—585.6 eV. On the other hand, the XMCD show a clear thickness dependence when normalized to the corresponding XAS, which originates from changes in the saturation magnetization $\widetilde{M}_{\mathrm{sat}}$. These data were obtained by Ryuji Fujita and Dr. Javier Herrero-Martin at BOREAS (BL29) at ALBA Synchrotron. **b)** Comparison of the theoretical multiplet spectrum at the Cr $L_{2,3}$ edge for $CrSiTe_3$ with bulk (black), 10 L (red), 3 L (green), and 1 L (blue) $CrSiTe_3$. When normalized to their respective maxima, the spectral shape of the peaks look similar, and do not have an obvious thickness dependence. For comparison, an experimental Cr $L_{2,3}$ spectra of bulk $CrGeTe_3$ is shown, for which a reduced Te M_5 peak (indicated by the black arrow) indicates Cr-Te hybridization.

3.5 Layer-dependent spin and orbital magnetic moments

The spin and orbital magnetic moments m_l and m_s were determined for 1 L, 3 L, 10 L and bulk $CrSiTe_3$ at 3 T using the sum rules [67]; m_s was scaled with (A_3 −

$2A_2$), where A_3 and A_2 are the integrated areas beneath the L_3 and L_2 peaks, respectively, and m_l was scaled with $(A_3 + A_2)$. Here, A_3 and A_2 have opposite signs as the spin and orbit are coupled oppositely for $p_{3/2}$ and $p_{1/2}$ core levels. For the bulk layer, taking the number of $3d$ electrons to be $n_d = 3.5$, $m_l = (-0.055 \pm 0.05)$ μ_B/Cr atom and $m_s = (2.86 \pm 0.25)$ μ_B/Cr atom [65]. The values for m_l and m_s are listed in Table 3.1; m_s monotonically decreases for the thinner layers, in accordance with the commonly observed reduction of T_C [4, 6–8].

	1 L	3 L	10 L	Bulk
m_s (μ_B/Cr atom)	1.7	1.89	2.17	2.86
m_l (μ_B/Cr atom)	-0.033	-0.036	-0.041	-0.055
m_l/m_s (10^{-2})	-1.94	-1.91	-1.89	-1.92

Table 3.1: Spin and orbital moments of the Cr atom in atomically thin and bulk $CrSiTe_3$ at 10 K in an applied OOP field $\mu_0 H_{OOP}$=3 T. The XAS and XMCD spectra were obtained by Ryuji Fujita and Dr. Javier Herrero-Martin at BOREAS (BL29) at ALBA Synchrotron.

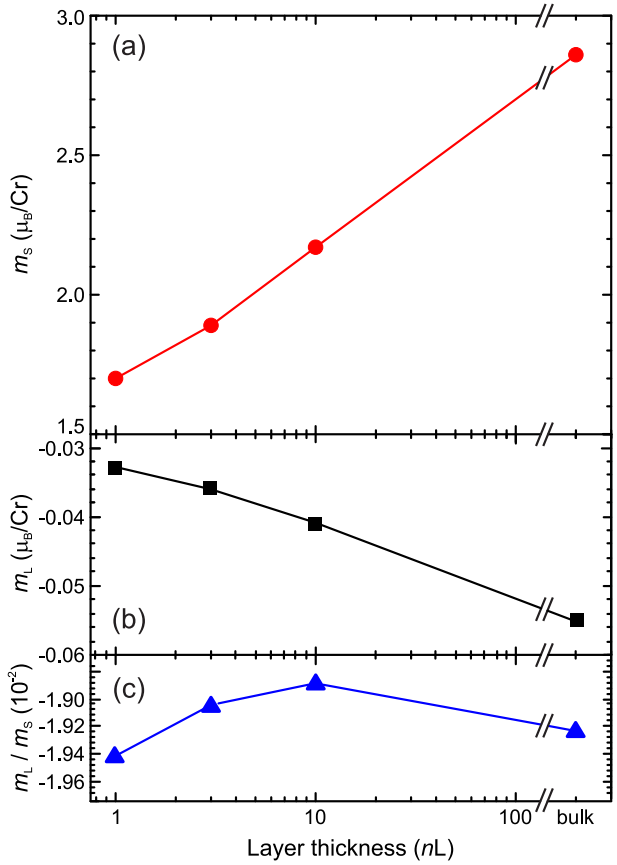


Figure 3.3: a) Spin (m_s) and **b)** orbital (m_l) moments of Cr in atomically thin and bulk $CrSiTe_3$ at 10 K in an applied field $\mu_0 H_{OOP} = 3$ T. **c)** The ratio m_l/m_s monotonically increases in magnitude for thicknesses below 10 L.

3.6 Layer-dependent ferromagnetic hysteresis

Magnetic hysteresis loops obtained at the Cr L_3 edge show soft ferromagnetism for bulk, 10 L and 3 L $CrSiTe_3$, while no opening of the hysteresis loop can be observed for 1 L $CrSiTe_3$, demonstrating that monolayer ferromagnetism is not stable for this material at 10 K (Figure 3.4) [71]. Bulk $CrSiTe_3$ undergoes a paramagnetic-ferromagnetic phase transition at $T_C \approx 33$ K with a weak easy-axis anisotropy [61]. The soft bulk ferromagnetism, which is characterized by extremely small H_c and remnant magnetization, also has wasp-waist characteristics, which can originate from domains of different sizes with different mag-

netic orientations as found in superparamagnetic nanoparticles with a blocking temperature below 300 K [72]. In other words, the bulk hysteresis is a combination of a paramagnetic response described by the Langevin function, along with the more open hysteresis of domains of varying orientation.

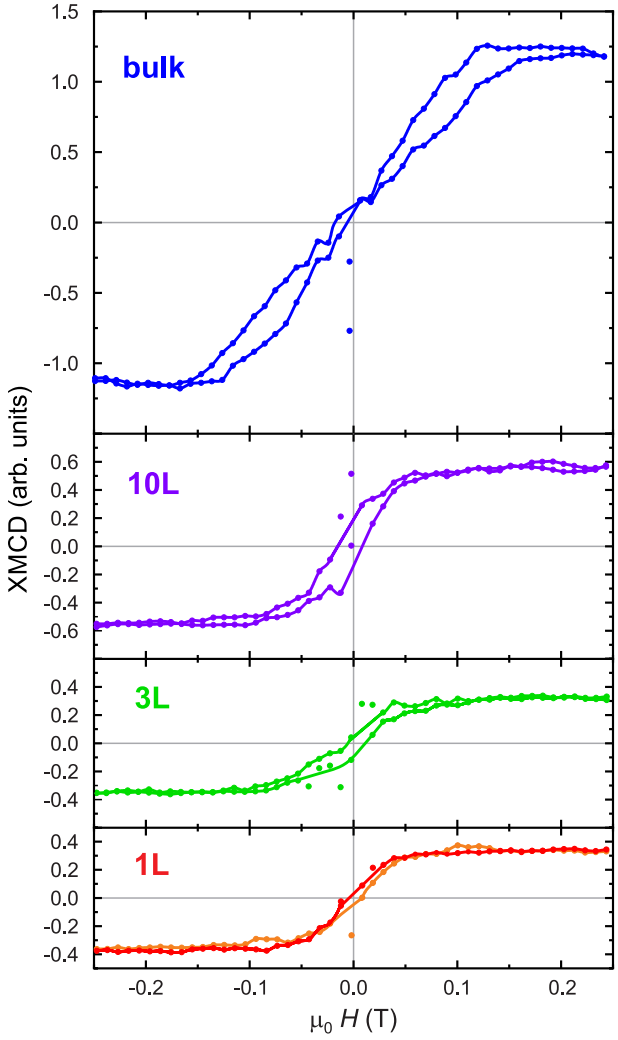


Figure 3.4: Ferromagnetic hysteresis obtained at the Cr L_3 edge for 1 L, 3 L, 10 L and bulk $CrSiTe_3$. While H_c is finite for 3 L, 10 L and bulk $CrSiTe_3$, the hysteresis loop is closed for 1 L $CrSiTe_3$, and strongly resembles a paramagnetic response. The solid lines represent a rolling average over the measured data points. Spurious low-field data points, which originate from changes in the photoelectron emission at low applied magnetic field, are disregarded in the rolling average. The measurement temperature was 10 K. The data were obtained by Ryuji Fujita and Dr. Javier Herrero-Martin at BOREAS (BL29) at ALBA Synchrotron.

3.7 Saturation magnetization and spin moment

The decrease of the spin moment m_s (Table 3.1) and decrease of H_{sat} (Figure 3.4) for thinner layers of $CrSiTe_3$ correspond to a reduction of T_C in the atomically thin limit and also varying magnetic domain structures.

In detail, for bulk $CrSiTe_3$, the relatively large spin moment $m_s = 2.86\,\mu_B$/Cr atom and large H_{sat} increases K_d, for which it is more energetically favorable for the magnetism to break up into domains. However, for atomically thin $CrSiTe_3$, the reduction of m_s and H_{sat} makes it less energetically costly for the magnetization to be uniform across larger length scales, resulting in single domains with easy-axis anisotropy for atomically thin flakes.

3.8 Orbital to spin moment ratio

The ratio m_l/m_s reveals some fundamental parameters in magnetic systems, including the magnetic anisotropy, $\langle T_z \rangle$, or e_g character in the $3d$ wavefunction. These parameters can be correlated to changes in the ratio m_l/m_s of Cr $3d$ electrons, as several effects, including n_h and changing H_{sat} cancel out in this ratio. Figure 3.3 and Table 3.1 show that the magnitude of m_l/m_s increases below 10 L. The magnitudes of m_l and m_s decrease for thinner flakes, which is expected as m_l and m_s are coupled by spin-orbit coupling. The opposite sign of m_l and m_s are expected by Hund's rule, for which m_l and m_s are aligned antiparallel for a less than half-filled d shell [73].

For 10 L $CrSiTe_3$, $m_l/m_s \approx -0.019$, while the magnitude of m_l/m_s increases by about 2.5% for 1 L. This enhancement of m_l/m_s in the atomically thin limit could originate from an enhanced easy-axis anisotropy, as the easy magnetization direction always has the largest orbital moment [66]. However, this is rather unlikely, as the ferromagnetic hysteresis loops in Figure 3.4 progressively become more soft in the atomically thin limit; contrarily, magnetic materials with large anisotropy are characterized by rectangular hysteresis loops, where all of the magnetization switches at H_c [8, 17].

An increase in $\langle T_z \rangle$, where the tensor T gives the anisotropy of the spin moment m_s due to the coupling between the spin and charge quadrupole, is also plausible; structural changes within the atomically thin limit [74] could induce changes in $\langle T_z \rangle$. A quick way to check for such changes is Raman spectroscopy where shifts in Raman peaks and also peak profile can be correlated to structural changes in 2D materials, and will be discussed in greater detail in Chapter 4.

The enhancement of m_l/m_s in the atomically thin limit could also originate from increased hybridization between Cr e_g and Te $5p$ electrons, which is corroborated by the Te M_5 peak in the XMCD, meaning that there are spin-polarized holes in the Te $5p$ band. The inset in the top panel of Figure 3.2a shows that the Cr XMCD L_3 spectra and L_2 spectra gain intensity at 576.5—580 eV and 585—587 eV, respectively, roughly coinciding with increased intensity at the high energy sides of the absorption peak for multiplet calculations which account for hybridization. Therefore, the increase in m_l/m_s could indicate pronounced hybridization between Cr and Te in atomically thin $CrSiTe_3$.

3.9 Conclusion

High-field XAS and XMCD spectroscopy was used to characterize changes in the magnetic moments m_l and m_s, and the ratio m_l/m_s as a function of layer thickness for $CrSiTe_3$, a vdW ferromagnet with 2D Ising-type ferromagnetism in the bulk. Although subtle, the enhancement of the ratio m_l/m_s in the atomically thin limit demonstrates a layer-dependence of magnetic properties beyond a trivial reduction of T_C even for magnetic vdW materials with weak interlayer coupling, which could be due to enhanced hybridization.

4 | Strained ferromagnetism at a Fe_3GeTe_2/α-In_2Se_3 heterojunction

4.1 Magnetism in bulk and two-dimensional Fe_3GeTe_2

Fe_3GeTe_2 is a prototypical vdW ferromagnet with a relatively high bulk T_C of 220 K and a monolayer T_C of 130 K [8]. The ferromagnetism is characterized by competition between the large perpendicular magnetic anisotropy (PMA) and dipolar interaction, producing meander-style domains in the bulk limit and a single domain in the atomically thin limit, as the large PMA makes the formation of domains energetically costly, forcing a uniform magnetization. As a result, the magnetic hysteresis is characterized by large H_c on the order of 1 T for atomically thin single-domain Fe_3GeTe_2 [8, 17].

Several properties including large H_c, PMA, and metallic conductivity make few-layer Fe_3GeTe_2 unique among atomically thin vdW magnets, which are usually insulators in the magnetic state. Current-induced reduction of H_c and electrical control of the magnetic anisotropy in Fe_3GeTe_2 has already been experimentally demonstrated [17, 25, 75]. The large anisotropy and metallic conduction also make Fe_3GeTe_2 an ideal material for MTJs [16]. For the other atomically thin vdW magnets [6, 7, 76, 77] which are wide-gap semiconductors, the electrical control of magnetic properties is more challenging. A general method which can tune the magnetic properties of atomically thin vdW magnets, regardless of their electrical conductivity, would be ideal.

4.2 Strain-tuning of two-dimensional materials

Strain-tuning of properties including bandgap [78] and carrier mobility [79] for a large range of TMDs, as well as H_c in Fe_3GeTe_2 [80] and VI_3 [77] has been demonstrated. Specifically, the application of tensile strain enhances H_c and T_C [81], while compressive strain suppresses the ferromagnetic ordering [82].

Density functional theory (DFT) calculations predicts a nearly linear correlation between the average magnetic moment of the unit cell and a biaxial tensile strain [83].

In most cases, the strain is formed or is applied by means of lattice mismatch at an epitaxial substrate-thin film interface [78], flexible substrate [77, 84–86], patterned substrate, local deformations made by AFM, or utilizing a piezoelectric substrate. However, inducing strain in 2D materials is challenging due to the intrinsically weak vdW interaction [87], meaning that some slippage will occur between adjacent layers [88]. Although the utilization of flexible substrates [77, 81, 89, 90] and piezoelectric substrates such as PMN-PT [47, 91] enables proof-of-principle investigations of strain-tuned magnetism in 2D materials, it is more difficult to investigate their intrinsic properties, as all of these methods rely on forces fundamentally different from the vdW interaction to induce strain. An outstanding question is whether it is possible to induce strain in a 2D material within the confines of an atomically smooth environment provided by hBN encapsulation. In this chapter, a novel method of straining Fe_3GeTe_2 by interfacing it with α-In_2Se_3, a vdW piezoelectric, is demonstrated.

4.3 Methods

4.3.1 Single crystal growth

Fe_3GeTe_2 and α-In_2Se_3 crystals were grown by Dr. Daniel Mayoh and Prof. Geetha Balakrishnan with CVT at the University of Warwick. Single crystalline hexagonal platelets of approximately $3 \times 3\,mm^2$ in the case of Fe_3GeTe_2 [92] and $2 \times 2\,mm^2$ sized hexagonal silvery-blue platelets in the case of α-In_2Se_3 [93] were obtained. The α-In_2Se_3 crystals were characterised by x-ray diffraction (XRD) and energy-dispersive x-ray spectroscopy (EDX). Compositional analysis of the crystals was carried out using EDX analysis, and was estimated to be $In_{1.96(5)}Se_{3.04(5)}$.

4.3.2 Mechanical exfoliation

Bulk α-In_2Se_3, Fe_3GeTe_2, graphite and hBN flakes were mechanically exfoliated in a glovebox with oxygen and water concentrations below 10 ppm. Thin flakes were identified via optical microscopy (Chapter 2.3), and were sequentially stacked over a conductive Si substrate by a PDMS-assisted transfer method [36].

4.3.3 Piezoresponse force microscopy characterization of a α-In_2Se_3 heterojunction

PFM measurements were performed by Dr. Alexander Kang-Jun Toh, Prof. Anjan Soumyanarayanan and Dr. Pin Ho at the Institute of Materials Research and Engineering (IMRE) in Singapore.

4.3.3.1 Instrumentation and setup

Single frequency vertical PFM measurements were performed on an exfoliated α-In_2Se_3 flake (75-125 nm) encapsulated in between top hBN (10 nm) and bottom hBN (17 nm) layers placed on a conductive p-Si substrate. In short, the setup consists of a scanning probe microscope within a variable temperature cryostat (Attocube systems). The employed Pt-Ir conductive tip (Nanosensors) had a radius of curvature <25 nm, spring constant of ≈3.6 N/m, and resonance frequency of 67.2 kHz. PFM measurements were performed at temperatures of 50 and 294 K with a stability of <20 mK.

4.3.3.2 Measurement procedures

First, the flake of interest was located via contact mode AFM imaging. Next, an a.c. drive voltage of V_{pp} = 10 V was applied to the tip while in contact with the sample surface to excite piezoresponse at an off-resonance frequency of 80 kHz (contact resonance ≈335 kHz). Off-resonance PFM was used to minimize topography crosstalk [94–96]. The amplitude and phase-shift of the tip-sample excitation, corresponding to the PFM signal, were detected using a lock-in amplifier. PFM images were acquired at each imaging temperature over a 20 μm

region with 256 sampling points.

4.3.4 Raman characterization of α-In_2Se_3 heterojunctions

Access to the Raman instrumentation was granted by Dr. Tina Geraki of I18 at the Diamond Light Source. hBN-encapsulated Fe_3GeTe_2, α-In_2Se_3, and graphite flakes were characterized with Raman spectroscopy at room temperature. The data were collected using an objective lens with 100x magnification. The laser wavelength was λ = 473 nm. The laser power was limited to 3.5 mW to limit laser-induced damage of the sample. The accumulation time was 120 s.

4.3.5 Density functional theory calculations of effective exchange interaction, uniaxial anisotropy, Curie temperature and lattice parameter

First-principles DFT calculations with fully relativistic projected augmented wave pseudopotentials were performed with Quantum ESPRESSO [97] by Dr. Gautam Gurung at Trinity College, University of Oxford. The exchange and correlation effects were treated within the local density approximation (LDA). Generally, the exact formulation of the exchange-correlation functional is unknown, and approximations of various sophistication, including LDA and generalized gradient approximation, have been used to model electronic structures in various vdW ferromagnets. The main drawback of LDA is its failure to accurately model many-body electron-electron potentials, which can manifest as underestimations in bandgap and inaccurate calculations of electronic structures in correlated materials [98]. While dynamical mean-field theory is better-suited to model such many-body interactions, it is computationally more expensive than DFT calculations based on approximations of the exchange-correlation functional [98]. Alternatively, a functional inspired by the Hubbard model, LDA+U, may also be incorporated in calculations of the electronic structure in correlated materials [98]. For Fe_3GeTe_2, DFT calculations incorporating LDA were found to be most consistent with experimental results [99]. The plane-wave cut-off energy of 70 Ry and a $18 \times 18 \times 1$ k-point mesh in the irreducible Brillouin zone

were used in the calculations. Spin-orbit coupling was included in all electronic structure calculations.

Tight-binding Hamiltonians were constructed using Wannier90 [100] and then TB2J [101] was used to calculate the exchange parameters considering nearest neighbors within 4.80 Å. T_C was calculated by using atomistic spin dynamics as implemented in Vampire [102].

4.4 Magnetic domain structure in a Fe_3GeTe_2/α-In_2Se_3 heterojunction

Ferromagnetism within Fe_3GeTe_2/α-In_2Se_3 heterojunctions were characterized with XPEEM at the UE49-PGMa beamlime at BESSY II (Helmholtz-Zentrum Berlin) [103] and at beamline I06 at Diamond Light Source. In detail, XPEEM measurements at the Fe L_3 edge (706.2 eV) were performed from 50-200 K.

α-In_2Se_3 crystallizes in the $R3m$ structure and has piezoelectric domains with both IP and OOP polarizations at room temperature [84]. Notably, such piezoelectric polarization is retained down to the monolayer [86]. In addition, ferroelectric field effect transistors made from α-In_2Se_3 have a high on-off ratio [104], which, in combination with its robust piezoelectric properties, make it a strong candidate material for in-memory computing applications which overcome the von Neumann bottleneck [105]. These favorable properties of α-In_2Se_3 motivate its incorporation in magnetic vdW heterojunctions.

For a heterojunction consisting of a Fe_3GeTe_2 flake of 9 nm thickness and an α-In_2Se_3 flake of 22 nm thickness (Figure 4.1), there is a significant increase in the density of domain walls compared to the surrounding area, which consists entirely of decoupled Fe_3GeTe_2 (Figure 4.2b). The magnetic domain structure within the decoupled Fe_3GeTe_2 homojunction is characterized by meander domains, which form as a result of the competition between K_u and K_d (Figure 4.2b). The enhanced density of domain walls within the heterojunction could reflect a change in K_d, which is proportional to $\widetilde{M}_{sat}^2$ [21]. For the class of itinerant vdW ferromagnets Fe_xGeTe_2 (x = 3, 4, 5), $\widetilde{M}_{sat}$ varies from 1.4 μ_B/Fe [106] to

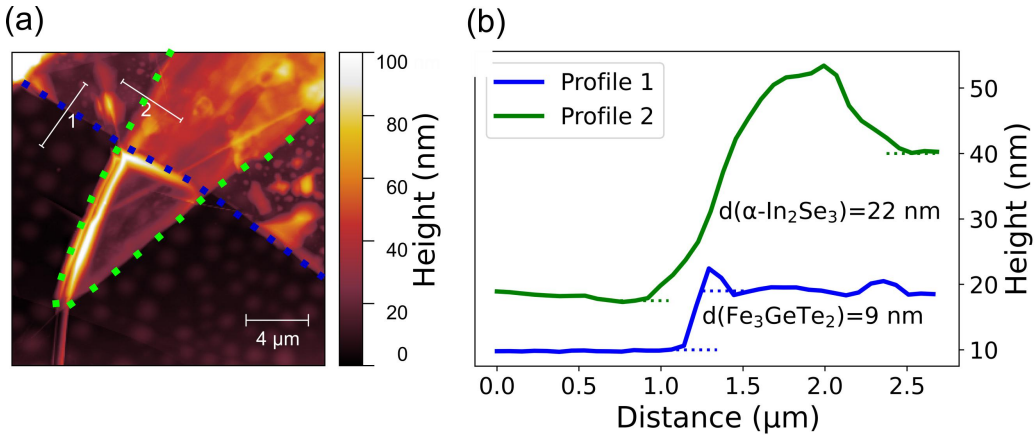


Figure 4.1: AFM scans of surface topography of a Fe_3GeTe_2/α-In_2Se_3 heterojunction at room temperature. Line profiles of the Fe_3GeTe_2 (blue) and α-In_2Se_3 (green) show that the thicknesses are 9 nm and 22 nm, respectively.

1.9 μ_B/Fe [107].

If there is a reduction of $\widetilde{M}_{sat}$ within the heterojunction, there would also be a corresponding decrease in the XMCD signal. However, a comparison of line profiles of the XMCD values within the heterojunction and homojunction shows that there is no discernible difference in the XMCD (Figure 4.3). In other words, if $\widetilde{M}_{sat}$ of Fe_3GeTe_2 changes when interfaced with α-In_2Se_3, the change is below the detection threshold of XPEEM at a measurement temperature of 50 K.

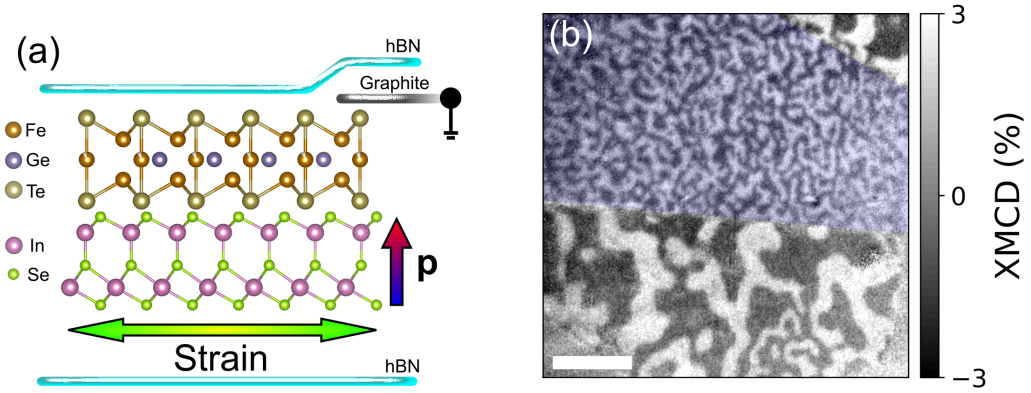


Figure 4.2: a) Side-view schematic showing the Fe_3GeTe_2/α-In_2Se_3 heterojunction encapsulated between thin hBN layers. A graphite electrode provides a conductive pathway to the XPEEM sample holder. **b)** XPEEM image of interfacial coupling within the Fe_3GeTe_2/α-In_2Se_3 heterojunction obtained at 50 K. Scale bar = 3 µm. The heterojunction is shaded in pale blue. The XPEEM data were obtained by Ryuji Fujita, Dr. Alevtina Smekhova, Dr. Mohamad A. Mawass and Dr. Florian Kronast at the UE49-PGMa beamline at BESSY II.

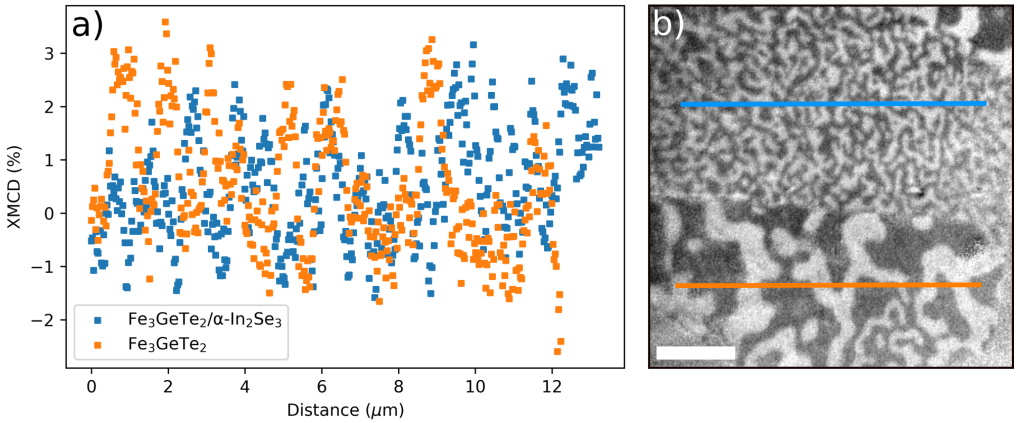


Figure 4.3: a) XMCD line profiles of the Fe_3GeTe_2/α-In_2Se_3 heterojunction and Fe_3GeTe_2 homojunction obtained at 50 K. The line profiles are shown in **b)**. Scale bar = 3 µm.

Alternatively, the increase in domain wall density may also be due to reduced A, which would also reduce $\sigma_w \propto \sqrt{AK_u}$, making it less energetically costly to form

more domains per unit area. Also, a slight reduction of K_u will also reduce σ_w. However, the lack of any intermediate XMCD contrast in Figure 4.2b indicates that a large uniaxial anisotropy is retained within the heterojunction.

4.5 Reduction of ferromagnetic Curie temperature in a Fe_3GeTe_2/α-In_2Se_3 heterojunction

For reduced A, a reduction in T_C, which is proportional to A, should also occur [21]. XPEEM images of the magnetic domains were obtained at temperatures varying from 145 to 190 K (Figure 4.4). At 145 K, magnetic domains are present in both the heterojunction and homojunction, while at 170 K, small areas encircled by the white dashed line appear to be no longer magnetic. At 175 to 190 K, these non-magnetic patches continue to expand in area, until there is barely any magnetic signal remaining in either the Fe_3GeTe_2 homojunction or the Fe_3GeTe_2/α-In_2Se_3 heterojunction (Figure 4.4f). The maximum difference between the T_C of the heterojunction and that of the homojunction is determined by noting the initial observation of non-magnetic areas at 170 K, and the nearly total disappearance of all XMCD at 190 K, and is estimated to be about 20 K.

At 177.5 K, the domains which are encircled by the pale blue line, which lies within the heterojunction, are modulated by geometric features shown by the green arrows, which resemble a three-fold rotational symmetry, which is consistent with the $R3m$ spacegroup of α-In_2Se_3 [86]. Presumably, the ferromagnetic domains are coupling to the underlying piezoelectric domain structure.

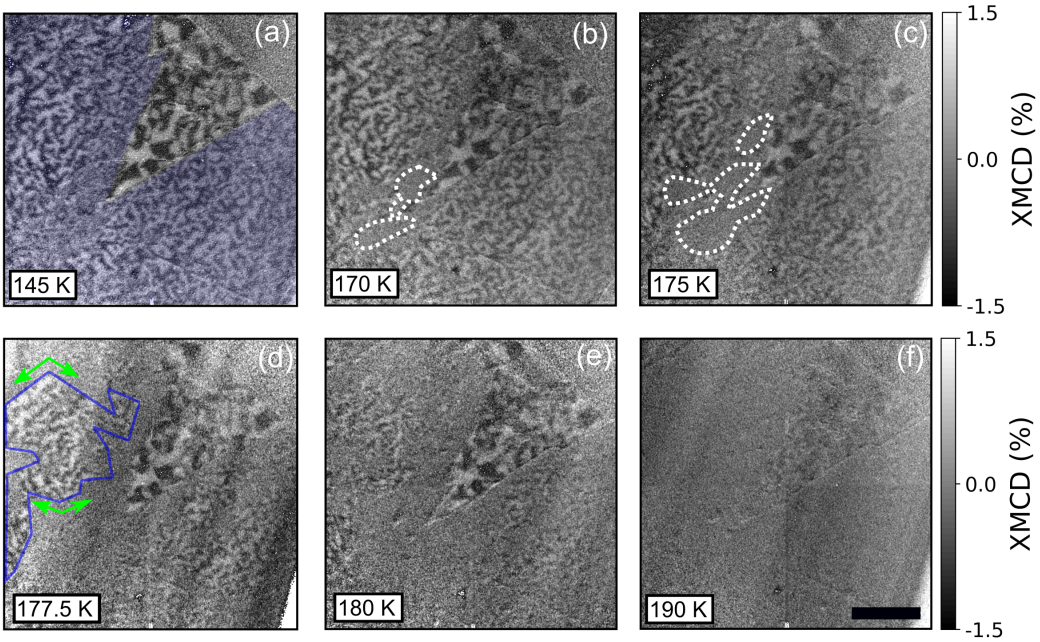


Figure 4.4: Reduction of ferromagnetic T_C in a Fe_3GeTe_2/α-In_2Se_3 heterojunction (shaded in pale blue). XPEEM images of ferromagnetic domains in the heterojunction and homojunction were collected at **a)** 145 K, **b)** 170 K, **c)** 175 K, **d)** 177.5 K, **e)** 180 K and **f)** 190 K. At 170 K, the magnetic contrast vanishes in a small area indicated by the white dashed line, which then expands to a larger area at 175 K. At 177.5 K, the magnetic domains encircled by the pale blue line are modulated by geometric features indicated by the green arrows. Scale bar = 3 µm. The XPEEM data were obtained by Ryuji Fujita, Dr. Alevtina Smekhova, Dr. Mohamad A. Mawass and Dr. Florian Kronast at the UE49-PGMa beamline at BESSY II.

4.6 Density functional theory calculations of effective exchange interaction, uniaxial anisotropy and estimation of ferromagnetic Curie temperature for varying lattice parameter

A lattice strain corresponding to a reduction of T_C by 20 K, as explained above, was estimated by DFT calculations and atomistic spin dynamics. Specifically, DFT was used to calculate the effective exchange interaction $J = \sum_a Z_a J_{ij}^a$ [108] and K_u for monolayer Fe_3GeTe_2 as a function of lattice parameter a. Subsequently, J and K_u were used to estimate the T_C corresponding to varying a. A linear fit of the data in Figure 4.5c show a compressive strain $\epsilon = 0.4\%$ corresponds to a decrease of 20 K, from 95 to 75 K. Here, ϵ is calculated with respect to the lattice parameter of the homojunction, $a_0 = 4.01$ Å [92].

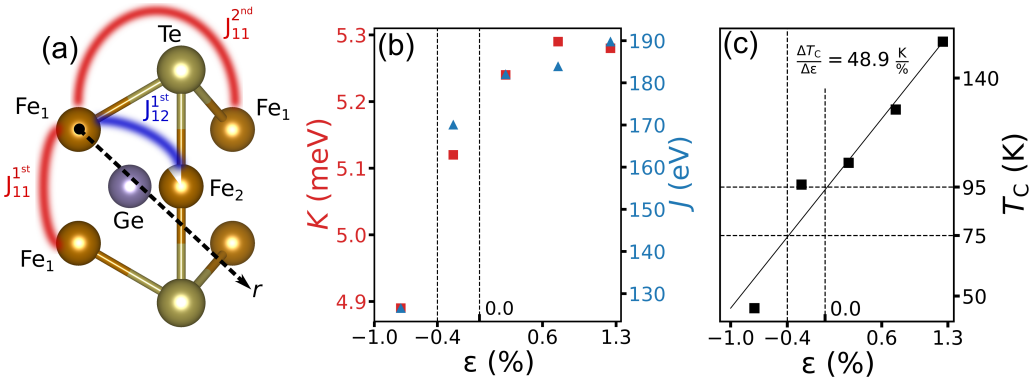


Figure 4.5: DFT calculations of K_u and J at the Fe_1 site for varying strain ϵ. **a)** Illustration of Fe_1 and Fe_2 sites and respective exchange interactions J_{11} and J_{12} for monolayer Fe_3GeTe_2. Exchange interactions amongst nearest neighbors are considered for $r = 4.80$Å. **b)** K_u and J are shown for varying strain ϵ. **c)** T_C as a function of strain ϵ. A decrease of 20 K, from 95 to 75 K, corresponds to a compressive strain $\epsilon = 0.4\%$. The DFT calculations were performed by Dr. Gautam Gurung at Trinity College, University of Oxford.

4.7 Enhancement of magnetic coercivity in a Fe_3GeTe_2/α-In_2Se_3 heterojunction

Within the Fe_3GeTe_2/α-In_2Se_3 heterojunction, H_c increases (Figure 4.6). Field reversal is only observed for the homojunction, while the heterojunction retains its initial magnetization. In detail, a magnetic state was initialized by cooling the sample across T_C from 300 to 50 K in an OOP field $\mu_0 H_{OOP} = -13.2$ mT, saturating the magnetization in the antiparallel direction relative to the surface normal. A subsequent field pulse of opposite polarity, $\mu_0 H_{OOP} = +88$ mT, was applied, resulting in only a partially field-reversed state.

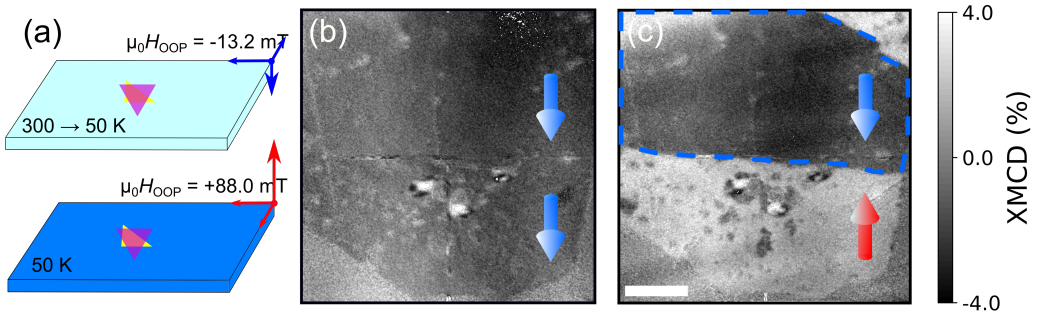


Figure 4.6: Enhanced H_c within the Fe_3GeTe_2/α-In_2Se_3 heterojunction at 50 K. **a)** The magnetic state is initialized by cooling the sample from 300 to 50 K in a field $\mu_0 H_{OOP} = -13.2$ mT, as shown in **(b)**. At 50 K, a field of opposite polarity, $\mu_0 H_{OOP} = +88$ mT, is applied, resulting in a partially field-reverse state, shown in **(c)**. Scale bar = 3 µm. The XPEEM data were obtained by Ryuji Fujita, Dr. Alevtina Smekhova, Dr. Mohamad A. Mawass and Dr. Florian Kronast at the UE49-PGMa beamline at BESSY II.

As a first approximation, consideration of the Stoner-Wolfarth model, for which H_c is proportional to K_u [109] implies an increase in K_u within the heterojunction. However, the increased domain wall density in the virgin state (Figures 4.2b and 4.4) would incur an additional energy cost $\sigma_w \propto \sqrt{AK_u}$. In addition, an increase in K_u would likely result in an enhanced T_C [17], which is contrary to the temperature-dependent magnetization data shown in Figure 4.4. Instead, it is rather likely that extrinsic effects including magnetostriction are behind the

enhanced H_c.

4.8 Interfacial strain in α-In_2Se_3 heterojunctions

Interfacial strain within the Fe_3GeTe_2/α-In_2Se_3 heterojunction is characterized by comparison to structural changes revealed by Raman spectroscopy in a graphite/α-In_2Se_3 heterojunction. In particular, the Tuinstra-Koening relation, $1/L_a \propto I(D)/I(G)$, where $I(D)$ and $I(G)$ are the respective intensities of the D and G Raman peaks and L_a is the crystallite size, indicates the amount of disorder in graphite [110]. Such disorder can originate from point defects induced by ion bombardment [111, 112] and dislocations [113], or grain boundaries [114] in nanocrystalline graphite. The chances of a chalcogen diffusing across the vdW gap between graphite and α-In_2Se_3 are negligible. Therefore, $I(D)/I(G)$ can be considered to characterize the concentration of grain boundaries in graphite/α-In_2Se_3, rather than point defects.

In detail, the Raman spectra of graphite include the $2D$, G and D peaks, indicating the presence of finite disorder [110]. The lack of a D' peak, peak attenuation, or broadening [111] indicate that the amount of disorder is between that of graphite and nanocrystalline graphite, for which the Tuinstra-Koening relation is valid [51]. The lack of peak shifts or splittings (Figure 4.7), as observed for graphene films strained over a flexible substrate [89, 90], can be attributed to sample-dependent piezoelectric polarization as well as the superlubricity of incommensurately stacked graphite [115, 116].

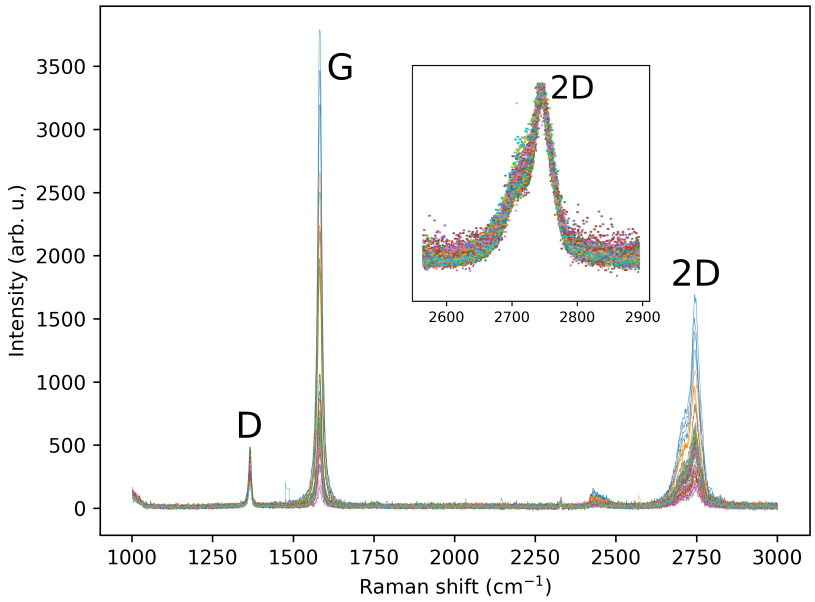


Figure 4.7: D, G and $2D$ Raman modes collected from different areas within the graphite homojunction and graphite/α-In_2Se_3 heterojunction at 300 K. Normalized $2D$ peak intensities obtained from the different areas are shown in the inset. No mode shifts or peak splittings are visible among these spectra.

The reduction of $I(D)/I(G)$ for the left part of Figure 4.8a suggests a reduction of the density of grain boundaries in response to a compressive strain, while a slight enhancement of $I(D)/I(G)$ at the tip of the α-In_2Se_3 flake implies an increase in the density of grain boundaries, which would originate from a tensile strain. The variation of $I(D)/I(G)$ may be a result of varying polarization of the underlying piezoelectric domains within the α-In_2Se_3, which could be due to varying thicknesses as seen in the AFM scan of the surface topography (Figure 4.9).

In one Fe_3GeTe_2/α-In_2Se_3 heterojunction sample, shifts of the Raman modes of Fe_3GeTe_2 indicate a tensile strain (Figure 4.8d). Specifically, a blueshift of the Fe_3GeTe_2 E_g^2 mode, $\Delta\omega_1 = +3.5$ cm^{-1}, and a redshift of the Fe_3GeTe_2 A_g^1 mode [117], $\Delta\omega_2 = -9.2$ cm^{-1} are observed at 300 K. A direct comparison to other TMDs, including MoS_2 and WS_2, indicate a remarkably large tensile strain of 2-3% (Table 4.1).

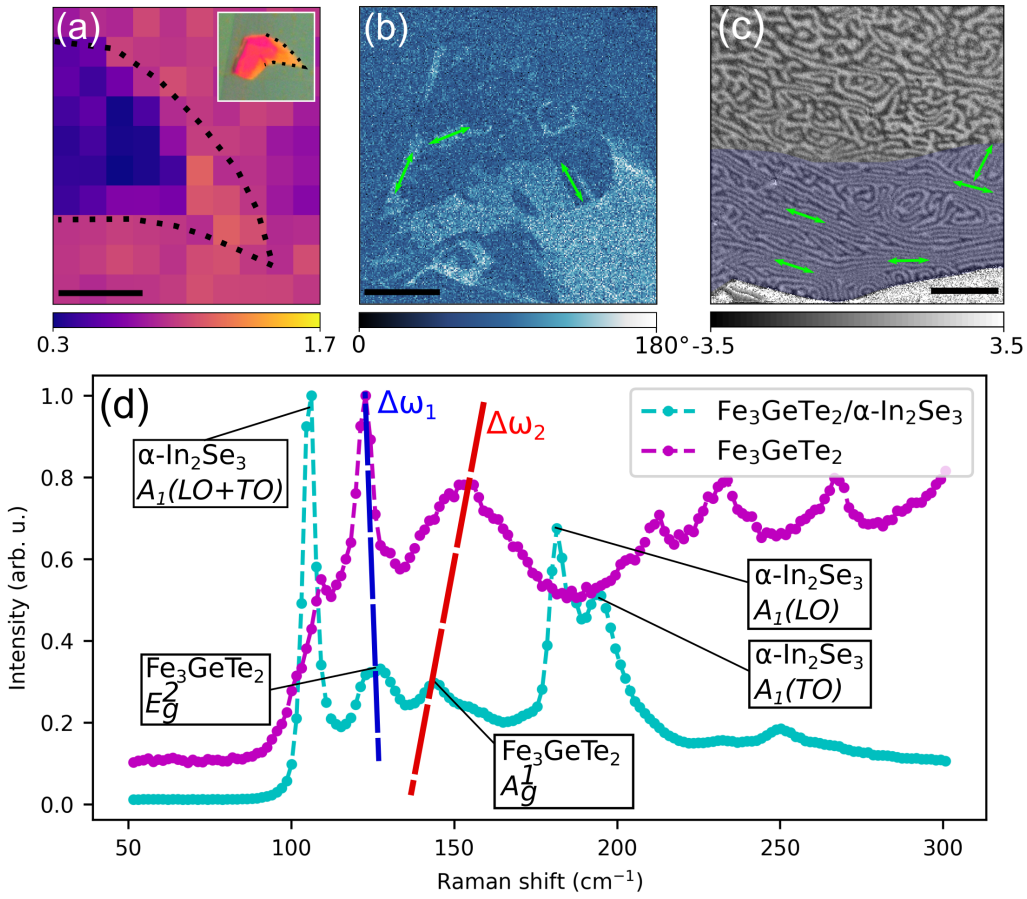


Figure 4.8: Interfacial strain within α-In_2Se_3 heterojunctions. **a)** Plot of $I(D)/I(G)$ of a graphite/α-In_2Se_3 heterojunction encapsulated between hBN obtained at 300 K. There is a significant reduction of $I(D)/I(G)$ within the left part of the flake, while a marginal enhancement is observed near the tip. The α-In_2Se_3 flake is outlined by the dashed black line, corresponding to the optical micrograph shown in the inset. Scale bar = 5 µm. **b)** PFM phase response of an α-In_2Se_3 flake encapsulated between hBN obtained at 294 K. The α-In_2Se_3 flake thickness varies between 60 and 140 nm. Preferential orientations of piezoelectric domains are indicated by green arrows. Scale bar = 5 µm. PFM data were obtained by Dr. Alexander Kang-Jun Toh, Dr. Pin Ho and Prof. Anjan Soumyanarayanan at A*STAR. **c)** XPEEM image of magnetostrictive ferromagnetic domains within the Fe_3GeTe_2/α-In_2Se_3 heterojunction (shaded in pale blue) obtained at 100 K. Preferential alignment of ferromagnetic domains is indicated by green arrows. XPEEM data were obtained by Ryuji Fujita, Dr. Angadjit Singh, Emily Heppell, Dr. Dirk Backes and Dr. Francesco Macherrozzi at the I06 beamline at Diamond Light Source. Scale bar = 4 µm. **d)** Raman spectra of a Fe_3GeTe_2 homojunction and Fe_3GeTe_2/α-In_2Se_3 heterojunction obtained at 300 K. The E_g^2 mode blueshifts by $\Delta\omega_1 = +3.5\ \mathrm{cm}^{-1}$, and the A_g^1 mode redshifts by $\Delta\omega_2 = -9.2\ \mathrm{cm}^{-1}$.

Raman mode	$d\omega$ / $d\epsilon$
Graphene (G^+, G^-)	-31.4 ± 2.8 cm^{-1}/%, -9.6 ± 1.4 cm^{-1}/% [89]
α-In_2Se_3 ($A_1(LO+TO)$)	-1.97 cm^{-1}/% [119]
MoS_2 (E')	-3.8 cm^{-1}/% [88]
WS_2 (E^1_{2g})	-5.4 cm^{-1}/% [120]

Table 4.1: Changes in Raman shift and corresponding applied tensile strain for various 2D materials.

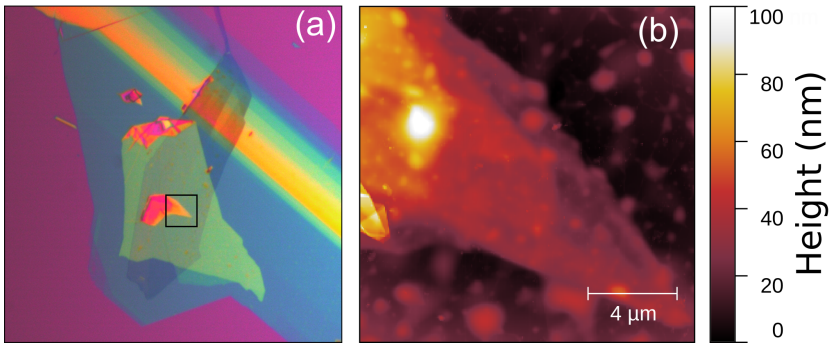


Figure 4.9: a) Optical micrograph of graphite/α-In_2Se_3 heterostructure. **b)** AFM topography scan of area indicated by the black square in **a)**.

It has been found that interfacial charge transfer within Fe_3GeTe_2-$CrGeTe_3$ heterostructures can modify the ferromagnetic coercivity in the Fe_3GeTe_2 layer [118]. Specifically, the transfer of electrons from Fe_3GeTe_2 to $CrGeTe_3$ reduces H_c. On the other hand, DFT calculations of Fe_3GeTe_2-α-In_2Se_3 heterostructures predict a rigid shift of the Fe_3GeTe_2 bands due to the change in the Fermi level, independent of ferroelectric polarization [99]. In comparison, the temperature dependence of ferromagnetic domains (Figure 4.4) show inhomogenous couplings with varying T_C, which cannot be accounted for by the charge transfer alone. Therefore, the Raman shifts (Figure 4.8d) and Table 4.1 are attributed to interfacial strain.

Evidently, structural changes and strain in graphite and Fe_3GeTe_2 are caused by the piezoelectric polarizations of the domains in α-In_2Se_3. To gain an idea of how large the piezoelectric domains are, PFM was performed on an α-In_2Se_3 flake encapsulated between thin hBN. The phase response data obtained at 300 K (Figure 4.8b) show piezoelectric domains which are 5-15 µm in length, sharing a com-

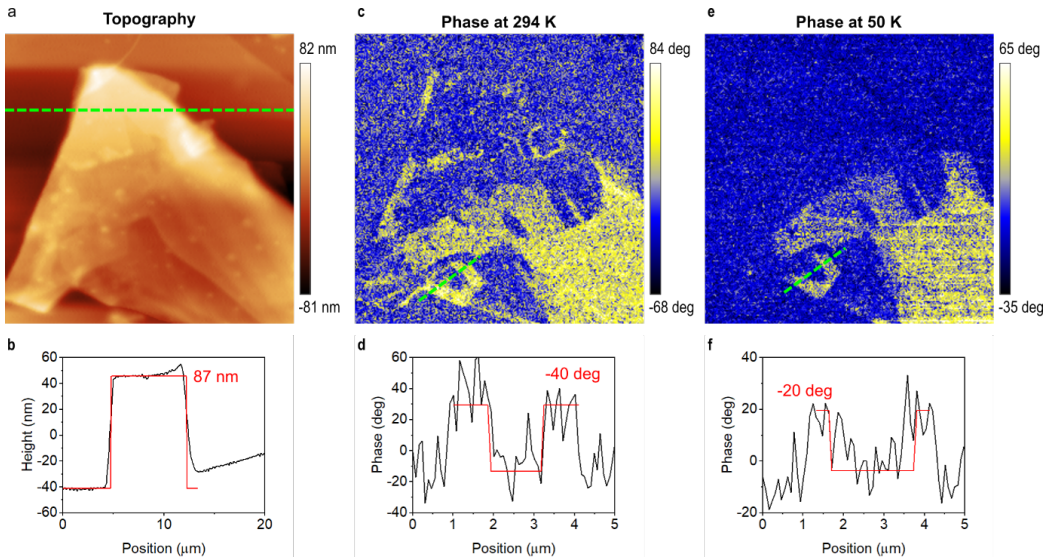


Figure 4.10: PFM characterization of α-In_2Se_3 encapsulated between hBN. **a,b)** Topography of the α-In_2Se_3 flake and profile line-cut (green dotted line) showing a step height of ≈87 nm. **c,d)** PFM phase contrast of the flake at 294 K, and profile line-cut of the up-polarized domain (blue) showing a domain extension of ≈1.2 μm and phase jump of 40°. **e,f)** PFM phase of the flake at 50 K, and profile line-cut of the up-polarized domain (blue) showing a domain size of ≈2.2 μm and a phase jump of 20°. This figure, which shows temperature-dependent PFM data, is the courtesy of Dr. Alexander Kang Jun Toh, Dr. Pin Ho, and Prof. Anjan Soumyanarayanan at the A*STAR in Singapore.

mon length scale with the modulations observed in the XMCD data at 177.5 K (Figure 4.4d). The piezoelectric domain walls are on the order of some nm [121], and are much too narrow to account for the size of these modulations.

The piezoelectric domains in Figure 4.8b also are preferentially oriented. For the hypothetical case where the piezoelectric domains lie fully IP, the domains should exhibit a three-fold rotational symmetry, in accordance with the $R3m$ space group [122, 123]. The OOP phase shift is only about 40°, as opposed to 180° for oppositely oriented OOP domains (Figure 4.10), implying the simultaneous existence of OOP and IP piezoelectric components [122, 123]. Thus, the preferential alignment of piezoelectric (Figure 4.8b) and ferromagnetic (Figure 4.4d) domains originates from a finite IP piezoelectric polarization.

4.9 Magnetostriction effects in a Fe_3GeTe_2/α-In_2Se_3 heterojunction

In general, strain can induce magnetostriction in ferromagnets. When coupled to the piezoelectric α-In_2Se_3, the magnetic domains in Fe_3GeTe_2 preferentially align along directions which are defined by a finite IP piezoelectric component within the α-In_2Se_3 layer. Such magnetostriction of materials with strong PMA in response to an IP strain could be explained by a small IP magnetization component induced by the stress anisotropy K_s.

For such a case, the magnetostriction constant needs to be relatively large [21]. Full spin reorientation transitions have been observed for crystalline ferromagnets, for which the magnetic domain walls are commensurate with grain boundaries of the neighboring stress states [124–127]. For the Fe_3GeTe_2/α-In_2Se_3 heterojunction, the magnetostriction (Figure 4.8c) is comparatively weak, as no full spin-reorientation transition is observed. Nevertheless, the previously derived compressive strain $\epsilon = 0.4\%$ can still induce a stress anisotropy $K_s = \frac{3}{2}\lambda_s\sigma = 0.38$ meV/Fe atom along the stress axis [21].

In detail, for a Fe_3GeTe_2 unit cell to experience a compressive force $\epsilon = -0.4\%$ along a, a force $F = C_{11}\Delta l = 2.7 \times 10^{-10}$ N is required along a [21], where $C_{11} = 134$ N/m, $\Delta l = 0.004a$, and $a = b = 4.01$ Å. For this force, the stress $\sigma = F/A = 6.0$ meV/Å^3, where $A = \sqrt{3}a/2 \times c/2$ is the cross-sectional area of the Fe_3GeTe_2 monolayer ($a = 4.01$ Å and $c = 16.3$ Å). The stress anisotropy constant is $K_s = 3/2\lambda_s\sigma = 5.05$ meV/Å^3 [128], where $\lambda_s = -559 \times 10^{-6}$ [128]. Finally, for the compressed unit cell, there are three Fe atoms in the unit cell volume $V = 226$ Å^3. Thus, the stress anisotropy constant $K_s = 0.38$ meV/Fe atom. This is less, but within the same order of magnitude as K_u= 0.844 meV/Fe atom [128], and is large enough to cause a reduction of the total magnetic anisotropy energy for compressive strains [128]. A deviation of the easy axis could be one reason for the enhanced H_c observed in Figure 4.6.

The presence of IP magnetization induced by the stress anisotropy K_s can be confirmed by the azimuthal dependence of the XMCD signal, which is propor-

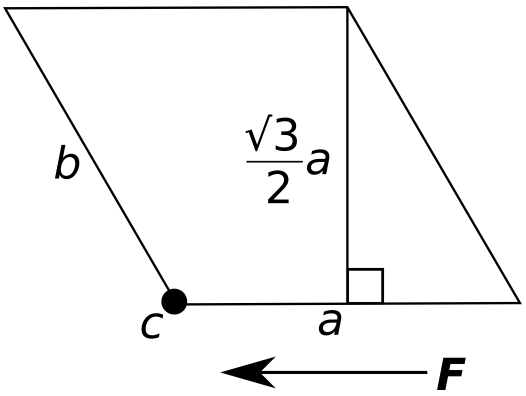


Figure 4.11: Schematic of Fe_3GeTe_2 unit cell. A force is applied along the a axis. The perpendicular cross-section has width $\sqrt{3}a/2$.

tional to $\vec{m} \cdot \vec{k}$. Specifically, for domains which are OOP, the XMCD signal is constant, while for domains which are IP, the XMCD signal is sinusoidal. In the present case, the IP magnetization was characterized for both the homojunction and heterojunction by collecting the XMCD signal at 0° and 90° azimuths [22] at 100 K, for which a reduction of the XMCD amplitude can be observed within the heterojunction (Figure 4.12b). This likely reflects a reduction of the average magnetic moment as the temperature of the sample approaches the T_C of the heterojunction. Correspondingly smaller values of A and K_u may facilitate an IP magnetization component within the heterojunction.

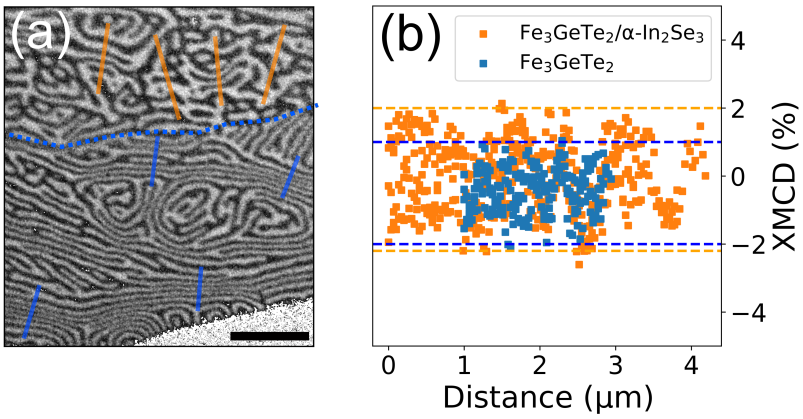


Figure 4.12: a) XMCD image showing preferential alignment of ferromagnetic domains within the Fe_3GeTe_2/α-In_2Se_3 heterojunction at 100 K. The heterojunction is demarcated from the homojunction by the blue dashed line. Scale bar = 3 μm. **b)** Line profiles, as indicated in **a)**, of XMCD obtained from the heterojunction (blue) and homojunction (orange). These XPEEM data were obtained by Dr. Dirk Backes, Dr. Angadjit Singh, Emily Heppell and Ryuji Fujita at the I06 beamline at Diamond Light Source.

A pronounced dependence of the XMCD signal on the azimuthal angle can be observed for the heterojunction (Figure 4.13); the difference between the XMCD signal collected at 0° and 90° azimuths, Δ_{XMCD}, exceeds a threshold $\delta \approx 0.55\%$ 10 out of 35 times within the heterojunction, compared to only 1 out 16 times for the homojunction. However, the presence of astigmatism in the XMCD data collected at 90°, which also contributes to Δ_{XMCD}, as well as the generally small width of the domains, obscures a definitive conclusion regarding the presence of IP magnetization within the heterojunction.

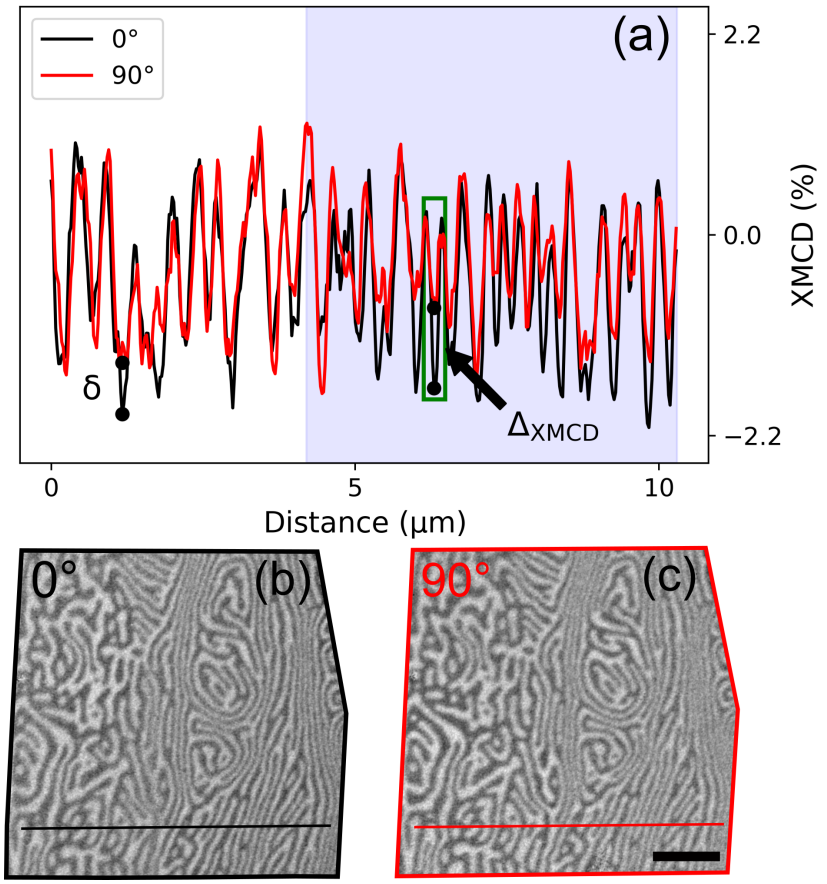


Figure 4.13: a) Line profiles of XMCD obtained within the heterojunction and homojunction at 0° and 90° azimuths. For the homojunction, a threshold $\delta \approx 0.55\%$ is exceeded 1 out of 16 times, while for the heterojunction, δ is exceeded 10 out of 35 times. XMCD images obtained at azimuthal angles of **b)** 0° and **c)** 90° at 100 K. Scale bar = 2 μm. These XPEEM data were obtained by Dr. Dirk Backes, Dr. Angadjit Singh, Emily Heppell and Ryuji Fujita at the I06 beamline at Diamond Light Source.

4.10 Conclusion

The strain-tuning of magnetism in the vdW ferromagnet Fe_3GeTe_2 was demonstrated via interfacial coupling to the vdW piezoelectric α-In_2Se_3. Despite the weak vdW interaction, changes in the ferromagnetic domain structure and Raman modes of Fe_3GeTe_2 were confirmed. In addition, the implementation of α-In_2Se_3 in straining graphite was also demonstrated. The incorporation of α-In_2Se_3 has the advantage that it may be readily incorporated into vdW heterostructures encapsulated between hBN, which plays an indispensable role in providing an atomically smooth environment and protection from ambient exposure. α-In_2Se_3 could potentially be integrated into a broader class of strain-tuned atomically thin vdW heterostructures such as MTJs.

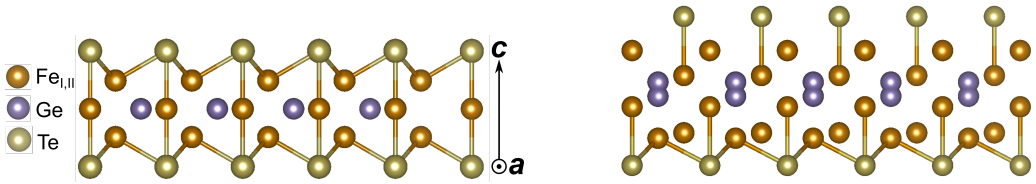
5 | Layer-dependent magnetic domains in atomically thin Fe_5GeTe_2

5.1 Fe_5GeTe_2: a weak-anisotropy van der Waals ferromagnet with high Curie temperature

As discussed in Chapter 1 and in Chapter 3, the magnetic anisotropy can play a large role in stabilizing 2D ferromagnetism, as the OOP exchange interaction, $J_\perp$, is greatly reduced in atomically thin vdW magnets. For example, in Fe_3GeTe_2, a large PMA forces a homogeneous magnetization for thin flakes [8]. It would therefore be interesting to see if a bulk vdW magnet with weak PMA can retain magnetic order in the atomically thin limit. In this chapter, the ferromagnetism in the weak-PMA vdW magnet, Fe_5GeTe_2, will be discussed in detail.

Fe_5GeTe_2 has a relatively high bulk T_C ranging from $270 - 330$ K, depending on the thermal history of the sample. Quenching Fe_5GeTe_2 in an ice-water bath from the growth temperature will reduce the stacking fault density, and further cooling below 100 K will enhance T_C to 310 K [46] (Chapter 6.3.1). The unit cell of Fe_5GeTe_2, which has three Fe sublattices and split Ge sites (Figure 5.1b), likely hosts strong intralayer exchange interactions, which are confined to one monolayer of Fe_5GeTe_2. Therefore, the thermal expansion or contraction of the lattice will influence the 2D ferromagnetism [129]. Note that there are respectively two and three inequivalent Fe sites in Fe_3GeTe_2 and Fe_5GeTe_2, which are not explicitly shown for the sake of simplicity.

Thus, the magnetism of Fe_5GeTe_2 is far from trivial, and a consistent picture describing the magnetism has not been established for even the bulk limit [46, 130, 131]. For example, crystals procured from Prof. Yanfeng Guo (ShanghaiTech University) have a weak easy-axis anisotropy [22], while those obtained from Dr. Andrew May (Oak Ridge National Laboratory) have a easy-plane anisotropy [46]. Even for a given group of crystals procured from the same source and synthesized under the same conditions, the magnetism cannot be described by



(a) Fe_3GeTe_2 **(b)** Fe_5GeTe_2

Figure 5.1: Monolayers of **a)** Fe_5GeTe_2 and **b)** Fe_3GeTe_2 viewed along the ***a*** axis.

a single universality class [130].

However, general observations which are consistent include T_C near room temperature, a smaller PMA than Fe_3GeTe_2 [22, 46] and the prevalence of stacking faults [46, 132]. While large-PMA magnets such as bulk Fe_3GeTe_2 and $CrGeTe_3$ can be described by the 2D Ising and the 2D-to-3D tricritical mean field models respectively, bulk magnetism in Fe_5GeTe_2 is closest to the 3D Heisenberg model, despite the existence of vdW gaps [130]. Due to the high-T_C magnetism which cannot be accounted for by magnetic anisotropy alone, it would be instructive to characterize the ferromagnetism in Fe_5GeTe_2 for the atomically thin limit. This chapter will discuss the XPEEM-based characterization of magnetic domains in few-layer Fe_5GeTe_2 and NVSM of field-induced domain motion in few-layer Fe_5GeTe_2.

5.2 Synthesis and preliminary characterization of few-layer Fe_5GeTe_2

Single crystals of Fe_5GeTe_2 were grown by Dr. Zhengxian Li and Prof. Yanfeng Guo at ShanghaiTech University with CVT [130]. Due to the large vdW cleavage energy in Fe_3GeTe_2 and Fe_5GeTe_2, it is extremely difficult and unlikely to obtain atomically thin flakes by standard mechanical exfoliation [8, 17, 35], highlighting the need for alternative synthesis techniques. Here, a gold-assisted exfoliation method [39] was used to exfoliate few-layer flakes (Chapter 2.2).

Due to the air-sensitivity of Fe_5GeTe_2, optical characterization (Chapter 2.3) is particularly useful because it is non-invasive and can be done inside of a glove-

box. However, calibration samples are required to first establish the necessary parameters. To address this, a calibration sample of Fe_5GeTe_2 was first exfoliated. Optical microscopy was used to confirm the presence of few-layer flakes with lateral dimensions of some tens of µm (Figure 5.2). AFM was used to measure the thicknesses of several flakes. The measured monolayer-to-bilayer step height of 0.66 nm is somewhat less than the nominal monolayer thickness of $c/3 = 0.8$ nm [46]. The exact lattice parameters can vary between crystals procured from different sources. Moreover, vdW gaps exist between each monolayer within one unit cell, meaning that the thickness of one exfoliated Fe_5GeTe_2 monolayer is bounded by an upper limit which is equal to $c/3$. Note that data obtained from previous AFM measurements of $CrSiTe_3$ (Figure 3.1) agree well with those found in the literature [69, 71].

The optical contrasts and thicknesses from different flakes were compared to each other to derive a linear relation between the optical contrast and the number of layers (Figure 5.2) [6]. For the XPEEM measurement, a new sample was made, as the calibration sample had been exposed to air during AFM measurements. The linear contrast-thickness relation described above was used to deduce that flakes up to 4 L in thickness were present within this new sample. Note that this was performed inside of the glovebox to avoid oxidation. The sample was then capped with a thin amorphous Se layer [22].

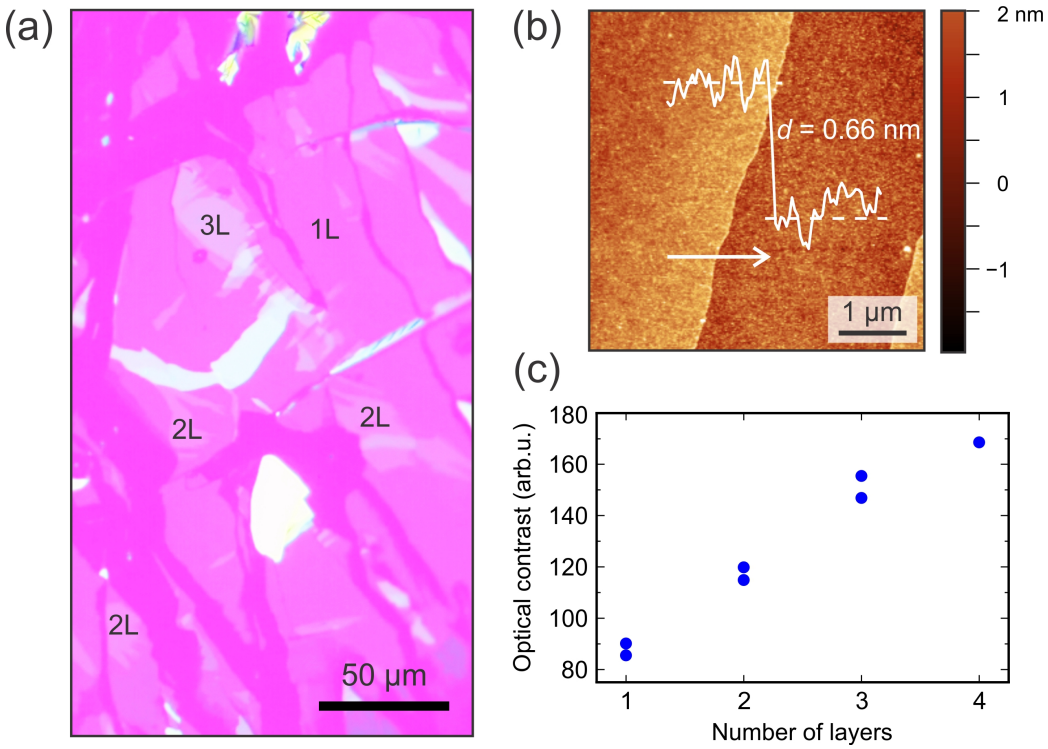


Figure 5.2: a) Optical micrograph of Fe_5GeTe_2 made with gold-assisted exfoliation. **b)** AFM scan of a monolayer-to-bilayer step. **c)** Optical contrast in **a)** measured as a function of the number of layers. The exfoliated samples were prepared by Ryuji Fujita. The bulk parent compound was synthesized by Dr. Zhengxian Li and Prof. Yanfeng Guo at ShanghaiTech University.

5.3 X-ray photoelectron emission microscopy characterization of Fe_5GeTe_2

5.3.1 Ferromagnetic domains in bulk Fe_5GeTe_2

The ferromagnetism in bulk Fe_5GeTe_2 is characterized by labyrinth-type domains (Figure 5.3a). These domains have a qualitative resemblance to labyrinth-type domains found in bulk Fe_3GeTe_2 (Figure 5.3b), which form because of intercompeting uniaxial anisotropy energy K_u and stray field energy K_d [8, 133]. The data shown in Figures 5.3a and 5.3b for bulk Fe_5GeTe_2 and Fe_3GeTe_2 were collected at 60 K and 50 K respectively.

However, the labyrinth domains found in bulk Fe_5GeTe_2 are much more narrow compared to those found bulk Fe_3GeTe_2. This may be because of the reduction of PMA in Fe_5GeTe_2 compared to Fe_3GeTe_2. In detail, the domain wall energy $\sigma_w \propto \sqrt{AK_u}$ and the domain wall width $W_d \propto \sqrt{A/K_u}$. For reduced K_u, it is less energetically costly for the magnetization to be broken up into narrow domains, and an increase in W_d should also follow.

On the other hand, the characterization of W_d is challenging. Qualitatively, the average W_d can be expected to be larger in Fe_5GeTe_2 than in Fe_3GeTe_2. However, the characterization of domain walls with XPEEM requires a magnetization vector map constructed from the XMCD contrasts obtained at different azimuths [33], which was not done here due to a limited amount of beamtime. Additionally, much higher magnifications are required to resolve domain walls. It should be noted that even at high magnifications, images of domain walls will be convoluted by the spatial resolution of XPEEM, which is around 30 nm. Therefore, any attempt to characterize W_d from Figures 5.3a or 5.3b alone would not be meaningful. Other techniques, such as NVSM, are more well-suited, and will be discussed in Section 5.4.

Alternatively, domain branching mechanisms may also be at play. It can be seen that compared to Fe_3GeTe_2 in which the stripe domains are mostly continuous and are parallel to each other (Figure 5.3b), there is a larger degree of domain branching in Fe_5GeTe_2 (Figure 5.3a). Generally, domain branching occurs when it is energetically preferable to reduce K_d by increasing the number of domains near the surface at the expense of $\sigma_w \propto \sqrt{AK_u}$ [21]. It is useful to consider two cases, which include closure domains and two-phase domain branching.

Closure domains occur when the easy axis is not parallel to the surface of a material. This is sometimes referred to as a misoriented surface. To minimize K_d near the surface, closure domains form. This is best visualized with the Landau model for uniaxial material [134]. Here, we consider an infinite plate which has uniaxial anisotropy K_u. $W_d \propto \sqrt{A/K_u}$ is small compared to the plate thickness D. Furthermore, K_u is small compared to K_d. Under these conditions, the formation of IP closure domains at the surface reduces the energy density compared

to a domain structure with only up and down magnetization directions. For materials with larger anisotropy where K_u is similar or larger than K_d, the closure domains consist of a large OOP component and a small IP component [21].

Two-phase domain branching occurs for strongly misoriented surfaces, in which bulk domains branch off into finer domains at the surface to minimize K_d at the expense of σ_w. However, the key difference between closure domains and two-phase domain branching is that in two-phase domain branching, the fine domain patterns at the surface consist of OOP domains which do not include any IP component. In contrast to closure domains, two-phase domain branching occurs in strongly uniaxial materials for which $K_u \gg K_d$ [21].

In bulk Fe_5GeTe_2, the observed domains resemble prototypical labyrinth domains, indicating large K_u. There is no obvious evidence for IP closure domains, which should show up as an intermediate contrast in the XPEEM image [135]. Two-phase domain branching is a more likely explanation for the finer domain features in Fe_5GeTe_2. In Fe_3GeTe_2, a larger K_u would dominate K_d, meaning that refinement of the surface domain structure would not be as favorable and that the domain structure is homogeneous along $\boldsymbol{c}$. This should also be the case for atomically thin flakes of Fe_5GeTe_2, as the atomic thicknesses are much less than typical W_d of some tens of nm [136].

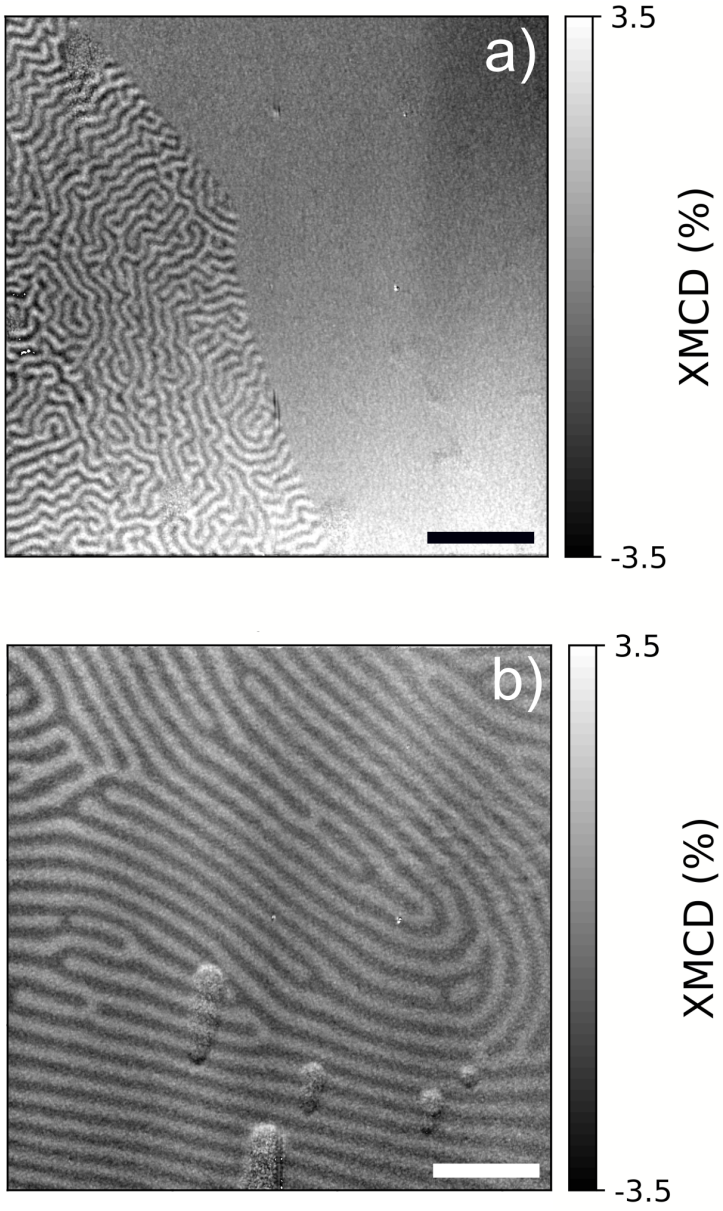


Figure 5.3: a) XMCD image of bulk Fe_5GeTe_2 obtained at 50 K. The labyrinth domains indicate a large uniaxial anisotropy, although a high density of domain walls suggest smaller σ_w and K_u compared to Fe_3GeTe_2. Scale bar = 2 µm. **b)** XMCD image of bulk Fe_3GeTe_2 obtained at 50 K, showing a labyrinth domain structure indicating a large uniaxial anisotropy. Scale bar = 2 µm. Bulk single crystals were synthesized by Dr. Zhengxian Li and Prof. Yanfeng Guo at ShanghaiTech University.

5.3.2 Ferromagnetic domains in atomically thin Fe_5GeTe_2

The ferromagnetic domain structure of atomically thin flakes differ greatly from that of the bulk. Before this is discussed in further detail, it is worth pointing out some general, yet important aspects of the XAS and XMCD data of 4 L and 3 L Fe_5GeTe_2 flakes presented in Figure 5.4.

Firstly, the role and contribution of non-magnetic defects will be discussed in detail. XAS data is sensitive to the chemical composition as well as the surface topography for a given sample. For the atomically thin 4 L and 3 L flakes of Fe_5GeTe_2, the XAS data show small pockets which have lower photoemission yield from the Fe L_3 edge compared to other regions (Figure 5.4a). This has no apparent effect on the XMCD image, where magnetic domains are visible across the entire sample and are continuous across these pockets. Therefore, changes in surface topography, such as holes, and local charging may be ruled out. Furthermore, any change in the chemical environment, such as Fe deficiencies (Section 5.5), which have significant effects on the magnetic properties, may also be excluded. One possibility is locally thick Se capping, as this would simply offset the intensity of the XAS, given by the sum of the intensities obtained with LCP and RCP, without changing the XMCD, which is given by the difference.

Second, compared to the bulk magnetic labyrinth domain structure in which the domains are either pointing up or down, the magnetization of 3 L and 4 L Fe_5GeTe_2 varies considerably (Figure 5.4). Some parts of the flake have larger XMCD than other regions (Figure 5.4b). As discussed above, the XAS data (Figure 5.4a) do not support any signs of spatially varying chemical composition or surface topography, other than the pockets with low intensity which have no correlation with the XMCD (Figure 5.4b). Therefore, the spatial variation of the XMCD is likely to be of magnetic origin. One possibility is that the magnetization varies across the flake due to defects, such as stacking disorder or Fe vacancies, as explained in Section 5.1. Alternatively, these regions may have a finite IP magnetization component. For the situation where this IP component is isotropic and can point in any direction, the XMCD would appear be large in some regions, and small in others, because the XMCD is proportional to $\vec{m} \cdot \vec{k}$.

However, as noted previously, the characterization of magnetization directions is not possible with one single XMCD image alone, and requires at least two images which are taken at azimuths of 0° and 90°. This will be revisited further below (Section 5.6) and in Chapter 6.

Third, the XMCD intensity from 3 L Fe_5GeTe_2 is generally smaller than the XMCD intensity from 4 L. This is most obvious in Figure 5.6a. As discussed above, the XAS image shows there are no topographical features or changes in the chemical profile between 3 L and 4 L Fe_5GeTe_2. In principle, the reduced XMCD in 3 L may be due to low photoelectron emission because of reduced scattering volume in the atomically thin limit. Photoelectrons emitted in XPEEM have an information depth of 5-10 nm [137]. Therefore, less photoelectrons will be emitted per unit volume for samples which are just a few atoms thick, compared to a bulk single crystal. However, there is no change in the XAS intensity between 3 L and 4 L Fe_5GeTe_2 (Figure 5.6a), so the reduced XMCD does not originate from layer-dependent photoelectron emission.

The reduced XMCD in 3 L Fe_5GeTe_2 must therefore be of magnetic origin; somehow, the magnetic moment in 3 L is smaller than that of 4 L. NVSM is used to confirm the reduction of magnetic stray fields for 2 L compared to 3 L, which means that the magnetization in 2 L is less than in 3 L (Section 5.4). This is at least partially due to layer-by-layer dependence of T_C for atomically thin magnets, which is a consequence of the Mermin-Wagner theorem (Chapter 1.4).

In the following, the magnetic domain structures in 3 L and 4 L Fe_5GeTe_2 will be characterized in terms of K_u, K_d, and the presence of magnetic bubble domains. Here, it is useful to begin by comparing the domain structure in 3 L and 4 L Fe_5GeTe_2 to the domain structure of atomically thin Fe_3GeTe_2, which has a single domain state in the atomically thin limit due to extremely large K_u [8, 133]; the formation of any domains would be energetically costly in this case.

We begin by analyzing the 4 L magnetic domain structure presented in Figure 5.4b. In contrast to the homogeneous magnetization found in atomically thin Fe_3GeTe_2 [8], there are small domains in 4 L Fe_5GeTe_2. The domain structure qualitatively resembles a partially, but not fully demagnetized easy-axis ferro-

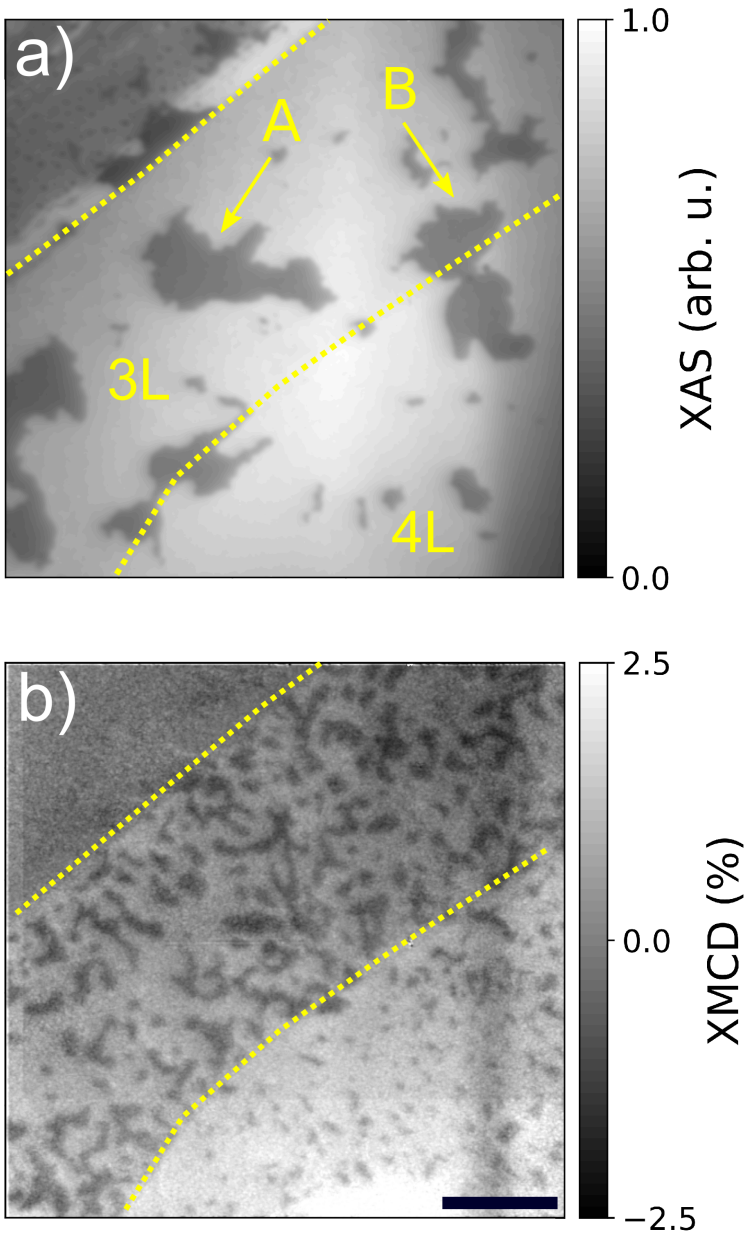


Figure 5.4: a) XAS image of 3 L and 4 L Fe_5GeTe_2. Areas with locally reduced Fe L_3 signal are denoted as A and B. These areas most likely come from inhomogeneities of the Se capping layer. **b)** XMCD image of 3 L and 4 L Fe_5GeTe_2 obtained at 50 K. The 3 L domain structure shows increased competition between K_u and K_d. Scale bar = 2 µm. Bulk single crystals were synthesized by Dr. Zhengxian Li and Prof. Yanfeng Guo at ShanghaiTech University.

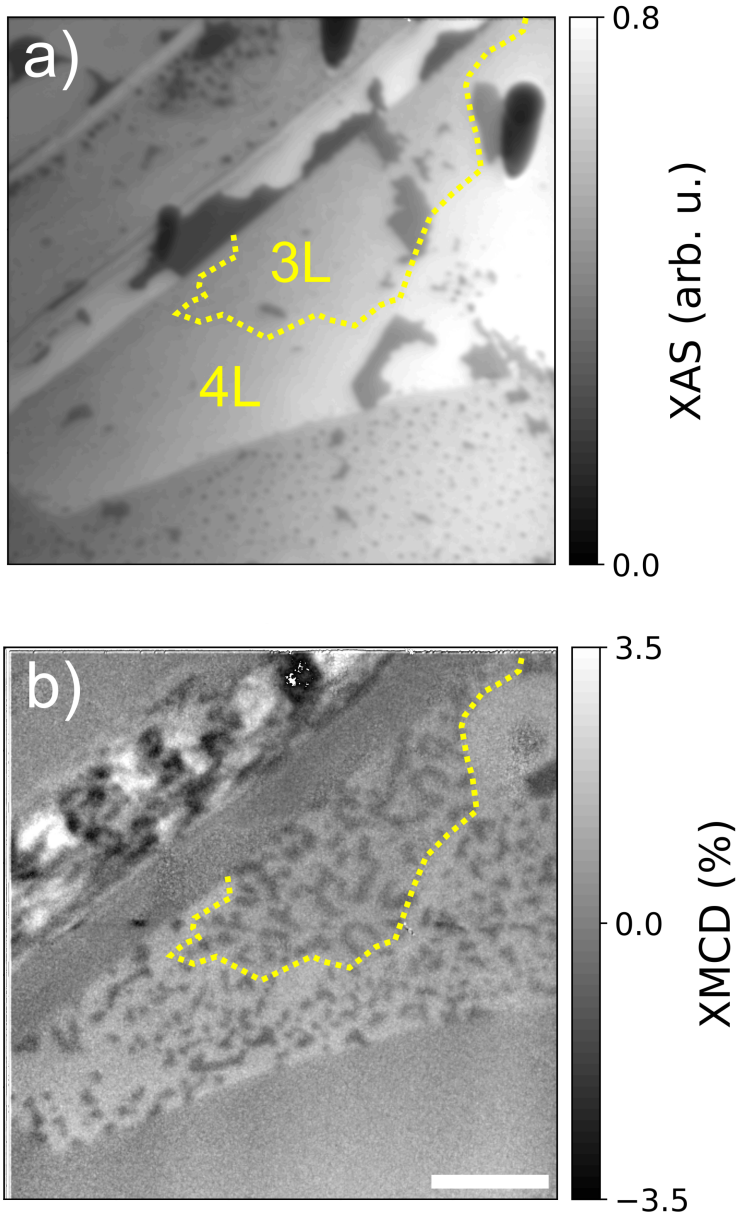


Figure 5.5: a) XAS of 3 L and 4 L Fe_5GeTe_2. Dark areas with reduced photoemission yield from Fe L_3 edges are present. These areas are also present in Figure 5.4a, and have no correlation with the XMCD. **b)** XMCD of 3 L and 4 L Fe_5GeTe_2 obtained at 50 K. In 4 L regions, bubble domains are found. In 3 L regions, a mixed distribution of stripe domains and bubble domains form. The magnetic domains abruptly stop at the 3 L-4 L boundary. Scale bar = 2 µm. Bulk single crystals were synthesized by Dr. Zhengxian Li and Prof. Yanfeng Guo at ShanghaiTech University.

magnet, which would have an even distribution of up and down domains. In a binary approximation, 88% of the magnetization points up, while the remaining 12% of the magnetization points down. Moreover, the minority domains are characterized by magnetic bubbles with diameters of $300 - 500$ nm. These bubbles are distinct from those which nucleate from band domains upon application of an OOP field, as no field was applied during the experiment [21].

The existence of these minority bubble domains constitutes evidence of competition between K_u and K_d. This is unusual for 2D vdW magnets, which usually have a very large K_u in the atomically thin limit [6–8, 17]. However, K_u is still large, preventing the formation of stripe domains as seen for bulk Fe_5GeTe_2, which would further reduce K_d at the cost of σ_w. The domain structures of 3 L and 2 L Fe_5GeTe_2 will now be analyzed in terms of K_u and K_d, and their relative contributions.

For 3 L, the magnetization further breaks up into more domains (Figure 5.4b), which is in contrast to atomically thin Fe_3GeTe_2 and other large-PMA 2D magnets [6, 7]. In a binary approximation, 52% of the magnetization points up, and 48% of the magnetization points down, meaning that the domain structure now resembles an almost fully demagnetized easy-axis ferromagnet. In 3 L Fe_5GeTe_2, it seems that K_u and K_d compete with each other on an even basis, meaning that it is more energetically preferable to reduce K_d by forming larger bubble domains and stripe domains at the expense of σ_w and K_u. Bubble domains with diameters ranging from $500 - 600$ nm coexist with stripe-like domains. Moreover, it seems like the stripe domains consist of interconnected bubble domains, again pointing to the competition between K_u, which would encourage the smaller bubble domains to congregate into larger stripe domains, and K_d, which generally promotes the separation of larger domains into smaller domains to minimize the stray field.

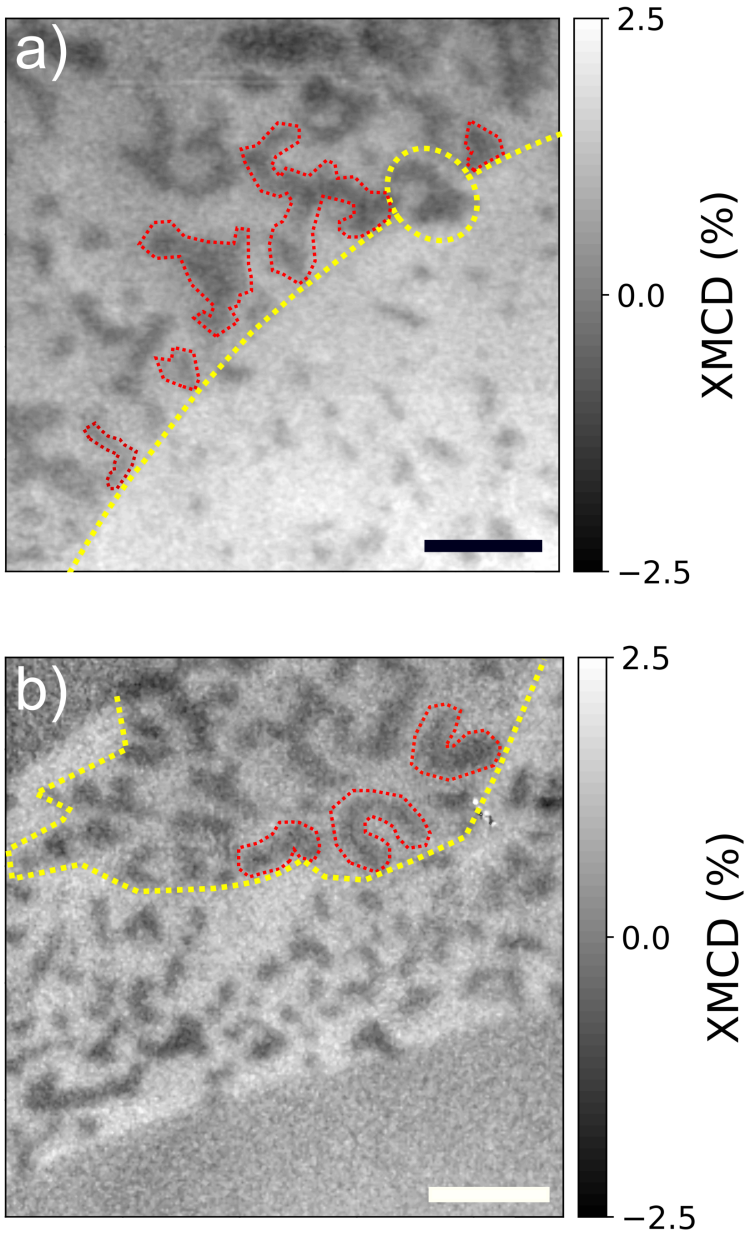


Figure 5.6: a) Ferromagnetic domains at the 3 L-4 L boundary in Figure 5.4b. Nearly all domains (outlined by red dashed lines), except for one sole exception (circled by yellow dashed line), do not cross the 3 L-4 L boundary. **b)** Ferromagnetic domains at the 3 L-4 L boundary in Figure 5.5b. The 3 L XMCD intensity is less than that of 4 L, indicating a reduced magnetization in 3 L. Here, all domains (outlined by red dashed lines) abruptly stop at the 3 L-4 L boundary. These data were obtained at 50 K. Scale bars = 1 µm.

An analysis of the domain structure at the 3 L-4 L boundary also gives insights into the layer-dependent energy terms. The 3 L-4 L boundary is characterized by the abrupt discontinuity of magnetic domains (Figures 5.5 and 5.6), with the exception of one single domain (circled by yellow dashed line), which crosses the boundary (Figure 5.6a). This domain may be pinned to an intrinsic defect in the Fe_5GeTe_2 or a defect resulting from the interaction with the substrate. In Figure 5.6b, all domains abruptly stop at the 3 L-4 L boundary.

The discontinuity of magnetic domains at the 3 L-4 L boundary can be understood as a result of the sudden change in the layer-dependent domain wall energy $\sigma_{\mathrm{W}}^{i} = \sqrt{AK_{\mathrm{u}}^{i}}$ at the 3 L-4 L boundary, where K_{u}^{i} is the layer-dependent magnetic anisotropy for the i^{th} layer. The discontinuity in σ_{W}^{i} results in strongly pinned domains and domain walls at the 3 L-4 L boundary [138].

In 2 L Fe_5GeTe_2, the magnetization continues to break up into domains to an arguably greater extent than 3 L or 4 L (Figure 5.7). In contrast to the 3 L and 4 L flakes, the relatively low photoelectron yield, which can be seen from the XAS image, in combination with the reduced magnetization, contributes to reduced XMCD. Nevertheless, magnetic domains are unambiguously present. Similarly to 3 L, the domain structure resembles that of a fully demagnetized easy-axis ferromagnet. In a binary approximation, 53% of the magnetization points up, while the remaining 47% of the magnetization points down. Here, no magnetic bubbles can be discerned, which could be due to a further reduction of the easy-axis anisotropy, which is required to stabilize bubble domains [21].

The topological nature of the observed magnetic bubbles in Figures 5.4 and 5.5 needs to be addressed. Skyrmions and merons, which are magnetic objects with non-trivial topology, have been observed in bulk Fe_3GeTe_2 [23] and Fe_5GeTe_2 [20]. However, no topological spin textures have been observed in atomically thin magnets to date, and the observation of these objects in few-layer 2D materials would be seminal. First, more conventional magnetic bubble domains, including those formed by domain wall pinning, will be discussed in the following section.

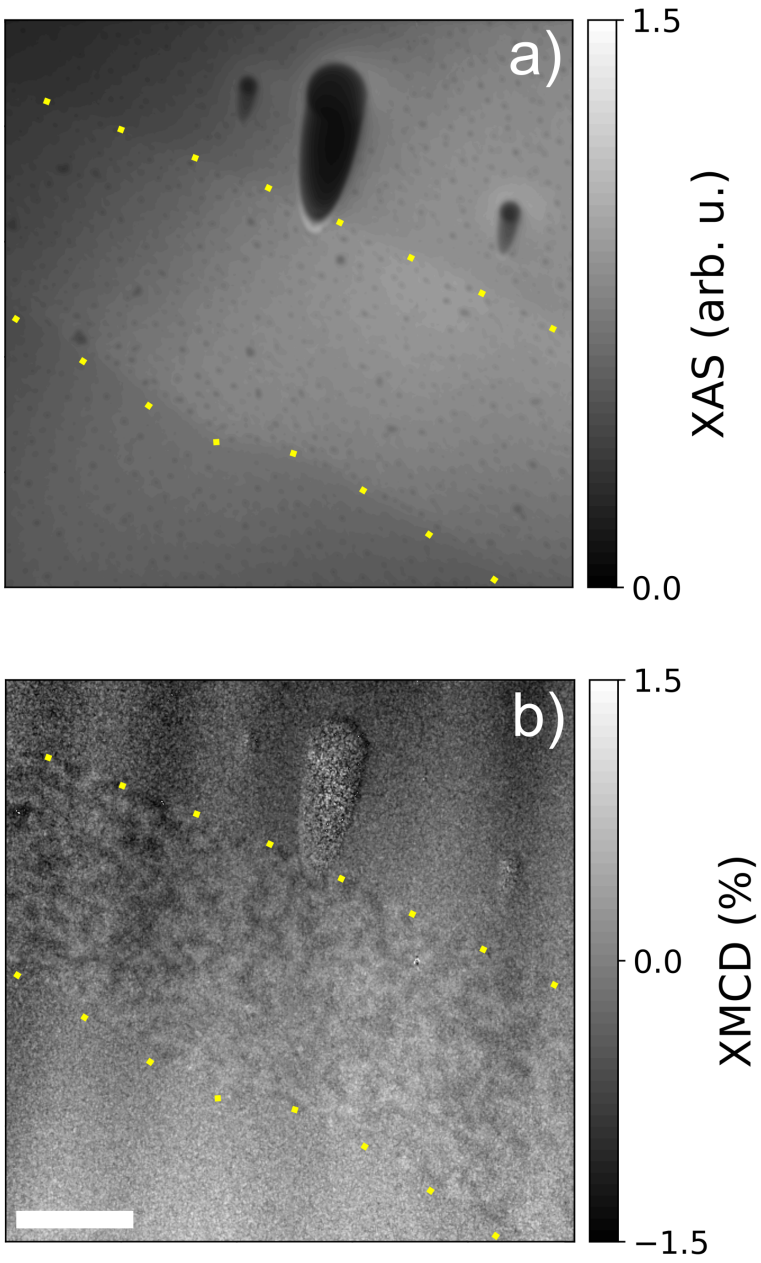


Figure 5.7: a) XAS of 2 L Fe_5GeTe_2 (outlined by yellow dashed line). Photoemission yield is reduced compared to 3 L or 4 L Fe_5GeTe_2. **b)** XMCD of 2 L Fe_5GeTe_2 obtained at 50 K. Despite the reduced photoemission yield, ferromagnetic domains are nevertheless present. Bulk crystals were synthesized by Dr. Zhengxian Li and Prof. Yanfeng Guo at ShanghaiTech University. Scale bar = 2 µm.

5.4 Nitrogen-vacancy center scanning magnetometry study of domain pinning in few-layer Fe_5GeTe_2

The characterization of topological spin textures requires the measurement of their chiral property. The high sensitivity of NVSM makes it the ideal tool to determine if the magnetic bubbles observed in Section 5.3.2 have an associated chiral property. NVSM data were obtained and analyzed by Dr. Michael Högen, Dr. Anthony K.C. Tan, and Prof. Mete Atatüre at the Cambridge Nanoscale Sensing and Imaging Suite (CANSIS) at the University of Cambridge [30].

The presence of magnetic domains was confirmed with NVSM on a freshly prepared sample of atomically thin flakes of Fe_5GeTe_2 (Figure 5.8). The parent bulk crystal was synthesized by Dr. Zhengxian Li and Prof. Yanfeng Guo at ShanghaiTech University. The domain structure measured with NVSM bares a qualitative resemblance to the domain structure of 4 L, 3 L and 2 L Fe_5GeTe_2 characterized by XPEEM (Section 5.3.2), for which stripe and bubble domains form.

Reduction of the magnetic moment per unit area is confirmed by reduced stray fields emerging from the saturated state (Figure 5.9). For 3 L and 2 L Fe_5GeTe_2, $\widetilde{M}_{sat}$ is estimated to be (67 ± 2.5) μ_B/nm^2 and (37 ± 1.3) μ_B/nm^2, respectively, corroborating the reduced XMCD observed in 2 L Fe_5GeTe_2 (Section 5.3.2). For comparison, $\widetilde{M}_{sat}$ of bulk Fe_3GeTe_2 at similar temperatures is estimated to be approximately 80 μ_B/nm^2 [106].

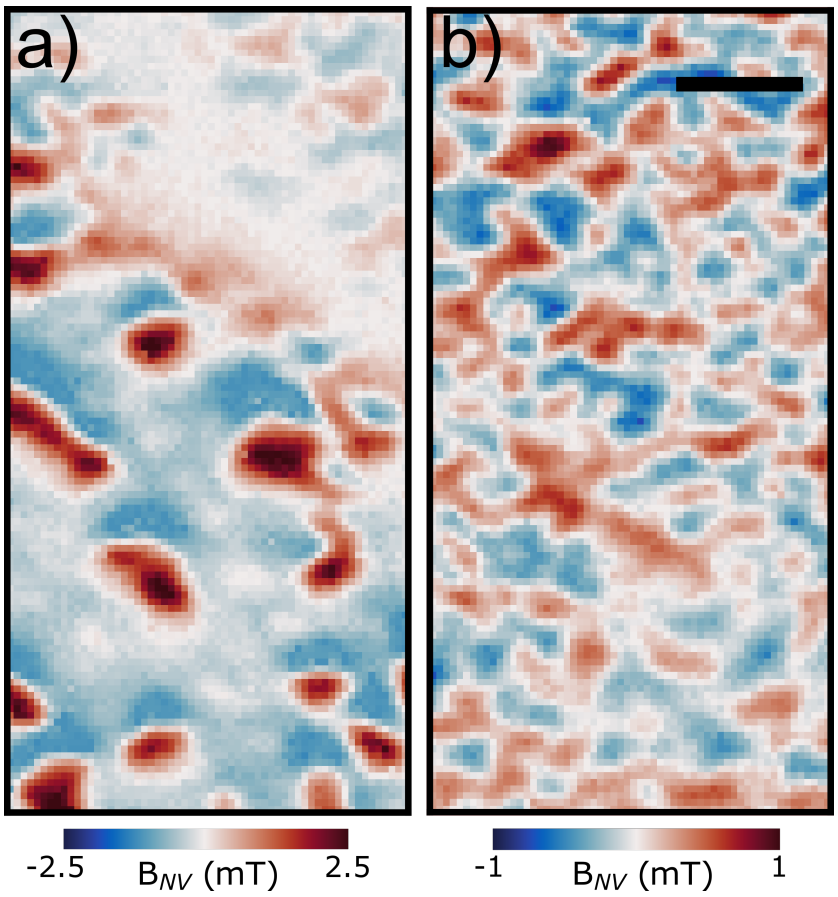


Figure 5.8: Stray fields from **a)** 3 L and **b)** 2 L Fe_5GeTe_2 measured at 4 K. The bulk crystals were synthesized by Dr. Zhengxian Li and Prof. Yanfeng Guo at ShanghaiTech University. The NVSM measurements were performed by Dr. Michael Högen, Dr. Anthony K.C. Tan and Prof. Mete Atatüre at the University of Cambridge. The figure is the courtesy of Dr. Högen, Dr. Tan and Prof. Atatüre at the University of Cambridge. Scale bar = 500 nm.

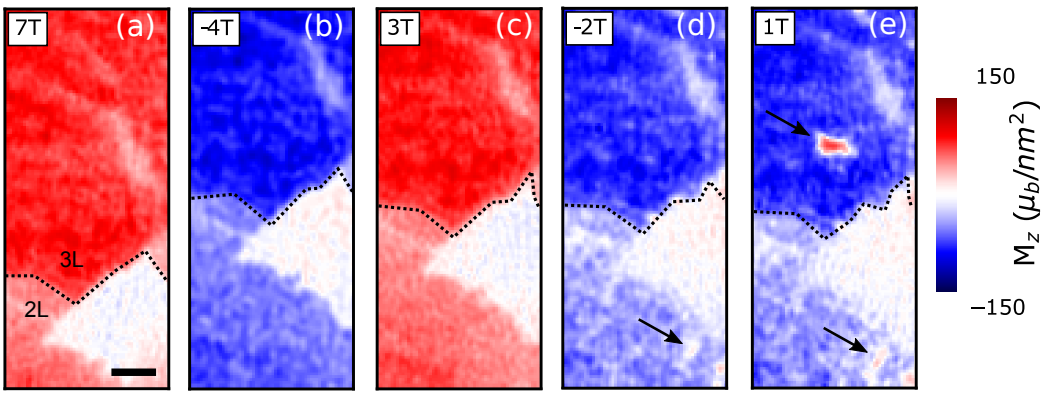


Figure 5.9: Demagnetization of 3 L and 2 L Fe_5GeTe_2. **a-e)** Fields of decreasing magnitude and alternating polarity were applied to demagnetize the sample. Domain nucleation, indicated by black arrows, occur at approximately -2 T and 1 T for 2 L and 3 L Fe_5GeTe_2, respectively. The stray field maps were acquired at 4 K. Scale bar = 500 nm. The NVSM measurements were performed by Dr. Michael Högen, Dr. Anthony K.C. Tan, and Prof. Mete Atatüre at the University of Cambridge. The exfoliated samples were synthesized by Ryuji Fujita. The bulk crystals were synthesized by Dr. Zhengxian Li and Prof. Yanfeng Guo at ShanghaiTech University. The figure is the courtesy of Dr. Högen, Dr. Tan and Prof. Atatüre at the University of Cambridge.

Furthermore, H_{sat} is estimated to be greater than 2 T for 2 L and 1 T for 3 L. This is inferred from Figure 5.9, in which a demagnetization sequence was applied to determine the layer-dependent H_{sat}. Domain nucleation is observed at -2 T for 2 L and 1 T for 3 L, indicating that magnetic saturation occurs at larger fields. This is illustrated by Figure 5.10, in which the layer-dependent hysteresis was estimated. For 2 L and 3 L Fe_5GeTe_2, H_{sat} is rather large and is comparable to H_{sat} found in atomically thin Fe_3GeTe_2 [8].

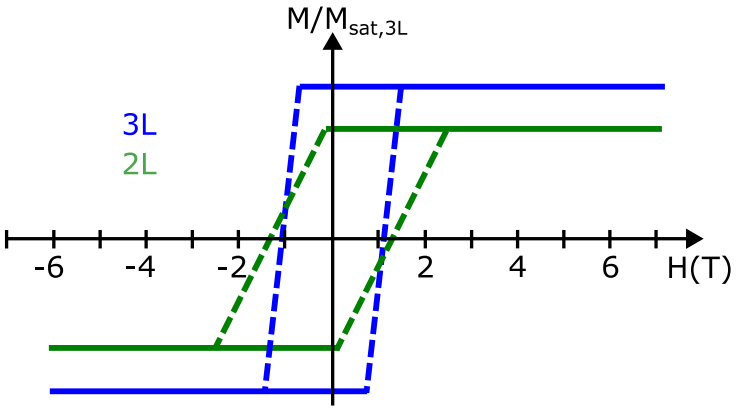


Figure 5.10: Estimated magnetic hysteresis for 3 L and 2 L Fe_5GeTe_2 at 4 K. The saturation fields were estimated from Figure 5.9. The figure is the courtesy of Dr. Michael Högen, Dr. Anthony K.C. Tan and Prof. Mete Atatüre at the University of Cambridge.

A vdW magnet can be idealized as a defect-free, atomically thin single-crystalline sheet isolated in vacuum (Figure 5.1a). Hence, domain wall motion under such ideal conditions should be unimpeded by domain wall pinning. The attainment of such ideal conditions in actual experiments is challenging, and Fe_5GeTe_2 is characterized by a large density of intrinsic defects such as stacking disorders (Section 5.1) and Fe vacancies (Section 5.6). The most direct and straightforward method of characterizing the prevalence of pinning centers and their role in the magnetic hysteresis is to measure the field dependence of the domains with NVSM.

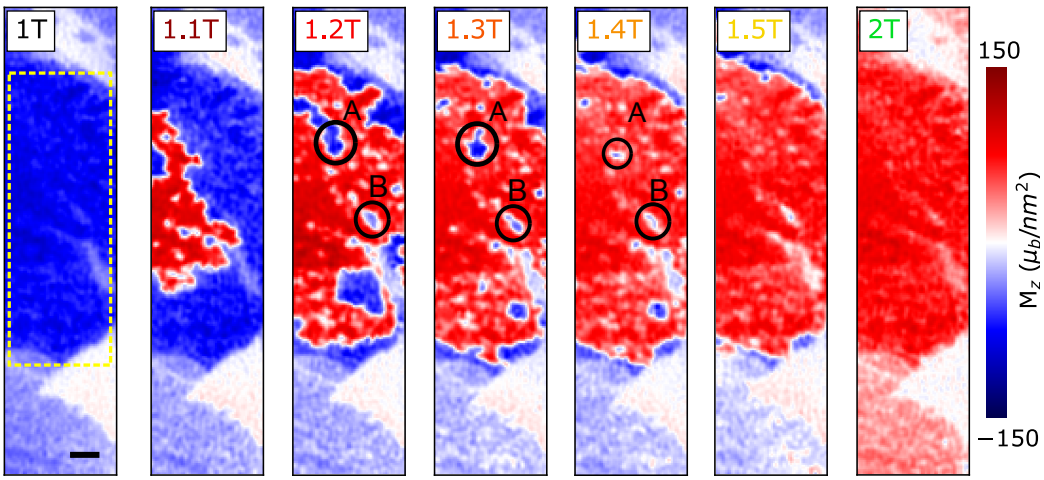


Figure 5.11: Field-dependent magnetization of 3 L Fe_5GeTe_2. Representative pinning centers are denoted as 'A' and 'B'. The stray field data were acquired at 4 K. The NVSM measurements were performed by Dr. Michael Högen, Dr. Anthony K.C. Tan, and Prof. Mete Atatüre at the University of Cambridge. The exfoliated samples were synthesized by Ryuji Fujita. The bulk crystals were synthesized by Dr. Zhengxian Li and Prof. Yanfeng Guo at ShanghaiTech University. The figure is the courtesy of Dr. Högen, Dr. Tan and Prof. Atatüre at the University of Cambridge. Scale bar = 500 nm.

Field-dependent magnetization data from 3 L Fe_5GeTe_2 is presented in Figure 5.11. In detail, the sample was first saturated in an OOP field $H_{OOP} = -3$ T before target fields, $H_{applied}$, ranging from 1-2 T was applied. After applying $H_{applied}$, the stray fields from the sample were measured at remanence.

The magnetization of 3 L Fe_5GeTe_2 begins to switch upon application of $H_{applied} =$ 1.1 T. Application of larger fields ranging from 1.1-1.4 T show multiple pinning centers, which remain at fixed positions. Two representative pinning centers, denoted as 'A' and 'B', are indicated in Figure 5.11. A relatively large field of 1.5 T is required to switch the magnetization at pinning centers A and B. Magnetic hysteresis data, which was derived by plotting M_z in the yellow dashed rectangle in Figure 5.11 as a function of the different fields, show a wasp-tail contribution to the magnetic hysteresis at fields larger than 1.5 T, which are due to 'A', 'B', and other pinning centers (Figure 5.12).

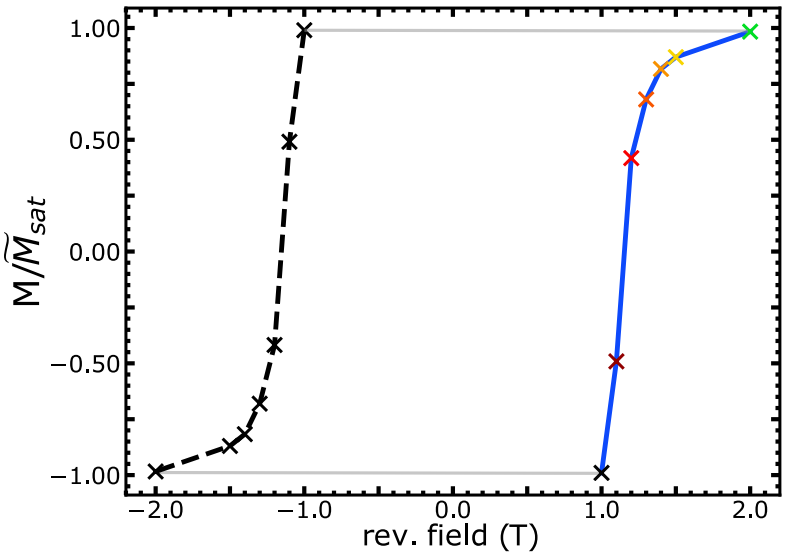


Figure 5.12: Field-dependent magnetic hysteresis of 3 L Fe_5GeTe_2 obtained at 4 K. The magnetization M, which is calculated from the region outlined in the yellow rectangle in Figure 5.11, is normalized to the saturation magnetization $\widetilde{M}_{sat}$. Pinning sites contribute to an enhancement of H_{sat} from approximately 1.2 to 2 T. The figure is the courtesy of Dr. Michael Högen, Dr. Anthony K.C. Tan and Prof. Mete Atatüre at the University of Cambridge.

The non-negligible contribution of defects and pinning centers suggests that at least some of the magnetic bubbles observed in the XPEEM data (Figures 5.4 and 5.6) could be pinning centers.

The topological properties of magnetic bubble domains can be determined by analyzing the magnetic domain walls. In detail, thin films with sizable PMA have domain walls which are Bloch-type for the presence of little to no Dzyaloshinskii-Moriya interaction (DMI), while domain walls which are Néel-type are found in thin films with large DMI, often resulting from broken inversion symmetry [139]. Figure 5.13 shows Bloch-type domain walls, for which the divergence of the IP magnetization component $\nabla \cdot \vec{M}_{xy} = 0$, thus limiting the stray field emanating from Bloch-type domain walls.

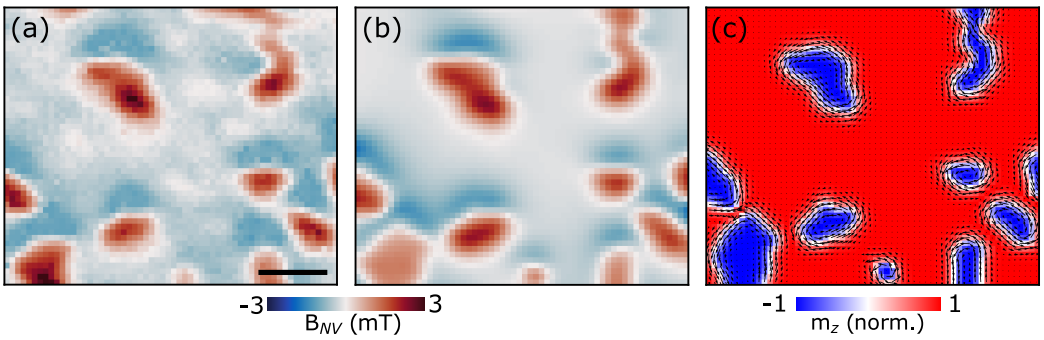


Figure 5.13: Simulation of bubble domains in 3 L Fe_5GeTe_2 observed at 4 K. **a)** A spatial map of the stray field, B_{NV}, shows bubble domains after cooling in zero field. **b)** A simulated stray field, for which the domain walls are Bloch-type, matches the experimental data shown in **a)**. **c)** The magnetization corresponding to the stimulated stray field map in **b)** is shown. The figure is the courtesy of Dr. Michael Högen, Dr. Anthony K.C. Tan and Prof. Mete Atatüre at the University of Cambridge.

The simulated stray fields from Bloch-type domain walls closely resemble the experimental data. On the other hand, Néel-type domain walls, for which $\nabla \cdot \vec{M}_{xy} \neq 0$, are not representative of the experimental data. These data further support that the observed bubbles in atomically thin Fe_5GeTe_2 result from domain wall pinning, rather than a chiral DMI [140, 141].

Here, W_d is estimated by extracting line profiles across multiple domains. For 3 L, the average of W_d is approximately 135 nm (Figure 5.14), which is two orders of magnitude greater than the flake thickness, suggesting the domains are homogeneous along *c*. This is in contrast to thicker Fe_3GeTe_2 samples in which the surface oxide contributes to a surface DMI and skyrmions [142]. Additionally, W_d of 3 L Fe_5GeTe_2 is broad compared to that of Fe_3GeTe_2, for which W_d spans only some tens of nm [136]. This could be due to the smaller PMA in Fe_5GeTe_2 compared to Fe_3GeTe_2.

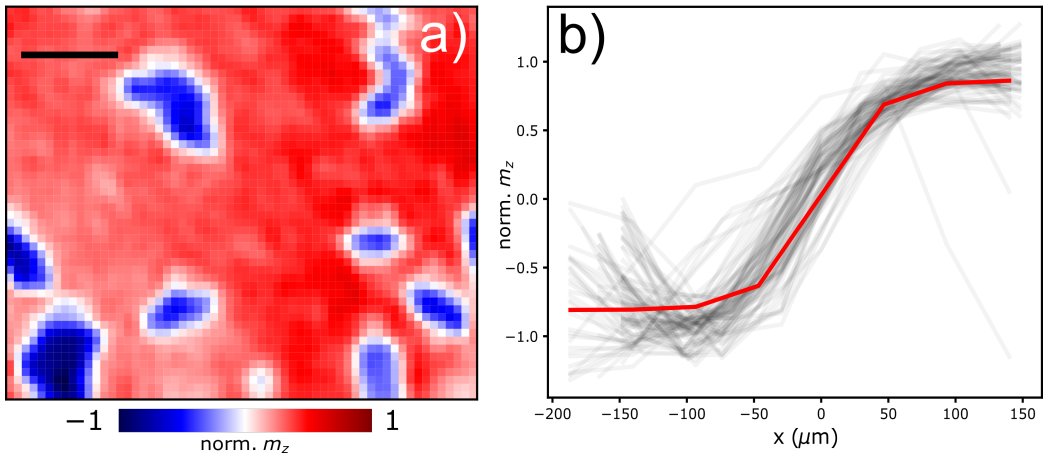


Figure 5.14: Estimation of W_d in 3 L Fe_5GeTe_2. **a)** Normalized OOP component of magnetization m_z calculated from 3 L stray fields. Scale bar = 500 nm. **b)** Extracted line profiles across multiple domains found in **a)**. The average of W_d is estimated by fitting the line profiles with the fit in red. An exemplary line profile is shown in yellow in **a)**. The figure is the courtesy of Dr. Michael Högen, Dr. Anthony K.C. Tan and Prof. Mete Atatüre at the University of Cambridge.

These NVSM data suggest that the observed magnetic bubbles are not skyrmions resulting from a chiral DMI. Rather, some of the bubbles could be pinning centers due to the presence pinning sites and defects, including Fe vacancies and excesses, which will be discussed in more detail in the next section.

5.5 Defects and magnetism in atomically thin Fe_5GeTe_2

As mentioned in Section 5.1 and in the previous section, Fe_5GeTe_2 is characterized by a large density of defects, including stacking disorder and variations in the Fe concentration. The latter has a direct and measurable effect on the ferromagnetism, which will be extensively discussed in this section.

A bulk Fe_5GeTe_2 crystal provided by Dr. Zhengxian Li and Prof. Yanfeng Guo (ShanghaiTech University) was freshly exfoliated into atomically thin flakes. AFM measurements taken after the XPEEM measurements confirm that 4-6 L

Fe_5GeTe_2 is present within the sample. Apart from some localized wrinkle-like features, the sample is free from significant variations in the surface topography, meaning that any changes in ferromagnetism for a given layer thickness must originate from variations in the chemical composition or lattice.

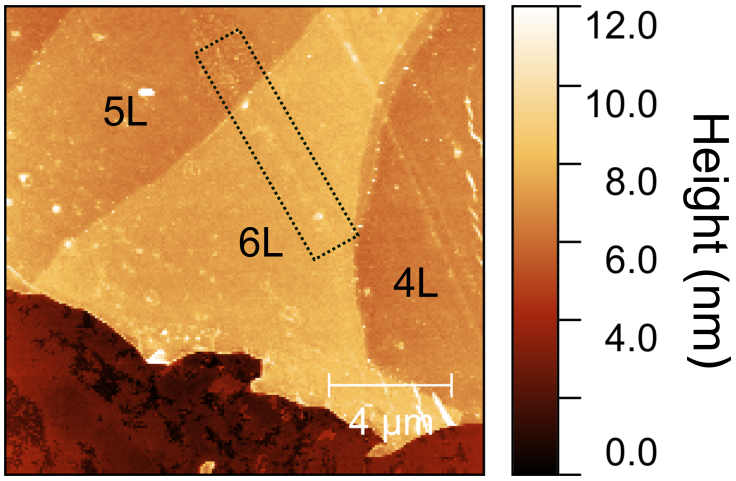


Figure 5.15: AFM of 4 L-6 L Fe_5GeTe_2, which show homogeneous and well-defined thickness for a given number of layers. A localized wrinkle-like feature is indicated by the black dashed line.

Indeed, variations in the Fe content are revealed by the XAS data; an Fe-deficient region (bounded by the blue triangles) is present (Figure 5.16). This Fe-deficient region also has straight edges, giving the impression that this specific region is a metastable phase of Fe_nGeTe_2, where n = 3, 4 or 5 [129]. It is difficult to infer the exact change in the lattice in this Fe-deficient area based on XPEEM alone. Nevertheless, some general estimations can be made.

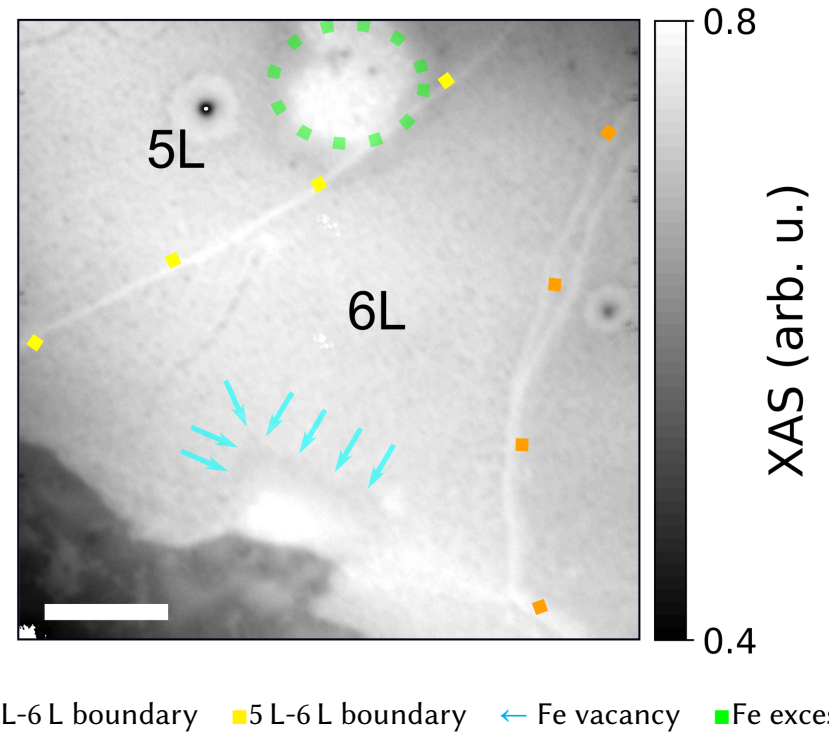


Figure 5.16: XAS of Fe_5GeTe_2. A region which is Fe-deficient is indicated by the cyan arrows. A region which has an excess amount of Fe is bounded by the dashed green line. 4 L-6 L and 5 L-6 L boundaries are indicated by the yellow and orange dots, respectively. The XPEEM measurement was performed by Dr. Mohamad A. Mawass and Dr. Florian Kronast at UE49-PGMa at BESSY II. The measurement temperature was 50 K. Scale bar = 2 µm.

Firstly, it can be seen that the Fe-deficient region has an enhanced XMCD (Figure 5.17). This applies for both the OOP (Figure 5.17a) and IP magnetization components (Figure 5.17b), meaning that the magnetization of the Fe-deficient region is enhanced, rather than an IP canting resulting in a larger XMCD signal. This is especially obvious for the IP magnetization component, as can be seen by the greater contrast in the IP XMCD image (Figure 5.17b). This behavior is counter-intuitive; one would expect a reduction of the magnetic moment for materials with smaller concentrations of magnetic transition metal ions. Therefore, the metastable Fe_3GeTe_2 phase can be excluded, as this large-PMA material [8] would have no IP magnetization in the atomically thin limit, and would also

likely have a smaller magnetic moment than Fe_5GeTe_2 [106].

In general, the deterministic synthesis of Fe_3GeTe_2 and Fe_5GeTe_2 with particular compositions is extremely challenging. Instead, the structural and magnetic properties of Fe_3GeTe_2 and Fe_5GeTe_2 which have been doped with transition metals including Co and Ni can be referenced. For $Fe_{3-x-1.5}Co_{1.5}GeTe_2$, the unit cell is smaller compared to undoped Fe_3GeTe_2. Rietveld refinement of the X-ray diffraction data shows that the lattice parameter a changes from 4.01293(8) to 3.92613(7) Å, while c changes from 16.3427(4) to 16.2227(4) Å. Correspondingly, T_C decreases from 225 K to 70 K upon the Co substitution [92].

For $Fe_{5-x-y}Ni_yGeTe_2$, the saturation magnetization changes from 1.80 μ_B to a maximum of 2.11 μ_B in $Fe_{4.11}Ni_{0.50}GeTe_2$ [132]. Rietveld refinement of X-ray diffraction data shows that the increase in saturation magnetization corresponds to shrinkage of the c-axis, while T_C is relatively constant. Therefore, the enhancement of the magnetic moment upon a slight Fe vacancy in Fe_5GeTe_2 is not necessarily inconsistent with previous findings [132].

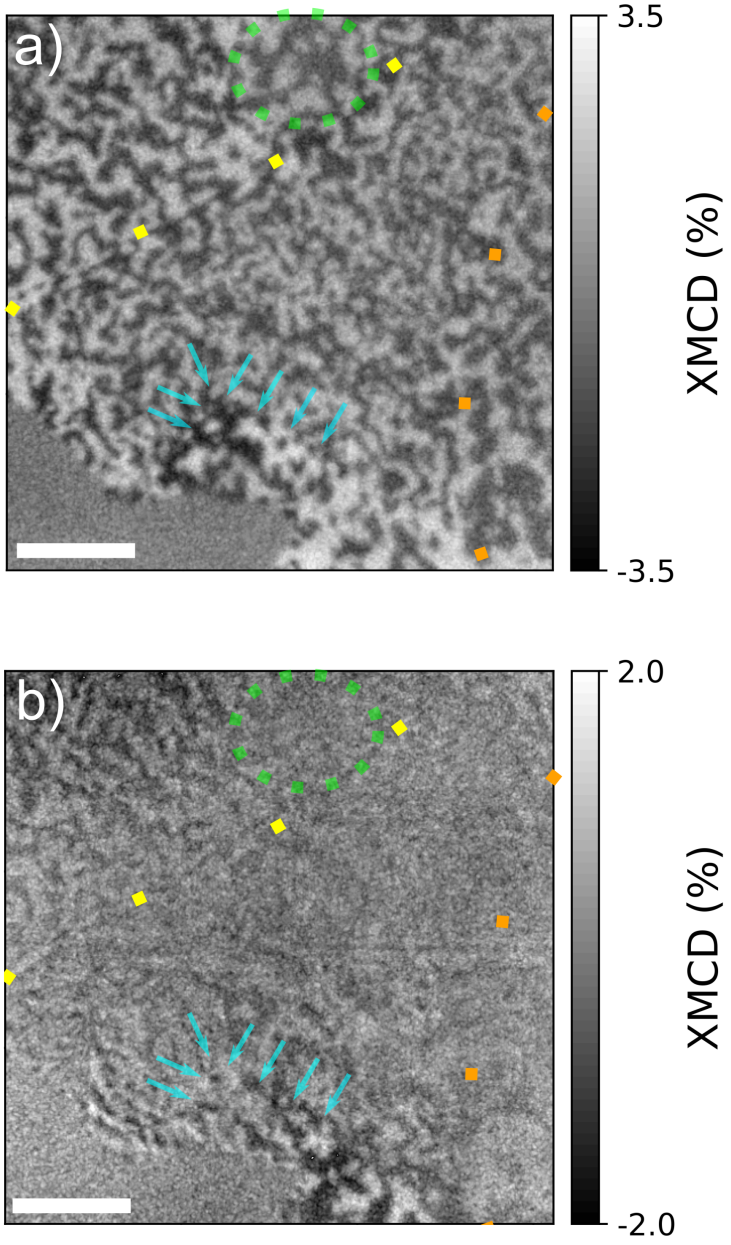


Figure 5.17: **a)** OOP and **b)** IP magnetization components of 4 L, 5 L and 6 L Fe_5GeTe_2. The XPEEM measurement was performed by Dr. Mohamad A. Mawass and Dr. Florian Kronast at UE49-PGMa at BESSY II. The measurement temperature was 50 K. Scale bar = 2 µm.

For $Fe_{5-x}GeTe_2$, where $x < 1$, the magnetic parameter space is extremely large. For instance, a large PMA [143] and a helical ground state [144] are just two of the many possible ground states. Gate-tuning may be one way to access similar magnetic phases across samples prepared differently from one another [145].

5.6 Spin Reorientation in 5 L and 6 L Fe_5GeTe_2

The magnetic domain structures in 2 L, 3 L and 4 L Fe_5GeTe_2 strongly suggest competition between K_u and K_d as the layers become thinner. This behavior is unusual, because in most vdW magnets [6, 8, 17], the magnetic anisotropy energy becomes much larger than other terms, forcing a uniform magnetization.

This anisotropy reduction requires further experimental verification. In XPEEM, a change in the anisotropy can be confirmed by comparing the OOP and IP magnetization components (Chapter 2.7) as a function of layer thickness for atomically thin Fe_5GeTe_2. For the sample discussed in the previous section, the IP and OOP XPEEM images demonstrate that there is an IP spin canting which occurs in a 5 L flake, whereas the magnetization in 6 L is nearly fully OOP, thus demonstrating the reduction of K_u for thinner layers (Figure 5.17).

It should be noted that in contrast to the Fe-deficient region bounded by blue triangles, the photoemission yield from the Fe L_3 edge is homogenous, and there is no evidence of a change in chemical composition across the 6 L-5 L boundary. The change in K_u seems to originate from the change in the layer thickness. However, this decrease in K_u is not universal; there is no clear change in the IP magnetization at the 4 L-6 L boundary, meaning that unlike 5 L, the 4 L magnetization is mostly OOP. These data should be interpreted as a proof-of-principle of stabilization of complex magnetic domains in atomically thin Fe_5GeTe_2, rather than a absolute and definitive characterization of the magnetic properties of Fe_5GeTe_2.

5.7 Conclusion

Thickness-dependent ferromagnetic domains were characterized for bulk and atomically thin Fe_5GeTe_2, a high-T_C vdW ferromagnet with a weak PMA. Labyrinth-type domains in the bulk are indicative of competition between K_u and K_d. However, in contrast to uniaxial ferromagnets such as Fe_3GeTe_2 for which a single domain is the most energetically preferred state, the magnetization in atomically thin Fe_5GeTe_2 is characterized by many domains, implying an enhancement of K_d relative to K_u in the atomically thin limit. However, NVSM reveals the presence of pinning sites, which contribute to enhanced H_{sat} in the few-layer limit [30]. The domain structure in atomically thin Fe_5GeTe_2 could therefore simply show the pinned domains. However, the XPEEM data show domains in demagnetized Fe_5GeTe_2, as no field was applied, meaning that layer-dependent domain structures likely originate from changes in relative energy contributions. Moreover, domain wall motion (Figure 5.11) and hysteresis (Figure 5.12) revealed by NVSM demonstrates that the pinning sites constitute a finite, yet limited contribution to the magnetic response; a direct correspondence between domains in demagnetized Fe_5GeTe_2 and pinning sites is rather unlikely. Thus, the thickness dependence of the ferromagnetic domain structure as well as IP spin canting for 5 L Fe_5GeTe_2 demonstrate intercompeting K_u and K_d in the few-layer limit.

6 | Vortex-antivortex pairs in atomically thin Fe_5GeTe_2

6.1 Easy-plane ferromagnetism in Fe_5GeTe_2

The 2D magnetic materials thus far considered, including $CrSiTe_3$, Fe_3GeTe_2, and Fe_5GeTe_2, have an easy-axis magnetic anisotropy. However, 2D easy-plane magnetism has not yet been discussed. For Fe_5GeTe_2, the magnetic anisotropy is weak compared to Fe_3GeTe_2, and varies between easy-axis [22] and easy-plane [46] for differing stoichiometric compositions, temperatures and thicknesses. In detail, bulk Fe_5GeTe_2 has an easy-plane anisotropy from room temperature to 190 K. However, in between 190 and 112 K, the anisotropy axis transitions to the easy axis [146, 147]. This chapter will discuss ferromagnetism and magnetic domains in 4 L Fe_5GeTe_2, for which the demagnetization energy (K_d) and uniaxial anisotropy energy (K_u) are likely to compete with one another [22]. This may result in a shape-induced easy-plane anisotropy for a broader range of temperatures.

In particular, easy-plane magnetism which is otherwise isotropic within the plane is described by the XY model (Chapter 1.5) [18]. Counter-intuitively, the 2D XY model is not sufficient to induce a transition to long range order [18]. However, bound pairs of vortices and antivortices have been predicted to form on shorter length scales below a finite temperature, coinciding with a divergence of the magnetic susceptibility (Chapter 1.5) [18, 19]. In the case of atomically thin Fe_5GeTe_2, for which ferromagnetism is observed down to 4 L (Section 6.4), it is unclear whether the magnetism is strictly 2D due to the exchange interactions among the many Fe atoms within the unit cell [129]. In addition, deviations of the magnetization away from the easy plane are conceivable due to the weak anisotropy of Fe_5GeTe_2 [22] or the presence of DMI [20, 148]. Nevertheless, easy-plane magnetic domains and pairs of magnetic vortices and antivortices are observed in 4 L Fe_5GeTe_2, and will be extensively discussed in Section 6.4. The magnetic behavior of $CrCl_3$, a bulk easy-plane vdW antiferromagnet, for

which a ferromagnetic monolayer is antiferromagnetically coupled to its adjacent neighbors, is also well-described by the XY model [149, 150]. In particular, easy-plane anisotropy which is otherwise isotropic in the *ab* plane has been confirmed [149]. However, no real-space imaging of the magnetism has been performed in atomically thin easy-plane vdW magnets to date.

6.2 Vortices in magnetic systems

In general, the magnetization within spatially confined particles including nanodisks [151], island-type growths [152], and patterned thin films [133] will assume different arrangements compared to that of their macroscopic counterparts. In detail, it is energetically favorable for the system to reduce K_{d}, while the enhanced anisotropy in such nanoparticles prevents the separation of the magnetization into smaller domains. The optimal magnetization configuration is that of a whirling vortex, for which both domain wall energy (σ_{w}) and K_{d} are simultaneously reduced.

Merons, which are quasiparticles with a topological index of $N = \pm 1/2$, are topologically equal to one-half of the well-studied skyrmions for which $N = \pm 1$ [153]. In real space, merons appear as a winding of the local magnetization with helicity w (Figure 6.1). Furthermore, merons, which also have cores polarized in the OOP direction, are topologically inequivalent to trivial magnetic vortices for which the magnetization lies completely IP. As a consequence, merons form in pairs in order to maintain an integer topological unit in magnetic systems [154] (Section 6.4). For such bimerons, the two cores have opposite polarizations with respect to one another. Magnetic bimerons can form ordered lattices [153] or stochastic arrangements [154] depending on properties of the magnetic system.

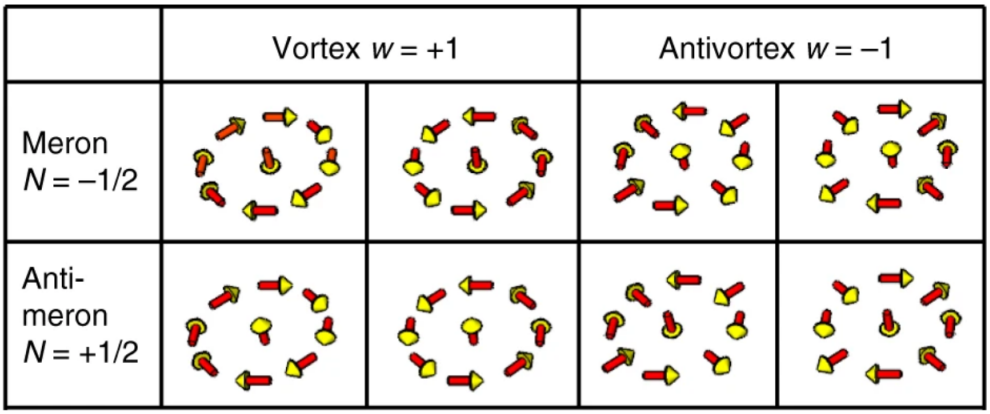


Figure 6.1: Spin textures with $N = \pm 1/2$. For a given spin texture, N is characterized by w and the OOP polarization at the core. Figure adapted from Ref. [155].

6.3 Methods

6.3.1 Bulk sample characterization

Single crystals of Fe_5GeTe_2 were grown with CVT by Dr. Andrew May at Oak Ridge National Laboratory [46]. The crystals were immediately quenched in an ice-water bath from a growth temperature of 1023 K and subsequently cooled below 100 K. For these quench-cooled (QC) crystals, the quenching step improves the crystallinity, as demonstrated by sharper diffraction peaks compared to non-quenched (NQ) furnace-cooled crystals [46]. The cooling step below 100 K induces magnetostructural changes in the lattice. Specifically, a decrease in c/a near 100 K and an increase in T_C from 270 to 310 K are observed. The enhancement of T_C is permanent, meaning that it remains for repeated thermal cycling until at least 380 K. No significant differences in the anisotropic behavior of the magnetism exist between the NQ and QC types, although it could be argued that the easy-plane anisotropy is slightly more prominent for the QC type for temperatures of 190 K and greater. This inference is made based on the isothermal magnetization data in Ref. [146].

6.3.2 Exfoliation of atomically thin Fe_5GeTe_2

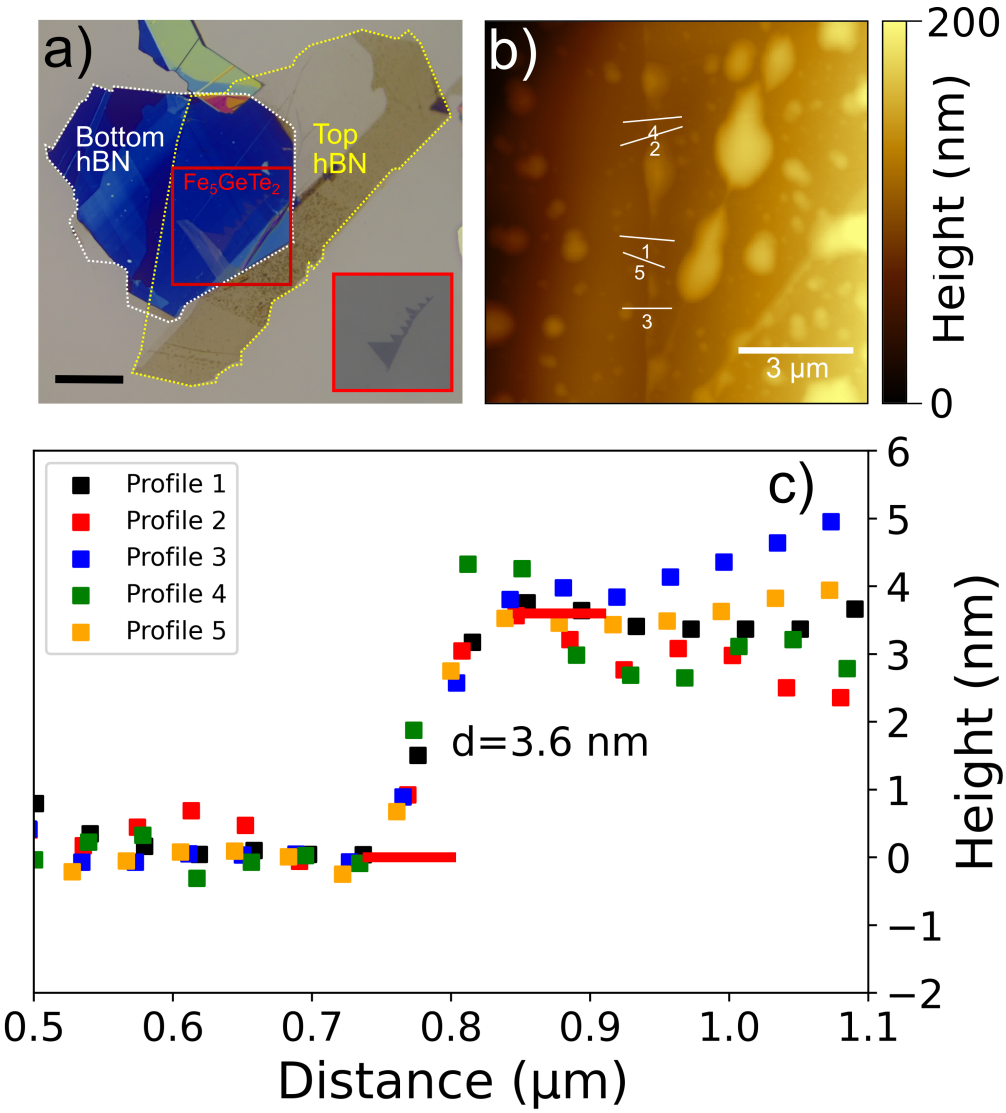


Figure 6.2: a) Optical micrograph of the exfoliated Fe_5GeTe_2 flake encapsulated between top and bottom hBN. An image of the flake on PDMS is shown in the inset. Scale bar = 50 µm. **b)** AFM topography map of the encapsulated Fe_5GeTe_2 flake obtained after the XPEEM measurement. **c)** Line profiles obtained from the AFM topography map. $d = 3.6$ nm corresponds to 4 L of Fe_5GeTe_2, which has a monolayer thickness of 0.8 nm [46]. The additional height of 0.4 nm may be due to artificial enhancement from the surrounding blisters in the hBN.

Single crystals of hBN, graphite and QC-type Fe_5GeTe_2 [46] were mechanically exfoliated with a PDMS-assisted transfer method [36] in a glovebox with oxygen and moisture levels below 10 ppm. Thin flakes of hBN were stacked on top of a conductive Si substrate. Next, a thin graphite flake was placed on top, forming a conductive pathway to the substrate. Next, a thin flake of Fe_5GeTe_2 was stacked on top of the Si/hBN/graphite heterostructure. Finally, another thin flake of hBN was placed to encapsulate the Fe_5GeTe_2, forming Si/hBN/graphite/Fe_5GeTe_2/hBN.

6.4 Vector imaging of vortex-antivortex pairs in 4 L Fe_5GeTe_2

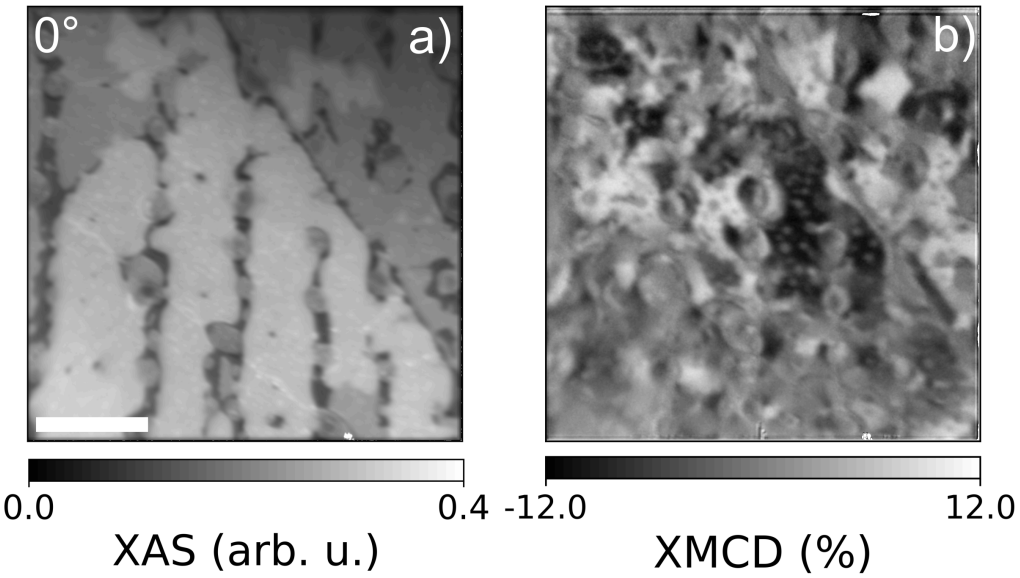


Figure 6.3: a) X-ray absorption spectra (XAS) and **b)** X-ray magnetic circular dichroism (XMCD) images of 4 L Fe_5GeTe_2 obtained at an azimuthal angle of 0°. The field of view is 10 µm. These data were obtained by Dr. Florian Kronast, Dr. Alevtina Smekhova and Ryuji Fujita at UE49-PGMa, BESSY II. The thickness of the Fe_5GeTe_2 sample was 4 L (approximately 3.6 nm). The measurement temperature was 50 K. The photon energy was 706.2 eV (Fe L_3 edge). Scale bar = 2 µm.

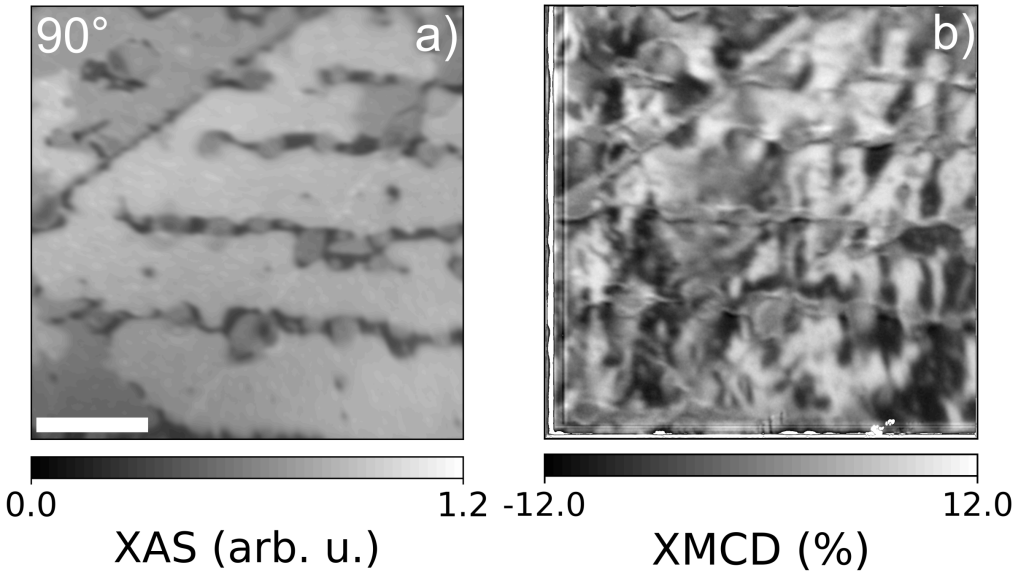


Figure 6.4: a) X-ray absorption spectra (XAS) and **b)** X-ray magnetic circular dichroism (XMCD) images of 4 L Fe_5GeTe_2 obtained at an azimuthal angle of 90°. The field of view is 10 µm. These data were obtained by Dr. Florian Kronast, Dr. Alevtina Smekhova and Ryuji Fujita at UE49-PGMa, BESSY II. The thickness of the Fe_5GeTe_2 sample was 4 L (approximately 3.6 nm). The measurement temperature was 50 K. The photon energy was 706.2 eV (Fe L_3 edge). Scale bar = 2 µm.

XPEEM measurements at the Fe L_3 edge (706.2 eV) were performed at 50 K (Chapter 2.7). The IP vector images were acquired from XMCD images at 0° (Figure 6.3) and 90° (Figure 6.4) azimuthal angles. Note that these vector images only show the orientation of the IP magnetization, and not the full IP and OOP projection, for which data sets from at least three azimuthal angles are required. An IP demagnetization sequence of a maximum amplitude of 100 mT was applied at 50 K prior to the XPEEM measurement.

Many instances of vortices and antivortices can be observed in the vector images of the IP magnetization for 4 L Fe_5GeTe_2. Moreover, the XMCD image obtained at 0° (Figure 6.3) differs significantly from the one obtained at 90° (Figure 6.4), indicating that the magnetization lies predominantly within the sample plane. Strictly speaking, it is not possible to determine if these vortex-antivortex pairs

are meron-antimeron pairs from the IP vector maps alone, as merons have an OOP-polarized core.

6.4.1 Vortex-antivortex formation in 4 L Fe_5GeTe_2

The in-plane magnetization in 4 L Fe_5GeTe_2 was characterized with XPEEM vector imaging. The measurement temperature was 50 K. In general, it can be seen in Figures 6.5 and 6.6 that the magnetization consists predominantly of ferromagnetic domains with planar anisotropy. Within the sample plane, the magnetization appears to be isotropic, compared to other planar vdW ferromagnets with magnetostructural anisotropy [156, 157]. Moreover, there is a distribution of vortices and antivortices. This distribution is stochastic, as predicted in Monte Carlo simulations performed by Augustin, et al [154]. This is particularly exemplified in Figure 6.6, in which the nucleation of vortices and antivortices appears to be random, and is independent of any magnetic anisotropy or the underlying crystal structure. The stochastic nucleation of vortices stands in contrast to the so-called meron crystals for which the vortices and antivortices form a periodic lattice as a result of multi-Q ordering [158, 159]. Among the vortices shown in Figure 6.5 and Figure 6.6, the helicity varies between Bloch and Néel-type magnetization arrangements [158]. For example, in Figure 6.5, the vortex labelled as 3 could be a Néel-type meron [160]. The variable chirality could indicate the lack of a strong DMI, as was the case in Chapter 5.

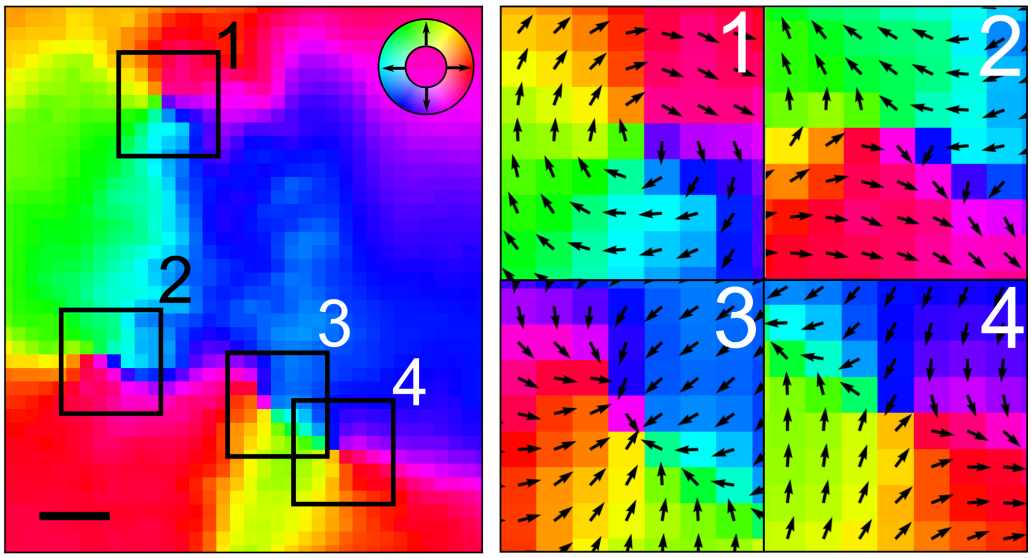


Figure 6.5: XPEEM vector image of ferromagnetic domains in 4 L Fe_5GeTe_2 showing vortices and antivortices labelled as **1**, **2**, **3** and **4**. A close-up of the magnetization shown in **3** reveals a Néel-type magnetization ordering [160]. These data were obtained by Dr. Florian Kronast, Dr. Alevtina Smekhova and Ryuji Fujita at UE49-PGMa, BESSY II. The thickness of the Fe_5GeTe_2 sample was 4 L (approximately 3.6 nm). The bulk parent compound was synthesized by Dr. Andrew May at the Oak Ridge National Laboratory. The measurement temperature was 50 K. Scale bar = 100 nm.

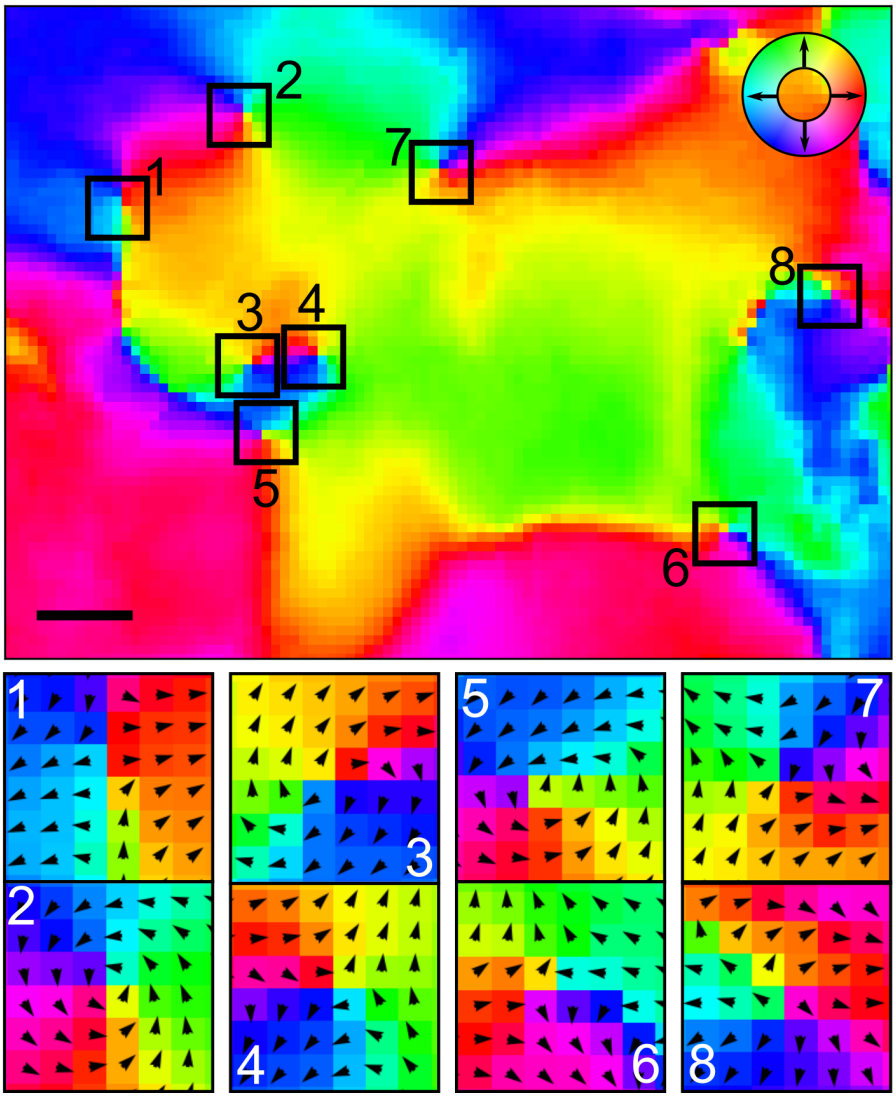


Figure 6.6: XPEEM vector image of the magnetization in 4 L Fe_5GeTe_2 showing vortices (labelled as **2**, **3**, **5** and **8**) and antivortices (labelled as **1**, **4**, **6** and **7**). The nucleation of vortices and antivortices appears to be stochastic, and independent of an underlying anisotropy or crystal structure. Some of the domain walls, particularly in between **5** and **6**, spans some hundreds of nm, which may reflect a reduction of the exchange interaction energy or magnetic frustration [154]. These data were obtained by Dr. Florian Kronast, Dr. Alevtina Smekhova and Ryuji Fujita at UE49-PGMa, BESSY II. The measurement temperature was 50 K. The thickness of the Fe_5GeTe_2 sample was 4 L (approximately 3.6 nm). The bulk parent compound was synthesized by Dr. Andrew May at the Oak Ridge National Laboratory. Scale bar = 100 nm.

6.4.2 Localized vortex-antivortex pairs in 4 L Fe_5GeTe_2

Vector images of the in-plane magnetization in 4 L Fe_5GeTe_2 were obtained at a measurement temperature of 50 K, and are shown in Figures 6.8, 6.9, 6.10, 6.11 and 6.12. These figures show vortices and antivortices which are contained within larger domain walls. The magnetization shown in these figures also demonstrate the lack of a magnetic anisotropy within the XY plane, a characteristic of the XY model (Chapter 1.5).

Qualitatively, there seems to be little energetic cost associated with the planar deformation of the magnetization on local length scales. For example, in Figure 6.7, a domain is shown in green and another domain is shown in violet. These two domains are adjacent to one another, and a domain wall shown in blue facilitates a continuous transition of the magnetization between the two domains. This domain wall accommodates a rotation of the magnetization of approximately 90°.

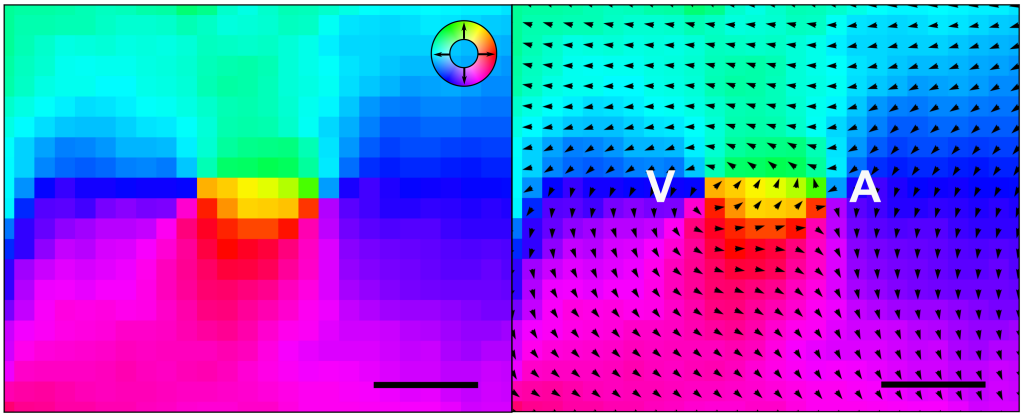


Figure 6.7: XPEEM vector image of the magnetization in 4 L Fe_5GeTe_2, which shows a localized deformation of the magnetization within the blue domain wall. A vortex (labelled as **V**) and antivortex (labelled as **A**) can be found on the ends of this localized deformation, and could signify a change of the exchange energy, or magnetic frustration [154]. These data were obtained by Dr. Florian Kronast, Dr. Alevtina Smekhova and Ryuji Fujita at UE49-PGMa, BESSY II. The thickness of the Fe_5GeTe_2 sample was 4 L (approximately 3.6 nm). The bulk parent compound was synthesized by Dr. Andrew May at the Oak Ridge National Laboratory. The measurement temperature was 50 K. Scale bar = 100 nm.

However, a local deformation of the magnetization within the domain wall can be found at the center of the image (Figure 6.7). A vortex (labelled as **V**) and an antivortex (labelled as **A**) can be found at the ends of this local deformation. Relative to the domain wall shown in blue, this deformation contributes an additional planar rotation of 90°, accommodating a total rotation of 180° across the magnetization shown in green, yellow and red (Figure 6.7). One may question why it is energetically favorable for there to be a local deformation of the magnetization, which deviates from the magnetization profile of the surrounding domain wall.

When considering the origins of such magnetization textures in easy-plane ferromagnets, we can evaluate the effects of long-range dipole interactions and microscopic exchange interactions. In thin films, dipole fields will usually induce an easy-plane anisotropy. Furthermore, Augustin, et al. predict the formation of long-range dipole fields which interconnect vortices and antivortices. Such dipole fields span some tens to hundreds of nm [154], suggesting that they play a key role in the stabilization of vortices and antivortices.

On atomic length scales, exchange interactions among the lattice sites influence the magnetism. In particular, for 1 L $CrCl_3$, higher-order exchange interactions, which compete with one another, are considered up to the 3rd nearest neighbor [154]. The exchange interaction for the 3rd nearest neighbor is predicted to be antiferromagnetic relative to the 1st and 2nd nearest neighbor. This is a form of magnetic frustration, and is also predicted to contribute to local deformations within domain walls, and the formation of vortices and antivortices [154].

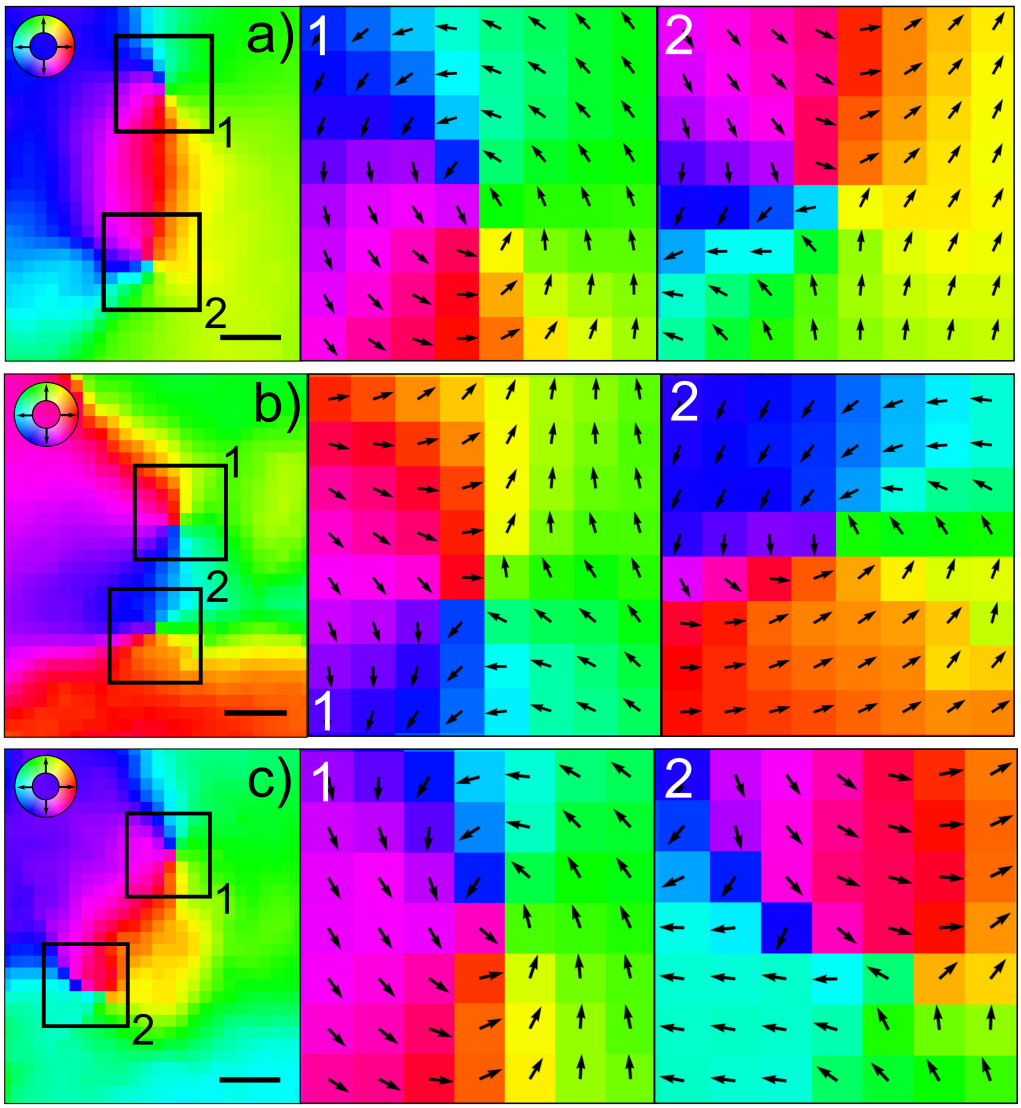


Figure 6.8: a, b, c) XPEEM vector images of localized pairs of vortices and antivortices. In each case, the vortex-antivortex pair is part of the larger domain wall, and can be characterized as significant deviations in the local magnetization. These data were obtained by Dr. Florian Kronast, Dr. Alevtina Smekhova and Ryuji Fujita at UE49-PGMa, BESSY II. The thickness of the Fe_5GeTe_2 sample was 4 L (approximately 3.6 nm). The bulk parent compound was synthesized by Dr. Andrew May at the Oak Ridge National Laboratory. The measurement temperature was 50 K. Scale bars = 100 nm.

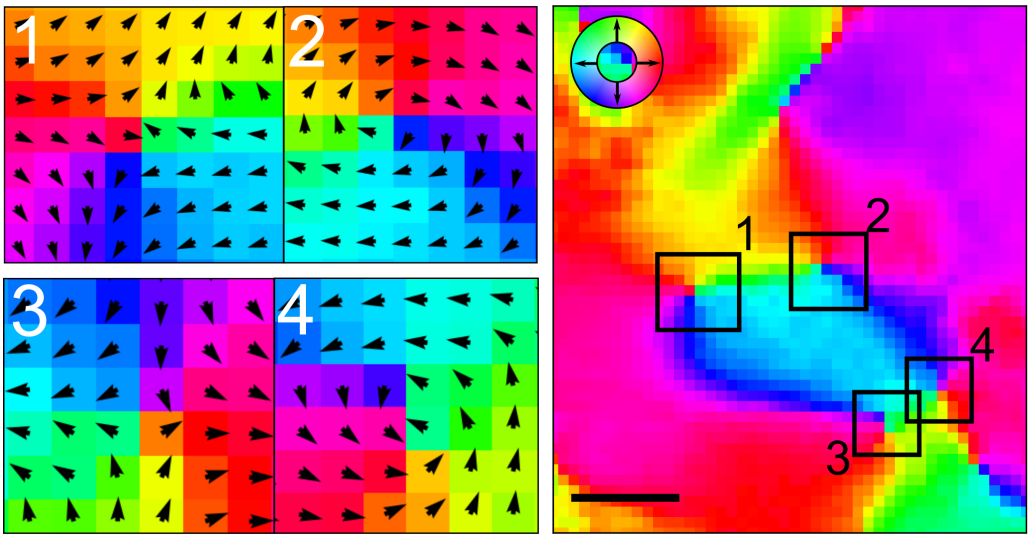


Figure 6.9: a) XPEEM vector image of vortices (labelled as **2** and **4**) and antivortices (labelled as **1** and **3**). Compared to Figure 6.8, the vortices and antivortices form over comparable length scales of some hundreds of nm. These data were obtained by Dr. Florian Kronast, Dr. Alevtina Smekhova and Ryuji Fujita at UE49-PGMa, BESSY II. The thickness of the Fe_5GeTe_2 sample was 4 L (approximately 3.6 nm). The bulk parent compound was synthesized by Dr. Andrew May at the Oak Ridge National Laboratory. The measurement temperature was 50 K. Scale bar = 200 nm.

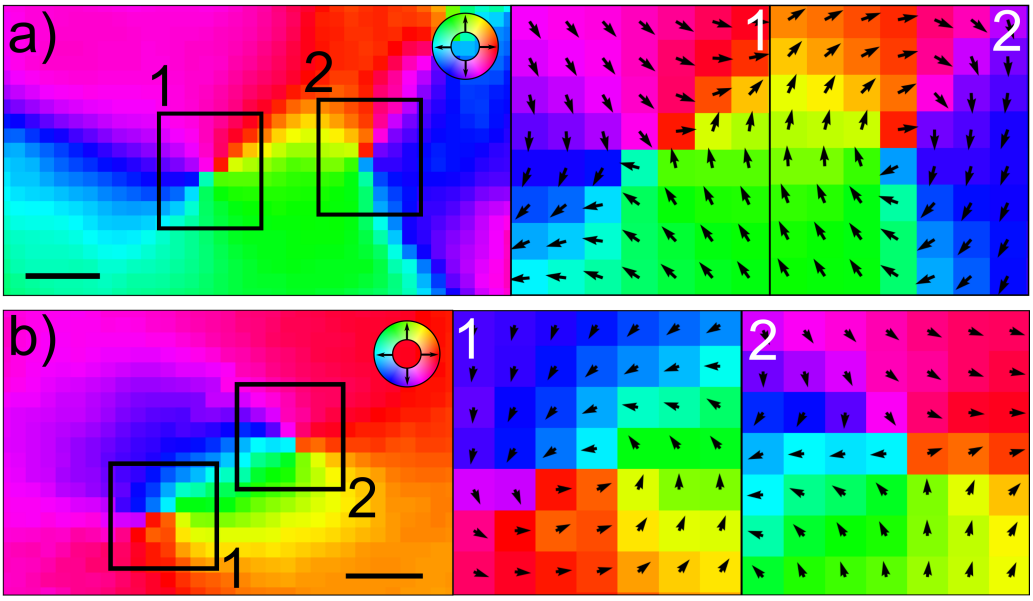


Figure 6.10: a, b) XPEEM vector images of vortices and antivortices within close proximity to each other. These local deviations of the magnetization could signify a reduction of the exchange energy, or magnetic frustration [154]. These data were obtained by Dr. Florian Kronast, Dr. Alevtina Smekhova and Ryuji Fujita at UE49-PGMa, BESSY II. The measurement temperature was 50 K. The thickness of the Fe_5GeTe_2 sample was 4 L (approximately 3.6 nm). The bulk parent compound was synthesized by Dr. Andrew May at the Oak Ridge National Laboratory. Scale bars = 100 nm.

Figure 6.10b shows a vortex-antivortex collision. Assuming that the observed vortex-antivortex pairs are a manifestation of BKT theory, such a strong binding among vortices and antivortices suggests that the measurement temperature of 50 K is below T_{KT}, for which strong binding, collision and subsequent annihilation of vortex-antivortex pairs is predicted [18, 19]. The data presented in Figure 6.10b bear a qualitative resemblance to meron-antimeron collisions [154] considered by Augustin, et al. However, such collisions are dynamic processes occurring on short time scales, meaning that domain wall pinning in Fe_5GeTe_2 [30] may be preventing subsequent vortex-antivortex annihilation. Conversely, a potential follow-up measurement should consist of warming the sample above 50 K to search for the dissociation of vortex-antivortex pairs into isolated constituents.

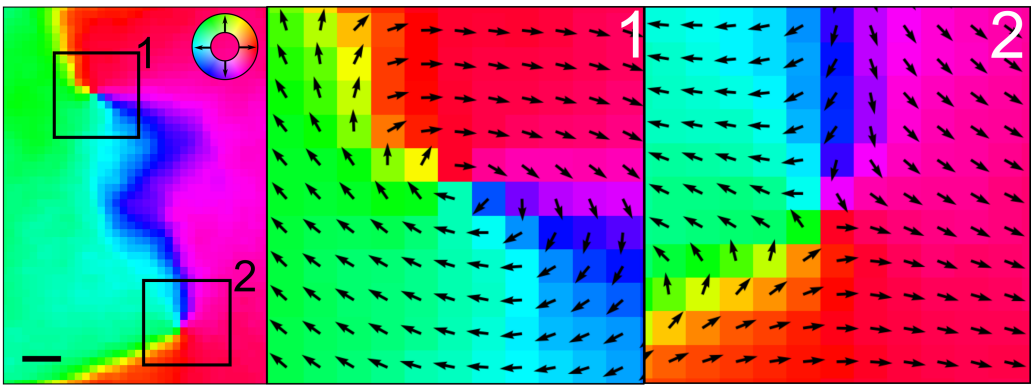


Figure 6.11: a) XPEEM vector image of a vortex (labelled as **1**), antivortex (labelled as **2**) and a deformation of the domain wall profile (shown in blue). The vortex (**1**) and antivortex (**2**) are separated by a longer distance, compared to Figures 6.8, 6.9, and 6.14. In between **1** and **2**, a localized deformation of the magnetization, shown in blue, spans some hundreds of nm. These data were obtained by Dr. Florian Kronast, Dr. Alevtina Smekhova and Ryuji Fujita at UE49-PGMa, BESSY II. The measurement temperature was 50 K. The thickness of the sample is 4 L (approximately 3.6 nm). The bulk parent compound was synthesized by Dr. Andrew May at the Oak Ridge National Laboratory. Scale bar = 100 nm.

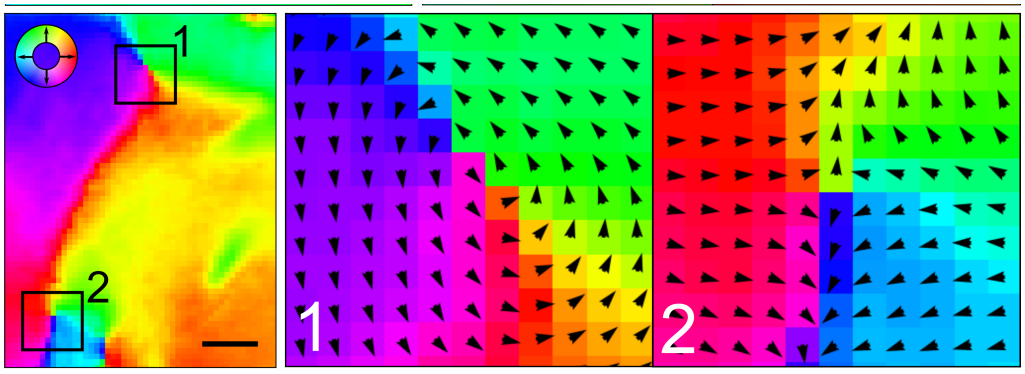


Figure 6.12: XPEEM vector maps of the magnetization in 4 L Fe_5GeTe_2, showing a vortex (labelled as **1**) and antivortex (labelled as **2**). Compared to Figure 6.11, the separation between the vortex (**1**) and antivortex (**2**) is even greater, and exceeds 1 µm. These data were obtained by Dr. Florian Kronast, Dr. Alevtina Smekhova and Ryuji Fujita at UE49-PGMa, BESSY II. The measurement temperature was 50 K. The thickness of the sample is 4 L (approximately 3.6 nm). The bulk parent compound was synthesized by Dr. Andrew May at the Oak Ridge National Laboratory. Scale bar = 200 nm.

6.4.3 Helicity variations in vortex-antivortex pairs

The vortices described in Section 6.4.2 are characterized by either a right-handed or left-handed helicity, which is characteristic of Bloch-type spin ordering [160]. However, a small minority of vortices are characterized by a reduced helicity. Such vortices, which occur 4 out of 38 times for an investigated area of 10 µm × 10 µm, are characteristic of Néel-type magnetization [160], and are shown in Figures 6.13 and 6.14. However, they are rather scarce in occurrence compared to the Bloch-type vortices which are characterized by a right-handed or left-handed helicity (Section 6.4.2). These Bloch-type vortices are usually found within a larger domain wall together with an antivortex (Sections 6.4.1 and 6.4.2).

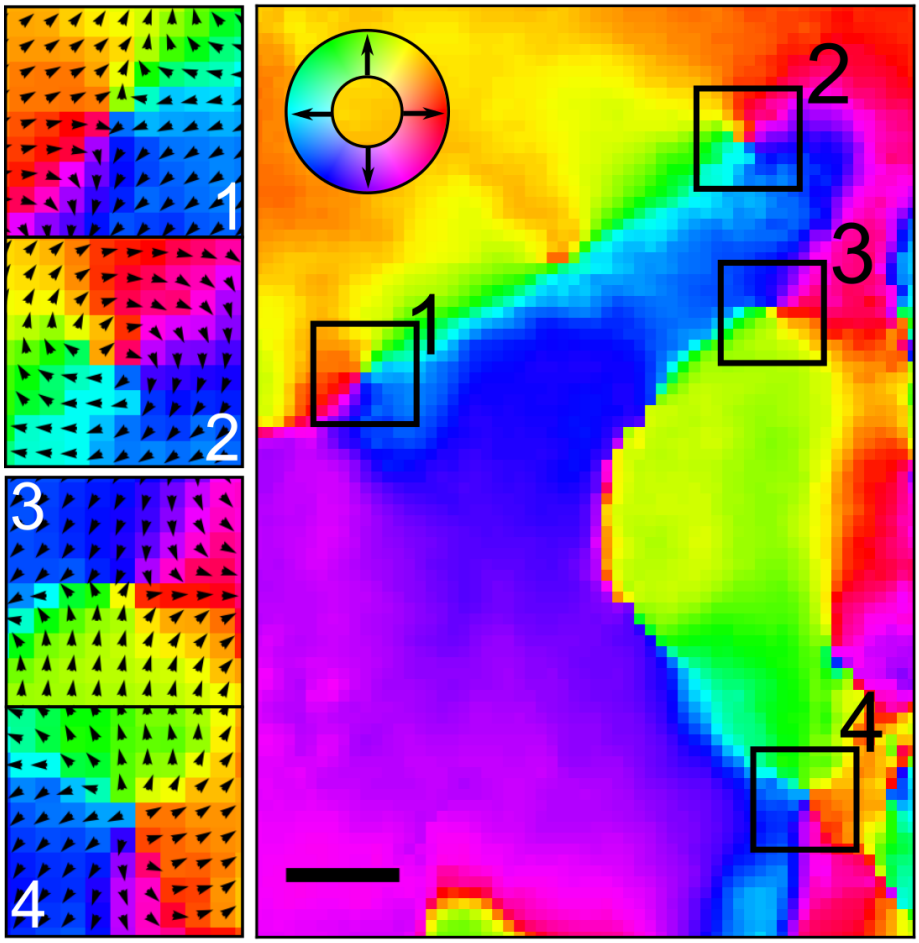


Figure 6.13: a) XPEEM vector image of vortices (labelled as **2** and **4**) and antivortices (labelled as **1** and **3**). The vortex labelled as **2** shows a Bloch-type magnetization, while the vortex labelled as **4** shows a Néel-type magnetization [160]. The varying vortex helicity could reflect the spatial variation of the DMI [161]. These data were obtained by Dr. Florian Kronast, Dr. Alevtina Smekhova and Ryuji Fujita at UE49-PGMa, BESSY II. The measurement temperature was 50 K. The thickness of the sample is 4 L (approximately 3.6 nm). The bulk parent compound was synthesized by Dr. Andrew May at the Oak Ridge National Laboratory. Scale bar = 100 nm.

It is possible to make some qualitative inferences and predictions regarding the dynamic behavior of the vortices and antivortices by observing that a vortex and antivortex is always contained within a domain wall. This is particularly

exemplified by Figures 6.8, 6.10 and 6.11, in which a localized deviation of the domain wall accommodates the vortex and antivortex. These deviations vary in length from 100 to 1000 nm, which implies that the vortex and antivortex initially nucleate from a singular point within the domain wall.

However, according to the BKT formalism, vortices and antivortices stochastically nucleate for temperatures above T_{KT} [154]. Below T_{KT}, these vortices and antivortices will combine into vortex-antivortex pairs which share close mutual proximity.

Yet another viewpoint considers the effect of the DMI on the spatial profile of meron-antimeron pairs. In detail, Bachmann, et al. finds that for the weak-DMI limit, merons and antimerons form tightly bound pairs, otherwise known as bimerons, while in the large-chirality limit, further separation and eventual detachment of merons is predicted. The localized nature of vortices and antivortices shown in Figures 6.8 and 6.10 may reflect a relatively small DMI contribution, while vortices and antivortices separated by somewhat longer distances, such as those shown in Figure 6.9, may reflect a stronger DMI contribution. In other words, the variations of the spatial profiles of vortices and antivortices shown in Sections 6.4.1, 6.4.2 and 6.4.3 could reflect a spatially varying DMI, which has been observed in Fe_5GeTe_2. Indeed, this material is characterized by a high density of structural irregularities and stacking faults [46, 148]. Furthermore, domain wall pinning [30] may also affect the spatial profile of the vortex and antivortex.

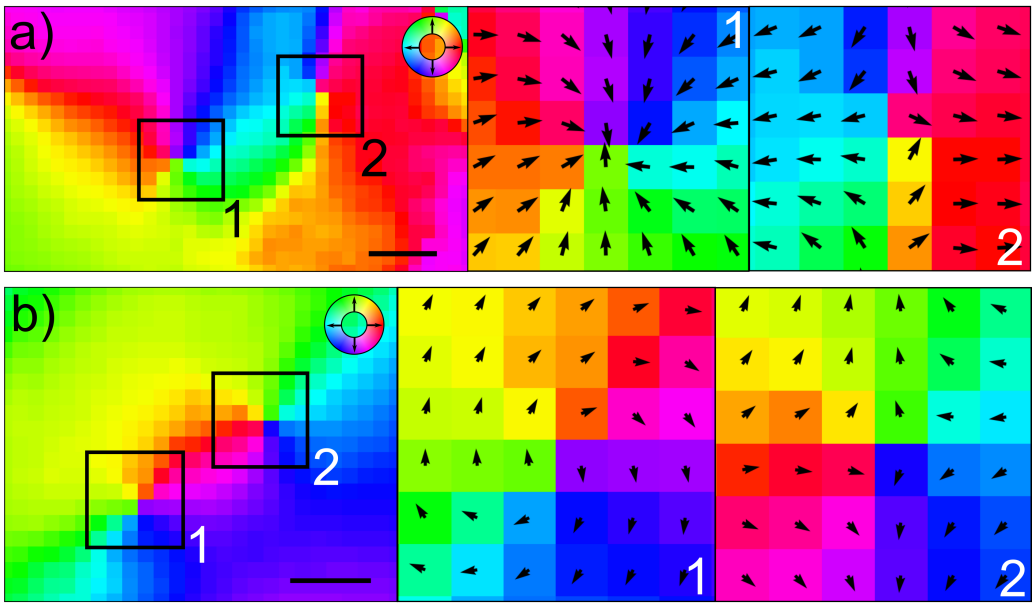


Figure 6.14: a) XPEEM vector image of a Néel-type vortex [160] (labelled as **1**) in close proximity to an antivortex (labelled as **2**). **b)** XPEEM vector image of a vortex (labelled as **1**), which may be characterized as having a slightly reduced chirality compared to other Bloch-type vortices, such as those shown in Figures 6.10 or 6.13. The vortex (**1**) is in close proximity to an antivortex (labelled as **2**). The variable chirality may indicate either a weak or spatially varying DMI [161]. These data were obtained by Dr. Florian Kronast, Dr. Alevtina Smekhova and Ryuji Fujita at UE49-PGMa, BESSY II. The measurement temperature was 50 K. The thickness of the sample is 4 L (approximately 3.6 nm). The bulk parent compound was synthesized by Dr. Andrew May at the Oak Ridge National Laboratory. Scale bars = 100 nm.

6.5 Conclusion

Easy-plane ferromagnetism and pairs of vortices and antivortices were found in 4 L Fe_5GeTe_2. These findings demonstrate the formation of magnetic domains which may be influenced by a reduced exchange energy, or magnetic frustation [154], in contrast to single domains separated by well-defined domain walls which are found in atomically thin easy-axis vdW ferromagnets. Furthermore, bound pairs of vortices and antivortices may be a manifestation of predictions made by Berezenskii [18], Kosterlitz [19] and Thouless regarding the 2D XY

model. Future work include the characterization of the topological properties of vortex-antivortex pairs by measuring the OOP magnetization component and searching for signs of thermally induced dissociation into isolated constituents above T_{KT}.

Moreover, these findings could be used to test proposals of characterizing Majorana bound states in hybrid superconductor-ferromagnet heterostructures [26], for which limited quenching of the superconductivity [162, 163], as well as the atomic flatness of Fe_5GeTe_2, could be advantageous for synthesizing a vdW heterostructure. In this regard, a particularly well-suited vdW superconductor may be $NbSe_2$ [162], which has a critical temperature of 5 K and can be readily exfoliated down to the monolayer.

7 | Conclusions and outlook

Despite fundamental constraints which have been thought to prevent the stabilization of magnetic order in the 2D limit (Chapter 1.4), ferromagnetism has been observed for 2D materials with significant uniaxial anisotropy. In fact, 2D vdW materials have specific properties which make them conducive to characterize fundamental magnetic properties; the ability to stack 2D materials on top of one another, mechanical flexibility, electrostatic tunability, and susceptibility to optical excitation motivate the inclusion of magnetism in the broader family of vdW materials. In this thesis, ferromagnetism in atomically thin vdW materials is characterized. Specifically, methodologies of modifying the intrinsic ferromagnetic domain structure in uniaxial vdW ferromagnets, and of stabilizing magnetic domains which are governed by fundamentally different interactions compared to those found in uniaxial vdW ferromagnets, are demonstrated. In particular, XMCD spectroscopy and magnetic domain analysis are implemented to make inferences regarding fundamental characteristics of easy-axis and easy-plane vdW ferromagnets. Moreover, this thesis encourages future implementation of atomically thin vdW magnets to test several outstanding hypotheses in condensed matter physics, which has so far been unfeasible due to a lack of suitable material platforms. Specifically, several aspects of 2D Fe_5GeTe_2, an easy-plane vdW ferromagnet, could be implemented to evaluate proposals regarding topological spin textures and quantum computation.

7.1 Summary of results

In detail, this thesis begins by considering how Ising-type ferromagnetism changes as a function of layer thickness in Chapter 3. High-field XMCD spectroscopy is utilized to characterize the ferromagnetism in $CrSiTe_3$ as a function of layer number. It is found that T_C is dependent on the number of layers; no monolayer ferromagnetism is observed at 10 K, while finite H_c is observed only for 3 L and thicker, implying a small, yet non-negligible interlayer exchange interaction for this vdW ferromagnet which has 2D Ising-type critical behavior in

the bulk limit. In addition, the ratio m_l/m_s increases for thinner $CrSiTe_3$, which could be a sign of enhanced Cr-Te hybridization in the atomically thin limit [65]. These results show that even for a vdW magnet with 2D Ising-type ordering in the bulk, magnetic properties still vary as a function of layer thickness.

Chapter 4 demonstrates a novel method of tuning the magnetic properties of Fe_3GeTe_2, a vdW ferromagnet with meander-type domains which form as a result of the large magnetic anisotropy. For Fe_3GeTe_2, the metallic conduction makes electrostatic gate-tuning difficult to implement [17], motivating other methods of tuning the ferromagnetism. Specifically, the incorporation of α-In_2Se_3, a vdW piezoelectric, compressively strains Fe_3GeTe_2, reducing T_C and σ_w. These inferences are made by analyzing the magnetic domain structure at varying temperature with XPEEM. Furthermore, Raman microscopy reveals a reduction of the Tuinstra-Koening relation, $I(D)/I(G)$, in a graphite/α-In_2Se_3 heterostructure, demonstrating that strain-tuning with α-In_2Se_3 can be extended to a broader class of vdW heterostructures, as well as graphene-based moíre systems. For MTJs [24, 25], the *in-situ* strain-tuning of the magnetoresistance ratio may be one way to realize energy-efficient magnetic memories at relatively high temperatures. Furthermore, a direct coupling between ferromagnetic and piezoelectric domains may enable the magnetic state to be written by electrical means, which is comparatively easier to implement in devices compared to applying a magnetic field.

The influence of the uniaxial anisotropy of ferromagnetism in 2D vdW magnets are covered in Chapters 4 and 5. In Chapter 5, Fe_5GeTe_2, a vdW ferromagnet with a weak uniaxial anisotropy and a bulk T_C near room temperature is discussed. In detail, XPEEM measurements reveal labyrinth-type domains in the bulk limit. The high density of domain walls compared to bulk Fe_3GeTe_2 suggests that Fe_5GeTe_2 has a smaller domain wall energy (σ_w), and thus uniaxial anisotropy compared to Fe_3GeTe_2. In the atomically thin limit, a large density of magnetic domains are found in 2 L and 3 L Fe_5GeTe_2, rather than a single domain state as observed in other vdW ferromagnets with large uniaxial anisotropy. Such layer-dependent domains imply intercompetition between uniaxial anisotropy energy (K_u) and demagnetization energy (K_d) in atomically

thin Fe_5GeTe_2, which is further corroborated by a finite IP magnetization component within 5 L compared to that of 6 L [22]. However, domain wall pinning is found to enhance H_c in atomically thin Fe_5GeTe_2 [30], meaning that the domains previously described could simply be pinned domains. Nevertheless, an explicit layer dependence of the magnetic domain structure in the demagnetized state, as well as a limited density of pinning sites revealed by NVSM [30] suggest that the layer dependent domain structures which were observed in the XPEEM measurements [22] originate from changes in the relative contributions from K_u and K_d. More importantly, the results motivate further investigation of magnetic textures beyond conventional single domains in atomically thin vdW materials.

Chapter 6 discusses easy-plane ferromagnetism and vortex-antivortex spin textures in atomically thin Fe_5GeTe_2. Counterintuitively, there is no magnetic phase transition for the 2D XY model, for which the magnetization is constrained to lie within the xy plane [18]. Instead, bound pairs of vortices and antivortices are predicted to form below a finite temperature [18, 19]. A vdW ferromagnet with easy-plane anisotropy is an ideal candidate material to test for these vortex-antivortex pairs, as proposed by Berezenskii [18], Kosterlitz and Thouless [19]. In detail, bulk Fe_5GeTe_2 crystals were quenched in ice water directly from the growth temperature of 1023 K, and were subsequently cooled below 100 K. The combination of these steps induces a magnetostructural transition, resulting in an enhanced T_C of 310 K [46]. Magnetic domains with easy-plane anisotropy were observed in 4 L of Fe_5GeTe_2. Moreover, magnetic vortices and antivortices were observed. Several proposals call for ferromagnetic vortices to be interfaced with their superconducting analogues, for which the binding between a ferromagnetic vortex and superconducting vortex is energetically favorable and could host the Majorana bound state [26]. In this regard, $NbSe_2$, a vdW superconductor [162, 163], could be interfaced with atomically thin Fe_5GeTe_2 to test the possibility of stabilizing Majorana bound states in hybrid ferromagnet-superconductor heterostructures.

7.2 Outlook and perspective

Broadly speaking, this thesis demonstrates the stabilization and modulation of ferromagnetic domain structures in atomically thin 2D vdW materials. In detail, this thesis demonstrates that it may be possible to tune or stabilize ferromagnetic domain structures with varying properties. The main findings of this thesis, as well as potential perspectives, are outlined below:

- Chapter 3: X-ray spectroscopy of atomically thin $CrSiTe_3$
  - Summary: XAS and XMCD spectroscopy was performed by Ryuji Fujita, Dr. Jieyi Liu, and Dr. Javier Herrero-Martín at BOREAS BL29 at ALBA Synchrotron. The exfoliated samples were synthesized by Ryuji Fujita. The bulk parent crystals were synthesized by Xiaofei Hou and Prof. Yanfeng Guo. The results were analyzed by Ryuji Fujita, Prof. Gerrit van der Laan and Prof. Thorsten Hesjedal.
  - Results: the magnetic spin moment (m_s) and magnetic orbital moment (m_l) was estimated as a function of thickness in atomically thin $CrSiTe_3$ with XAS and XMCD spectroscopy. Signs of an enhanced hybridizations were found for 10 L and below.
  - Outlook: the enhanced hybridization in the few-layer limit should also be evaluated for other vdW ferromagnets, including $CrGeTe_3$ and Fe_3GeTe_2.
- Chapter 4: Strained ferromagnetism at a Fe_3GeTe_2/α-In_2Se_3 heterojunction
  - Summary: XPEEM imaging of Fe_3GeTe_2/α-In_2Se_3 heterostructures were performed by Ryuji Fujita, Dr. Mohamad A. Mawass, Dr. Alevtina Smekhova and Dr. Florian Kronast at the UE49-PGMa beamline at BESSY II. Additional XPEEM measurements were performed by Ryuji Fujita, Dr. Angadjit Singh, Emily Heppell, Dr. Dirk Backes and Dr. Francesco Maccherozzi at the I06 beamline at Diamond Light Source. Density functional theory calculations were performed by Dr. Gautam Gurung at Trinity College, Oxford. The exfoliated sample was

synthesized by Ryuji Fujita. The bulk parent crystals were synthesized by Dr. Daniel Mayoh and Prof. Geetha Balakrishnan at the University of Warwick, and by Dr. Kenji Watanabe and Dr. Takashi Taniguchi at the National Institute for Materials Science. The results were analyzed by Ryuji Fujita, Dr. Gautam Gurung, Prof. Gerrit van der Laan and Prof. Thorsten Hesjedal.

  - Results: the ferromagnetic domain structure of Fe_3GeTe_2 was characterized with XPEEM. In particular, it was found that interfacial coupling with α-In_2Se_3 alters the domain structure and reduces T_C. Raman spectroscopy reveals the presence of interfacial strain in both Fe_3GeTe_2/α-In_2Se_3 and graphite/α-In_2Se_3 heterostructures.

  - Outlook: A poling voltage should be applied to the α-In_2Se_3 layer to see if it is possible to control the ferromagnetic by electrical means. This should be simultaneously evaluated with an imaging method, such as XPEEM or NV magnetometry, and Raman microscopy.

- Chapter 5: Layer-dependent magnetic domains in atomically thin Fe_5GeTe_2

  - Summary: XPEEM imaging of atomically thin Fe_5GeTe_2 was performed by Ryuji Fujita, Dr. Mohamad A. Mawass and Dr. Florian Kronast at UE49-PGMa at BESSY II. Micromagnetic simulations were performed by Pedram Bassirian at Oxford. The exfoliated samples were synthesized by Ryuji Fujita. The bulk parent crystals were synthesized by Dr. Zhengxian Li and Prof. Yanfeng Guo at ShanghaiTech University. The results were analyzed by Ryuji Fujita, Prof. Gerrit van der Laan and Prof. Thorsten Hesjedal.

  - Results: ferromagnetic domains, instead of a spatially homogenous magnetization, were observed in few-layer Fe_5GeTe_2 with XPEEM. Moreover, the domain structure was found to depend on the number of layers. Domain wall pinning and Bloch-type domain walls were confirmed with NV magnetometry.

  - Outlook: it remains unclear whether the bubble domains observed in

few-layer Fe_5GeTe_2 are skyrmions. More exfoliated flakes produced from furnace-cooled Fe_5GeTe_2 should be characterized to evaluate the reproducibility and domain wall profile of the bubble domains.

- Chapter 6: Vortex-antivortex pairs in atomically thin Fe_5GeTe_2
  - Summary: XPEEM imaging of few-layer Fe_5GeTe_2 was performed by Ryuji Fujita, Jheng-Cyuan Lin, Dr. Alevtina Smekhova and Dr. Florian Kronast at UE49-PGMa at BESSY II. The exfoliated samples were synthesized by Ryuji Fujita. The bulk parent crystals were synthesized by Dr. Andrew May at Oak Ridge National Laboratory. The results were analyzed by Ryuji Fujita, Jheng-Cyuan Lin, Prof. Gerrit van der Laan and Prof. Thorsten Hesjedal.
  - Results: the magnetization of 4 L Fe_5GeTe_2 was characterized with XPEEM at a temperature of 50 K. The sample was produced from Fe_5GeTe_2 synthesized with the quench-cool protocol [46]. The presence of planar magnetic domains, vortices and antivortices was confirmed.
  - Outlook: the vortices and antivortices may be merons and antimerons, which have a core polarized in the out-of-plane direction. This should be confirmed by characterizing the magnetization profile with XPEEM and NV magnetometry.

The findings of this thesis will lead to future investigations, including the implementation of α-In_2Se_3 in ferromagnetic MTJs, the further characterization of topological properties of vortex-antivortex pairs in Fe_5GeTe_2 and eventual incorporation of Fe_5GeTe_2 in hybrid ferromagnet-superconductor heterostructures, which may host Majorana bound states which are necessary for topological quantum devices.

Bibliography

(1) Novoselov, K.; Geim, A.; Morozov, S.; Jiang, D.; Zhang, Y.; Dubonos, S.; Grigorieva, I.; Firsov, A. Electric Field Effect in Atomically Thin Carbon Films. *Science* **2004**, *306*, 666–669.

(2) Mak, K. F.; Lee, C.; Hone, J.; Shan, J.; Heinz, T. F. Atomically Thin MoS_2: A New Direct-Gap Semiconductor. *Phys. Rev. Lett.* **2010**, *105*, 136805.

(3) Tang, S. et al. Quantum spin Hall state in monolayer 1T'-WTe_2. *Nat. Phys.* **2017**, *13*, 683–687.

(4) Mermin, N. D.; Wagner, H. Absence of Ferromagnetism or Antiferromagnetism in One- or Two-Dimensional Isotropic Heisenberg Models. *Phys. Rev. Lett.* **1966**, *17*, 1133–1136.

(5) Klein, M. J.; Smith, R. S. Thin Ferromagnetic Films. *Phys. Rev.* **1951**, *81*, 378–380.

(6) Huang, B.; Clark, G.; Navarro-Moratalla, E.; Klein, D. R.; Cheng, R.; Seyler, K. L.; Zhong, D.; Schmidgall, E.; McGuire, M. A.; Cobden, D. H.; Yao, W.; Xiao, D.; Jarillo-Herrero, P.; Xu, X. Layer-dependent ferromagnetism in a van der Waals crystal down to the monolayer limit. *Nature* **2017**, *546*, 270–273.

(7) Gong, C.; Li, L.; Li, Z.; Ji, H.; Stern, A.; Xia, Y.; Cao, T.; Bao, W.; Wang, C.; Wang, Y.; Qiu, Z. Q.; Cava, R. J.; Louie, S. G.; Xia, J.; Zhang, X. Discovery of intrinsic ferromagnetism in two-dimensional van der Waals crystals. *Nature* **2017**, *546*, 265–269.

(8) Fei, Z.; Huang, B.; Malinowski, P.; Wang, W.; Song, T.; Sanchez, J.; Yao, W.; Xiao, D.; Zhu, X.; May, A. F.; Wu, W.; Cobden, D. H.; Chu, J. H.; Xu, X. Two-dimensional itinerant ferromagnetism in atomically thin Fe_3GeTe_2. *Nat. Mater.* **2018**, *17*, 778–782.

(9) An, J.; Zhao, X.; Zhang, Y.; Liu, M.; Yuan, J.; Sun, X.; Zhang, Z.; Wang, B.; Li, S.; Li, D. Perspectives of 2D Materials for Optoelectronic Integration. *Adv. Funct. Mater.* **2022**, *32*, 2110119.

(10) Wang, S.; Liu, X.; Xu, M.; Liu, L.; Yang, D.; Zhou, P. Two-dimensional devices and integration towards the silicon lines. *Nat. Mater.* **2022**, *21*, 1225–1239.

(11) Song, T.; Sun, Q.-C.; Anderson, E.; Wang, C.; Qian, J.; Taniguchi, T.; Watanabe, K.; McGuire, M. A.; Stöhr, R.; Xiao, D.; Cao, T.; Wrachtrup, J.; Xu, X. Direct visualization of magnetic domains and moiré magnetism in twisted 2D magnets. *Science* **2021**, *374*, 1140–1144.

(12) Zhong, D.; Seyler, K. L.; Linpeng, X.; Wilson, N. P.; Taniguchi, T.; Watanabe, K.; McGuire, M. A.; Fu, K.-M. C.; Xiao, D.; Yao, W.; Xu, X. Layer-resolved magnetic proximity effect in van der Waals heterostructures. *Nat. Nano.* **2020**, *15*, 187–191.

(13) Cao, Y.; Fatemi, V.; Fang, S.; Watanabe, K.; Taniguchi, T.; Kaxiras, E.; Jarillo-Herrero, P. Unconventional superconductivity in magic-angle graphene superlattices. *Nature* **2018**, *556*, 43–50.

(14) Sharpe, A. L.; Fox, E. J.; Barnard, A. W.; Finney, J.; Watanabe, K.; Taniguchi, T.; Kastner, M. A.; Goldhaber-Gordon, D. Emergent ferromagnetism near three-quarters filling in twisted bilayer graphene. *Science* **2019**, *365*, 605–608.

(15) Klein, D. R.; Xia, L.-Q.; MacNeill, D.; Watanabe, K.; Taniguchi, T.; Jarillo-Herrero, P. Electrical switching of a bistable moiré superconductor. *Nat. Nano.* **2023**, *18*, 331–335.

(16) Min, K.-H.; Lee, D. H.; Choi, S.-J.; Lee, I.-H.; Seo, J.; Kim, D. W.; Ko, K.-T.; Watanabe, K.; Taniguchi, T.; Ha, D. H.; Kim, C.; Shim, J. H.; Eom, J.; Kim, J. S.; Jung, S. Tunable spin injection and detection across a van der Waals interface. *Nat. Mater.* **2022**, *21*, 1144–1149.

(17) Deng, Y.; Yu, Y.; Song, Y.; Zhang, J.; Wang, N. Z.; Sun, Z.; Yi, Y.; Wu, Y. Z.; Wu, S.; Zhu, J.; Wang, J.; Chen, X. H.; Zhang, Y. Gate-tunable room-temperature ferromagnetism in two-dimensional Fe_3GeTe_2. *Nature* **2018**, *563*, 94–99.

(18) Berezinskii, V. Destruction of long-range order in one-dimensional and two-dimensional systems possessing a continous symmetry group. II. quantum systems. *J. Exp. Theor. Phys* **1972**, *34*, 1144–1156.

(19) Kosterlitz, J. M.; Thouless, D. J. Ordering, metastability and phase transitions in two-dimensional systems. *J. Phys. C: Solid State Phys.* **1973**, *6*, 1181.

(20) Casas, B. W.; Li, Y.; Moon, A.; Xin, Y.; McKeever, C.; Macy, J.; Petford-Long, A. K.; Phatak, C. M.; Santos, E. J. G.; Choi, E. S.; Balicas, L. Coexistence of Merons with Skyrmions in the Centrosymmetric van der Waals Ferromagnet $Fe_{5-x}GeTe_2$. *Adv. Mater.* **2023**, *35*, 2212087.

(21) Hubert, A.; Schäfer, R., *Magnetic Domains: The Analysis of Magnetic Microstructures*, 1st ed.; Springer-Verlag: Berlin, 1998.

(22) Fujita, R.; Bassirian, P.; Li, Z.; Guo, Y.; Mawass, M. A.; Kronast, F.; Van Der Laan, G.; Hesjedal, T. Layer-Dependent Magnetic Domains in Atomically Thin Fe_5GeTe_2. *ACS Nano* **2022**, *16*, 10545–10553.

(23) Yang, M. et al. Creation of skyrmions in van der Waals ferromagnet Fe_3GeTe_2 on $(Co/Pd)_n$ superlattice. *Sci. Adv.* **2020**, *6*.

(24) Wang, Z.; Sapkota, D.; Taniguchi, T.; Watanabe, K.; Mandrus, D.; Morpurgo, A. F. Tunneling Spin Valves Based on Fe_3GeTe_2/hBN/Fe_3GeTe_2 van der Waals Heterostructures. *Nano Lett.* **2018**, *18*, 4303–4308.

(25) Zhang, K.; Han, S.; Lee, Y.; Coak, M. J.; Kim, J.; Hwang, I.; Son, S.; Shin, J.; Lim, M.; Jo, D.; Kim, K.; Kim, D.; Lee, H.-W.; Park, J.-G. Gigantic Current Control of Coercive Field and Magnetic Memory Based on Nanometer-Thin Ferromagnetic van der Waals Fe_3GeTe_2. *Adv. Mater.* **2021**, *33*, 2004110.

(26) Pathak, V.; Dasgupta, S.; Franz, M. Majorana zero modes in a magnetic and superconducting hybrid vortex. *Phys. Rev. B* **2022**, *106*, 224518.

(27) Jenkins, S.; Rózsa, L.; Atxitia, U.; Evans, R. F. L.; Novoselov, K. S.; Santos, E. J. G. Breaking through the Mermin-Wagner limit in 2D van der Waals magnets. *Nat. Commun.* **2022**, *13*, 6917.

(28) Blundell, S., *Magnetism in Condensed Matter*; Adlung, S., Ed.; Oxford University Press: 2001.

(29) Kittel, C., *Introduction to Solid State Physics*; Johnson, S., Ed.; John Wiley & Sons, Inc.: 2005.

(30) Högen, M.; Fujita, R.; Tan, A. K. C.; Geim, A.; Pitts, M.; Li, Z.; Guo, Y.; Stefan, L.; Hesjedal, T.; Atatüre, M. Imaging Nucleation and Propagation of Pinned Domains in Few-Layer $Fe_{5-x}GeTe_2$. *ACS Nano* **2023**, *17*, 16879–16885.

(31) Persky, E.; Sochnikov, I.; Kalisky, B. Studying Quantum Materials with Scanning SQUID Microscopy. *Ann. Rev. Condens. Matter Phys.* **2022**, *13*, 385–405.

(32) Paul, A., *Low-Angle Polarized Neutron and X-ray Scattering from Magnetic Nanolayers and Nanostructures*; Chen, Y., Ed.; Springer: 2017; Vol. 273.

(33) Ghidini, M.; Maccherozzi, F.; Dhesi, S. S.; Mathur, N. D. XPEEM and MFM Imaging of Ferroic Materials. *Adv. Electron. Mater.* **2022**, *8*, 2200162.

(34) Casola, F.; van der Sar, T.; Yacoby, A. Probing condensed matter physics with magnetometry based on nitrogen-vacancy centres in diamond. *Nat. Rev. Mater.* **2018**, *3*, 17088.

(35) Deng, Y.; Xiang, Z.; Lei, B.; Zhu, K.; Mu, H.; Zhuo, W.; Hua, X.; Wang, M.; Wang, Z.; Wang, G.; Tian, M.; Chen, X. Layer-Number-Dependent Magnetism and Anomalous Hall Effect in van der Waals Ferromagnet Fe_5GeTe_2. *Nano Lett.* **2022**, *22*, 9839–9846.

(36) Pizzocchero, F.; Gammelgaard, L.; Jessen, B. S.; Caridad, J. M.; Wang, L.; Hone, J.; Bøggild, P.; Booth, T. J. The hot pick-up technique for batch assembly of van der Waals heterostructures. *Nat. Commun.* **2016**, *7*, 11894.

(37) Frisenda, R.; Navarro-Moratalla, E.; Gant, P.; Pérez De Lara, D.; Jarillo-Herrero, P.; Gorbachev, R. V.; Castellanos-Gomez, A. Recent progress in the assembly of nanodevices and van der Waals heterostructures by deterministic placement of 2D materials. *Chem. Soc. Rev.* **2018**, *47*, 53–68.

(38) Purdie, D. G.; Pugno, N. M.; Taniguchi, T.; Watanabe, K.; Ferrari, A. C.; Lombardo, A. Cleaning interfaces in layered materials heterostructures. *Nat. Commun.* **2018**, *9*, 5387.

(39) Huang, Y. et al. Universal mechanical exfoliation of large-area 2D crystals. *Nat. Commun.* **2020**, *11*, 2453.

(40) Shcherbakov, D.; Stepanov, P.; Weber, D.; Wang, Y.; Hu, J.; Zhu, Y.; Watanabe, K.; Taniguchi, T.; Mao, Z.; Windl, W.; Goldberger, J.; Bockrath, M.; Lau, C. N. Raman Spectroscopy, Photocatalytic Degradation, and Stabilization of Atomically Thin Chromium Tri-iodide. *Nano Lett.* **2018**, *18*, 4214–4219.

(41) Wu, Y.; Wu, Y.; Kang, K.; Chen, Y.; Li, Y.; Chen, T.; Xu, Y. Characterization of CVD graphene permittivity and conductivity in micro-/millimeter wave frequency range. *AIP Adv.* **2016**, *6*, 095014.

(42) Gorbachev, R. V.; Riaz, I.; Nair, R. R.; Jalil, R.; Britnell, L.; Belle, B. D.; Hill, E. W.; Novoselov, K. S.; Watanabe, K.; Taniguchi, T.; Geim, A. K.; Blake, P. Hunting for Monolayer Boron Nitride: Optical and Raman Signatures. *Small* **2011**, *7*, 465–468.

(43) Liu, X.; Chiu, C.-L.; Lee, J. Y.; Farahi, G.; Watanabe, K.; Taniguchi, T.; Vishwanath, A.; Yazdani, A. Spectroscopy of a tunable moiré system with a correlated and topological flat band. *Nat. Commun.* **2021**, *12*, 2732.

(44) Xu, R.; Guo, J.; Mi, S.; Wen, H.; Pang, F.; Ji, W.; Cheng, Z. Advanced atomic force microscopies and their applications in two-dimensional materials: a review. *Mater. Futures* **2022**, *1*, 032302.

(45) Zhang, H.; Huang, J.; Wang, Y.; Liu, R.; Huai, X.; Jiang, J.; Anfuso, C. Atomic force microscopy for two-dimensional materials: A tutorial review. *Opt. Commun.* **2018**, *406*, 3–17.

(46) May, A. F.; Ovchinnikov, D.; Zheng, Q.; Hermann, R.; Calder, S.; Huang, B.; Fei, Z.; Liu, Y.; Xu, X.; McGuire, M. A. Ferromagnetism Near Room Temperature in the Cleavable van der Waals Crystal Fe_5GeTe_2. *ACS Nano* **2019**, *13*, 4436–4442.

(47) Hui, Y. Y.; Liu, X.; Jie, W.; Chan, N. Y.; Hao, J.; Hsu, Y.-T.; Li, L.-J.; Guo, W.; Lau, S. P. Exceptional Tunability of Band Energy in a Compressively Strained Trilayer MoS_2 Sheet. *ACS Nano* **2013**, *7*, 7126–7131.

(48) Han, W. et al. Phase-controllable large-area two-dimensional In_2Se_3 and ferroelectric heterophase junction. *Nat. Nano.* **2023**, *18*, 55–63.

(49) McCreary, A. et al. Distinct magneto-Raman signatures of spin-flip phase transitions in CrI_3. *Nat. Commun.* **2020**, *11*, 3879.

(50) Velický, M.; Rodriguez, A.; Bouša, M.; Krayev, A. V.; Vondráček, M.; Honolka, J.; Ahmadi, M.; Donnelly, G. E.; Huang, F.; Abruña, H. D.; Novoselov, K. S.; Frank, O. Strain and Charge Doping Fingerprints of the Strong Interaction between Monolayer MoS_2 and Gold. *J. Phys. Chem. Lett.* **2020**, *11*, 6112–6118.

(51) Ferrari, A. C.; Basko, D. M. Raman spectroscopy as a versatile tool for studying the properties of graphene. *Nat. Nano.* **2013**, *8*, 235–246.

(52) Figueroa, A. I., *Magnetic Nanoparticles: A Study by Synchrotron Radiaition and RF Transverse Susceptibility*; Lahee, A., Ed.; Springer: 2015.

(53) Carra, P.; Thole, B. T.; Altarelli, M.; Wang, X. X-ray circular dichroism and local magnetic fields. *Phys. Rev. Lett.* **1993**, *70*, 694–697.

(54) Thole, B. T.; Carra, P.; Sette, F.; van der Laan, G. X-ray circular dichroism as a probe of orbital magnetization. *Phys. Rev. Lett.* **1992**, *68*, 1943–1946.

(55) Chen, C. T.; Idzerda, Y. U.; Lin, H.; Smith, N. V.; Meigs, G.; Chaban, E.; Ho, G. H.; Pellegrin, E.; Sette, F. Experimental Confirmation of the X-Ray Magnetic Circular Dichroism Sum Rules for Iron and Cobalt. *Phys. Rev. Lett.* **1995**, *75*, 152–155.

(56) Sander, A.; Orfila, G.; Sanchez-Manzano, D.; Reyren, N.; Mawass, M. A.; Gallego, F.; Collin, S.; Bouzehouane, K.; Höflich, K.; Kronast, F.; Grilli, F.; Rivera-Calzada, A.; Santamaria, J.; Villegas, J. E.; Valencia, S. Superconducting imprint of magnetic textures in ferromagnets with perpendicular magnetic anisotropy. *Sci. Rep.* **2021**, *11*, 20788.

(57) Grinolds, M. S.; Warner, M.; De Greve, K.; Dovzhenko, Y.; Thiel, L.; Walsworth, R. L.; Hong, S.; Maletinsky, P.; Yacoby, A. Subnanometre resolution in three-dimensional magnetic resonance imaging of individual dark spins. *Nat. Nano.* **2014**, *9*, 279–284.

(58) Tetienne, J. et al. The nature of domain walls in ultrathin ferromagnets revealed by scanning nanomagnetometry. *Nat. Commun.* **2015**, *6*, 6733.

(59) Ku, M. J. H. et al. Imaging viscous flow of the Dirac fluid in graphene. *Nature* **2020**, *583*, 537–541.

(60) Scholten, S. C.; Healey, A. J.; Robertson, I. O.; Abrahams, G. J.; Broadway, D. A.; Tetienne, J.-P. Widefield quantum microscopy with nitrogen-vacancy centers in diamond: Strengths, limitations, and prospects. *J. Appl. Phys.* **2021**, *130*, 150902.

(61) Zhang, J.; Cai, X.; Xia, W.; Liang, A.; Huang, J.; Wang, C.; Yang, L.; Yuan, H.; Chen, Y.; Zhang, S.; Guo, Y.; Liu, Z.; Li, G. Unveiling Electronic Correlation and the Ferromagnetic Superexchange Mechanism in the van der Waals Crystal $CrSiTe_3$. *Phys. Rev. Lett.* **2019**, *123*, 047203.

(62) Lin, G. T.; Zhuang, H. L.; Luo, X.; Liu, B. J.; Chen, F. C.; Yan, J.; Sun, Y.; Zhou, J.; Lu, W. J.; Tong, P.; Sheng, Z. G.; Qu, Z.; Song, W. H.; Zhu, X. B.; Sun, Y. P. Tricritical behavior of the two-dimensional intrinsically ferromagnetic semiconductor $CrGeTe_3$. *Phys. Rev. B.* **2017**, *95*, 245212.

(63) Liu, B.; Zou, Y.; Zhang, L.; Zhou, S.; Wang, Z.; Wang, W.; Qu, Z.; Zhang, Y. Critical behavior of the quasi-two-dimensional semiconducting ferromagnet $CrSiTe_3$. *Sci. Rep.* **2016**, *6*, 33873.

(64) Williams, T. J.; Aczel, A. A.; Lumsden, M. D.; Nagler, S. E.; Stone, M. B.; Yan, J.-Q.; Mandrus, D. Magnetic correlations in the quasi-two-dimensional semiconducting ferromagnet $CrSiTe_3$. *Phys. Rev. B* **2015**, *92*, 144404.

(65) Fujita, R.; Liu, J.; Hou, X.; Guo, Y.; Herrero-Martín, J.; van der Laan, G.; Hesjedal, T. X-ray spectroscopy for the magnetic study of the van der Waals ferromagnet $CrSiTe_3$ in the few- and monolayer limit. *2D Mater.* **2022**, *9*, 045007.

(66) Van der Laan, G.; Figueroa, A. I. X-ray magnetic circular dichroism–A versatile tool to study magnetism. *Coord. Chem. Rev.* **2014**, *277-278*, 95–129.

(67) Van der Laan, G. Angular momentum sum rules for x-ray absorption. *Phys. Rev. B* **1998**, *57*, 112–115.

(68) Figueroa, A. I.; van der Laan, G.; Collins-McIntyre, L. J.; Zhang, S.-L.; Baker, A. A.; Harrison, S. E.; Schönherr, P.; Cibin, G.; Hesjedal, T. Magnetic Cr doping of Bi_2Se_3: Evidence for divalent Cr from x-ray spectroscopy. *Phys. Rev. B* **2014**, *90*, 134402.

(69) Lin, M.-W.; Zhuang, H. L.; Yan, J.; Ward, T. Z.; Puretzky, A. A.; Rouleau, C. M.; Gai, Z.; Liang, L.; Meunier, V.; Sumpter, B. G.; Ganesh, P.; Kent, P. R. C.; Geohegan, D. B.; Mandrus, D. G.; Xiao, K. Ultrathin nanosheets of $CrSiTe_3$: a semiconducting two-dimensional ferromagnetic material. *J. Mater. Chem. C* **2016**, *4*, 315–322.

(70) Watson, M. D.; Marković, I.; Mazzola, F.; Rajan, A.; Morales, E. A.; Burn, D. M.; Hesjedal, T.; van der Laan, G.; Mukherjee, S.; Kim, T. K.; Bigi, C.; Vobornik, I.; Ciomaga Hatnean, M.; Balakrishnan, G.; King, P. D. C. Direct observation of the energy gain underpinning ferromagnetic superex-

change in the electronic structure of $CrGeTe_3$. *Phys. Rev. B* **2020**, *101*, 205125.

(71) Zhang, C.; Wang, L.; Gu, Y.; Zhang, X.; Xia, X.; Jiang, S.; Huang, L.-L.; Fu, Y.; Liu, C.; Lin, J.; Zou, X.; Su, H.; Mei, J.-W.; Dai, J.-F. Hard ferromagnetic behavior in atomically thin $CrSiTe_3$ flakes. *Nanoscale* **2022**, *14*, 5851–5858.

(72) Dudzik, E.; Dürr, H. A.; Dhesi, S. S.; van der Laan, G.; Knabben, D.; Goedkoop, J. B. Magnetic properties of self-assembled Co clusters on Au(111) below the ferromagnetic phase transition. *J. Condens. Matter Phys.* **1999**, *11*, 8445.

(73) Morgan, J. D. I.; Kutzelnigg, W. Hund's rules, the alternating rule, and symmetry holes. *J. Phys. Chem.* **1993**, *97*, 2425–2434.

(74) Sun, Z. et al. Giant nonreciprocal second-harmonic generation from antiferromagnetic bilayer CrI_3. *Nature* **2019**, *572*, 497–501.

(75) Johansen, Ø.; Risinggård, V.; Sudbø, A.; Linder, J.; Brataas, A. Current Control of Magnetism in Two-Dimensional Fe_3GeTe_2. *Phys. Rev. Lett.* **2019**, *122*, 217203.

(76) Sun, Q. C.; Song, T.; Anderson, E.; Brunner, A.; Förster, J.; Shalomayeva, T.; Taniguchi, T.; Watanabe, K.; Gräfe, J.; Stöhr, R.; Xu, X.; Wrachtrup, J. Magnetic domains and domain wall pinning in atomically thin $CrBr_3$ revealed by nanoscale imaging. *Nat. Commun.* **2021**, *12*, 1989.

(77) Zhang, X.; Wang, L.; Su, H.; Xia, X.; Liu, C.; Lyu, B.; Lin, J.; Huang, M.; Cheng, Y.; Mei, J.-W.; Dai, J.-F. Strain Tunability of Perpendicular Magnetic Anisotropy in van der Waals Ferromagnets VI_3. *Nano Lett.* **2022**, *22*, 9891–9899.

(78) Li, M.-Y.; Shi, Y.; Cheng, C.-C.; Lu, L.-S.; Lin, Y.-C.; Tang, H.-L.; Tsai, M.-L.; Chu, C.-W.; Wei, K.-H.; He, J.-H.; Chang, W.-H.; Suenaga, K.; Li, L.-J. Epitaxial growth of a monolayer WSe_2-MoS_2 lateral p-n junction with an atomically sharp interface. *Science* **2015**, *349*, 524–528.

(79) Liu, T.; Liu, S.; Tu, K.-H.; Schmidt, H.; Chu, L.; Xiang, D.; Martin, J.; Eda, G.; Ross, C. A.; Garaj, S. Crested two-dimensional transistors. *Nat. Nano.* **2019**, *14*, 223–226.

(80) Wang, Y.; Wang, C.; Liang, S.-J.; Ma, Z.; Xu, K.; Liu, X.; Zhang, L.; Admasu, A. S.; Cheong, S.-W.; Wang, L.; Chen, M.; Liu, Z.; Cheng, B.; Ji, W.; Miao,

F. Strain-Sensitive Magnetization Reversal of a van der Waals Magnet. *Adv. Mater.* **2020**, *32*, 2004533.

(81) Wang, H. et al. Above Room-Temperature Ferromagnetism in Wafer-Scale Two-Dimensional van der Waals Fe_3GeTe_2 Tailored by a Topological Insulator. *ACS Nano* **2020**, *14*, 10045–10053.

(82) Dang, N.-T.; Kozlenko, D. P.; Lis, O. N.; Kichanov, S. E.; Lukin, Y. V.; Golosova, N. O.; Savenko, B. N.; Duong, D.-L.; Phan, T.-L.; Tran, T.-A.; Phan, M.-H. High Pressure-Driven Magnetic Disorder and Structural Transformation in Fe_3GeTe_2: Emergence of a Magnetic Quantum Critical Point. *Adv. Sci.* **2023**, *10*, 2206842.

(83) Hu, X.; Zhao, Y.; Shen, X.; Krasheninnikov, A. V.; Chen, Z.; Sun, L. Enhanced Ferromagnetism and Tunable Magnetism in Fe_3GeTe_2 Monolayer by Strain Engineering. *ACS Appl. Mater. Interfaces* **2020**, *12*, 26367–26373.

(84) Zhou, Y.; Wu, D.; Zhu, Y.; Cho, Y.; He, Q.; Yang, X.; Herrera, K.; Chu, Z.; Han, Y.; Downer, M. C.; Peng, H.; Lai, K. Out-of-Plane Piezoelectricity and Ferroelectricity in Layered α-In_2Se_3 Nanoflakes. *Nano Lett.* **2017**, *17*, 5508–5513.

(85) Zhang, Y.; Shen, L.; Liu, M.; Li, X.; Lu, X.; Lu, L.; Ma, C.; You, C.; Chen, A.; Huang, C.; Chen, L.; Alexe, M.; Jia, C.-L. Flexible Quasi-Two-Dimensional $CoFe_2O_4$ Epitaxial Thin Films for Continuous Strain Tuning of Magnetic Properties. *ACS Nano* **2017**, *11*, 8002–8009.

(86) Xue, F.; Zhang, J.; Hu, W.; Hsu, W.-T.; Han, A.; Leung, S.-F.; Huang, J.-K.; Wan, Y.; Liu, S.; Zhang, J.; He, J.-H.; Chang, W.-H.; Wang, Z. L.; Zhang, X.; Li, L.-J. Multidirection Piezoelectricity in Mono- and Multilayered Hexagonal α-In_2Se_3. *ACS Nano* **2018**, *12*, 4976–4983.

(87) Novoselov, K. S.; Mishchenko, A.; Carvalho, A.; Castro Neto, A. H. 2D materials and van der Waals heterostructures. *Science* **2016**, *353*.

(88) Li, Z. et al. Efficient strain modulation of 2D materials via polymer encapsulation. *Nat. Commun.* **2020**, *11*, 1151.

(89) Frank, O.; Tsoukleri, G.; Parthenios, J.; Papagelis, K.; Riaz, I.; Jalil, R.; Novoselov, K. S.; Galiotis, C. Compression Behavior of Single-Layer Graphenes. *ACS Nano* **2010**, *4*, 3131–3138.

(90) Ni, Z. H.; Yu, T.; Lu, Y. H.; Wang, Y. Y.; Feng, Y. P.; Shen, Z. X. Uniaxial Strain on Graphene: Raman Spectroscopy Study and Band-Gap Opening. *ACS Nano* **2008**, *2*, 2301–2305.

(91) Yang, J.; Colen, J.; Liu, J.; Nguyen, M. C.; Chern, G.-W.; Louca, D. Elastic and electronic tuning of magnetoresistance in $MoTe_2$. *Sci. Adv.* **2017**, *3*, 4949.

(92) Mayoh, D. A.; Wood, G. D. A.; Holt, S. J. R.; Beckett, G.; Dekker, E. J. L.; Lees, M. R.; Balakrishnan, G. Effects of Fe Deficiency and Co Substitution in Polycrystalline and Single Crystals of Fe_3GeTe_2. *Crystal Growth & Design* **2021**, *21*, 6786–6792.

(93) Küpers, M.; Konze, P. M.; Meledin, A.; Mayer, J.; Englert, U.; Wuttig, M.; Dronskowski, R. Controlled Crystal Growth of Indium Selenide, In_2Se_3, and the Crystal Structures of α-In_2Se_3. *Inorg. Chem.* **2018**, *57*, 11775–11781.

(94) Neumayer, S. M.; Saremi, S.; Martin, L. W.; Collins, L.; Tselev, A.; Jesse, S.; Kalinin, S. V.; Balke, N. Piezoresponse amplitude and phase quantified for electromechanical characterization. *J. Appl. Phys.* **2020**, *128*, 171105.

(95) Hong, S. Single frequency vertical piezoresponse force microscopy. *J. Appl. Phys.* **2021**, *129*, 051101.

(96) Gruverman, A.; Alexe, M.; Meier, D. Piezoresponse force microscopy and nanoferroic phenomena. *Nat. Commun.* **2019**, *10*, 1661.

(97) Giannozzi, P. et al. QUANTUM ESPRESSO: a modular and open-source software project for quantum simulations of materials. *J. Condens. Matter Phys.* **2009**, *21*, 395502.

(98) Himmetoglu, B.; Floris, A.; de Gironcoli, S.; Cococcioni, M. Hubbard-corrected DFT energy functionals: The LDA+U description of correlated systems. *Int. J. Quantum Chem.* **2014**, *114*, 14–49.

(99) Huang, K.; Shao, D.-F.; Tsymbal, E. Y. Ferroelectric Control of Magnetic Skyrmions in Two-Dimensional van der Waals Heterostructures. *Nano Lett.* **2022**, *22*, PMID: 35380845, 3349–3355.

(100) Pizzi, G. et al. Wannier90 as a community code: new features and applications. *J. Condens. Matter Phys.* **2020**, *32*, 165902.

(101) He, X.; Helbig, N.; Verstraete, M. J.; Bousquet, E. TB2J: A python package for computing magnetic interaction parameters. *Comput. Phys. Commun.* **2021**, *264*, 107938.

(102) Evans, R. F. L.; Fan, W. J.; Chureemart, P.; Ostler, T. A.; Ellis, M. O. A.; Chantrell, R. W. Atomistic spin model simulations of magnetic nanomaterials. *J. Condens. Matter Phys.* **2014**, *26*, 103202.

(103) Kronast, F.; Molina, S. V. SPEEM: The photoemission microscope at the dedicated microfocus PGM beamline UE49-PGMa at BESSY II. *JLSRF* **2016**, *2*, A90.

(104) Si, M.; Saha, A. K.; Gao, S.; Qiu, G.; Qin, J.; Duan, Y.; Jian, J.; Niu, C.; Wang, H.; Wu, W.; Gupta, S. K.; Ye, P. D. A ferroelectric semiconductor field-effect transistor. *Nat. Electron.* **2019**, *2*, 580–586.

(105) Ielmini, D.; Wong, H. P. In-memory computing with resistive switching devices. *Nat. Electron.* **2018**, *1*, 333–343.

(106) Kim, S.-R.; Park, I. K.; Yoo, J.-G.; Seo, J.; Kim, J.-G.; Park, J.-H.; Kim, J. S.; Kim, K.; Lee, G.; Ko, K.-T. Role Of Orbital Bond and Local Magnetism In Fe_3GeTe_2 and Fe_4GeTe_2: Implication For Ultrathin Nano Devices. *ACS Appl. Nano Mater.* **2022**, *5*, 10341–10347.

(107) Yamagami, K. et al. Itinerant ferromagnetism mediated by giant spin polarization of the metallic ligand band in the van der Waals magnet Fe_5GeTe_2. *Phys. Rev. B* **2021**, *103*, L060403.

(108) Jekal, S. Exchange Interactions and Curie Temperature of Ce-Substituted $SmCo_5$. *Condens. Matter* **2019**, *4*, 11.

(109) Stoner, E. C.; Wohlfarth, E. P. A mechanism of magnetic hysteresis in heterogeneous alloys. *Phil. Trans. Royal Soc. Ser. A* **1948**, *240*, 599–642.

(110) Tuinstra, F.; Koenig, J. L. Raman Spectrum of Graphite. *J. Chem. Phys.* **2003**, *53*, 1126–1130.

(111) Cançado, L. G.; Jorio, A.; Ferreira, E. H. M.; Stavale, F.; Achete, C. A.; Capaz, R. B.; Moutinho, M. V. O.; Lombardo, A.; Kulmala, T. S.; Ferrari, A. C. Quantifying Defects in Graphene via Raman Spectroscopy at Different Excitation Energies. *Nano Lett.* **2011**, *11*, 3190–3196.

(112) Lucchese, M. M.; Stavale, F.; Ferreira, E. H. M.; Vilani, C.; Moutinho, M. V. O.; Capaz, R. B.; Achete, C. A.; Jorio, A. Quantifying ion-induced de-

fects and Raman relaxation length in graphene. *Carbon* **2010**, *48*, 1592–1597.

(113) Warner, J. H.; Margine, E. R.; Mukai, M.; Robertson, A. W.; Giustino, F.; Kirkland, A. I. Dislocation-Driven Deformations in Graphene. *Science* **2012**, *337*, 209–212.

(114) Kurasch, S.; Kotakoski, J.; Lehtinen, O.; Skákalová, V.; Smet, J.; Krill, C. E. I.; Krasheninnikov, A. V.; Kaiser, U. Atom-by-Atom Observation of Grain Boundary Migration in Graphene. *Nano Lett.* **2012**, *12*, 3168–3173.

(115) Androulidakis, C.; Koukaras, E. N.; Paterakis, G.; Trakakis, G.; Galiotis, C. Tunable macroscale structural superlubricity in two-layer graphene via strain engineering. *Nat. Commun.* **2020**, *11*, 1595.

(116) Song, Y.; Mandelli, D.; Hod, O.; Urbakh, M.; Ma, M.; Zheng, Q. Robust microscale superlubricity in graphite/hexagonal boron nitride layered heterojunctions. *Nat. Mater.* **2018**, *17*, 894–899.

(117) Du, L. et al. Lattice Dynamics, Phonon Chirality, and Spin-Phonon Coupling in 2D Itinerant Ferromagnet Fe_3GeTe_2. *Adv. Funct. Mater.* **2019**, *29*, 1904734.

(118) Wang, Z.-A.; Xue, W.; Yan, F.; Zhu, W.; Liu, Y.; Zhang, X.; Wei, Z.; Chang, K.; Yuan, Z.; Wang, K. Selectively Controlled Ferromagnets by Electric Fields in van der Waals Ferromagnetic Heterojunctions. *Nano Lett.* **2023**, *23*, 710–717.

(119) Li, Q.; Wang, Y.; Li, T.; Li, W.; Wang, F.; Janotti, A.; Law, S.; Gu, T. Localized Strain Measurement in Molecular Beam Epitaxially Grown Chalcogenide Thin Films by Micro-Raman Spectroscopy. *ACS Omega* **2020**, *5*, 8090–8096.

(120) Pak, S. et al. Strain-Mediated Interlayer Coupling Effects on the Excitonic Behaviors in an Epitaxially Grown MoS_2/WS_2 van der Waals Heterobilayer. *Nano Lett.* **2017**, *17*, 5634–5640.

(121) Han, E.; Nahid, S. M.; Rakib, T.; Nolan, G.; Ferrari, P. F.; Hossain, M. A.; Schleife, A.; Nam, S.; Ertekin, E.; van der Zande, A. M.; Huang, P. Y. Bend-Induced Ferroelectric Domain Walls in α-In_2Se_3. *ACS Nano* **2023**, *17*, 7881–7888.

(122) Cui, C. et al. Intercorrelated In-Plane and Out-of-Plane Ferroelectricity in Ultrathin Two-Dimensional Layered Semiconductor In_2Se_3. *Nano Lett.* **2018**, *18*, 1253–1258.

(123) Xiao, J.; Zhu, H.; Wang, Y.; Feng, W.; Hu, Y.; Dasgupta, A.; Han, Y.; Wang, Y.; Muller, D. A.; Martin, L. W.; Hu, P.; Zhang, X. Intrinsic Two-Dimensional Ferroelectricity with Dipole Locking. *Phys. Rev. Lett.* **2018**, *120*, 227601.

(124) Lisfi, A.; Williams, C. M.; Nguyen, L. T.; Lodder, J. C.; Coleman, A.; Corcoran, H.; Johnson, A.; Chang, P.; Kumar, A.; Morgan, W. Reorientation of magnetic anisotropy in epitaxial cobalt ferrite thin films. *Phys. Rev. B* **2007**, *76*, 054405.

(125) Yang, S.; Ren, X. Noncubic crystallographic symmetry of a cubic ferromagnet: Simultaneous structural change at the ferromagnetic transition. *Phys. Rev. B* **2008**, *77*, 014407.

(126) Callen, E. R.; Callen, H. B. Static Magnetoelastic Coupling in Cubic Crystals. *Phys. Rev.* **1963**, *129*, 578–593.

(127) Abes, M.; Koops, C. T.; Hrkac, S. B.; McCord, J.; Urs, N. O.; Wolff, N.; Kienle, L.; Ren, W. J.; Bouchenoire, L.; Murphy, B. M.; Magnussen, O. M. Domain structure and reorientation in $CoFe_2O_4$. *Phys. Rev. B* **2016**, *93*, 195427.

(128) Zhuang, H. L.; Kent, P. R. C.; Hennig, R. G. Strong anisotropy and magnetostriction in the two-dimensional Stoner ferromagnet Fe_3GeTe_2. *Phys. Rev. B* **2016**, *93*, 134407.

(129) Seo, J. et al. Nearly room temperature ferromagnetism in a magnetic metal-rich van der Waals metal. *Sci. Adv.* **2020**, *6*, 1–10.

(130) Li, Z.; Xia, W.; Su, H.; Yu, Z.; Fu, Y.; Chen, L.; Wang, X.; Yu, N.; Zou, Z.; Guo, Y. Magnetic critical behavior of the van der Waals Fe_5GeTe_2 crystal with near room temperature ferromagnetism. *Sci. Rep.* **2020**, *10*, 15345.

(131) Zhang, C. et al. Magnetic Skyrmions with Unconventional Helicity Polarization in a van der Waals Ferromagnet. *Adv. Mater.* **2022**, *34*, 2204163.

(132) Stahl, J.; Shlaen, E.; Johrendt, D. The van der Waals Ferromagnets $Fe_{5-\delta}GeTe_2$ and $Fe_{5-\delta-x}Ni_xGeTe_2$ - Crystal Structure, Stacking Faults, and Magnetic Properties. *Z. Anorg. Allg. Chem.* **2018**, *644*, 1923–1929.

(133) Li, Q. et al. Patterning-Induced Ferromagnetism of Fe_3GeTe_2 van der Waals Materials beyond Room Temperature. *Nano Lett.* **2018**, *18*, 5974–5980.

(134) Landau, L.; Lifshitz, E. On the theory of the dispersion of magnetic permeability in ferromagnetic bodies. *Phys. Z. Sowjetunion* **1935**, *8*, 153.

(135) Rhensius, J.; Vaz, C. A.; Bisig, A.; Schweitzer, S.; Heidler, J.; Körner, H. S.; Locatelli, A.; Niño, M. A.; Weigand, M.; Méchin, L.; Gaucher, F.; Goering, E.; Heyderman, L. J.; Kläui, M. Control of spin configuration in half-metallic $La_{0.7}Sr_{0.3}MnO_3$ nano-structures. *Appl. Phys. Lett.* **2011**, *99*, 062508.

(136) Yang, H.-H.; Bansal, N.; Rüßmann, P.; Hoffmann, M.; Zhang, L.; Go, D.; Li, Q.; Haghighirad, A.-A.; Sen, K.; Blügel, S.; Le Tacon, M.; Mokrousov, Y.; Wulfhekel, W. Magnetic domain walls of the van der Waals material Fe_3GeTe_2. *2D Mater.* **2022**, *9*, 025022.

(137) Schneider, C. M.; Schönhense, G. Investigating surface magnetism by means of photoexcitation electron emission microscopy. *Rep. Prog. Phys.* **2002**, *65*, 1785–1839.

(138) Lemerle, S.; Ferré, J.; Chappert, C.; Mathet, V.; Giamarchi, T.; Le Doussal, P. Domain wall creep in an ising ultrathin magnetic film. *Phys. Rev. Lett.* **1998**, *80*, 849–852.

(139) Buijnsters, F. J.; Ferreiros, Y.; Fasolino, A.; Katsnelson, M. I. Chirality-Dependent Transmission of Spin Waves through Domain Walls. *Phys. Rev. Lett.* **2016**, *116*, 147204.

(140) Dzyaloshinsky, I. A thermodynamic theory of "weak" ferromagnetism of antiferromagnetics. *J. Phys. Chem. Solids* **1958**, *4*, 241–255.

(141) Moriya, T. Anisotropic Superexchange Interaction and Weak Ferromagnetism. *Phys. Rev.* **1960**, *120*, 91–98.

(142) Park, T.-E. et al. Néel-type skyrmions and their current-induced motion in van der Waals ferromagnet-based heterostructures. *Phys. Rev. B* **2021**, *103*, 104410.

(143) Lv, H. et al. Large-Area Synthesis of Ferromagnetic $Fe_{5-x}GeTe_2$/Graphene van der Waals Heterostructures with Curie Temperature above Room Temperature. *Small* **2023**, *19*, 2302387.

(144) Ly, T. T. et al. Direct Observation of Fe-Ge Ordering in $Fe_{5-x}GeTe_2$ Crystals and Resultant Helimagnetism. *Adv. Funct. Mater.* **2021**, *31*, 2009758.

(145) Tang, M. et al. Continuous manipulation of magnetic anisotropy in a van der Waals ferromagnet via electrical gating. *Nat. Electron.* **2022**, *6*, 28–36.

(146) May, A. F.; Bridges, C. A.; McGuire, M. A. Physical properties and thermal stability of $Fe_{5-x}GeTe_2$ single crystals. *Phys. Rev. Mater.* **2019**, *3*, 104401.

(147) May, A. F.; Du, M.-H.; Cooper, V. R.; McGuire, M. A. Tuning magnetic order in the van der Waals metal Fe_5GeTe_2 by cobalt substitution. *Phys. Rev. Mater.* **2020**, *4*, 074008.

(148) Gao, Y.; Yin, Q.; Wang, Q.; Li, Z.; Cai, J.; Zhao, T.; Lei, H.; Wang, S.; Zhang, Y.; Shen, B. Spontaneous (Anti)meron Chains in the Domain Walls of van der Waals Ferromagnetic $Fe_{5-x}GeTe_2$. *Adv. Mater.* **2020**, *32*, 2005228.

(149) Cai, X.; Song, T.; Wilson, N. P.; Clark, G.; He, M.; Zhang, X.; Taniguchi, T.; Watanabe, K.; Yao, W.; Xiao, D.; McGuire, M. A.; Cobden, D. H.; Xu, X. Atomically Thin $CrCl_3$: An In-Plane Layered Antiferromagnetic Insulator. *Nano Lett.* **2019**, *19*, 3993–3998.

(150) Bedoya-Pinto, A.; Ji, J.-R.; Pandeya, A. K.; Gargiani, P.; Valvidares, M.; Sessi, P.; Taylor, J. M.; Radu, F.; Chang, K.; Parkin, S. S. P. Intrinsic 2D-XY ferromagnetism in a van der Waals monolayer. *Science* **2021**, *374*, 616–620.

(151) Shinjo, T.; Okuno, T.; Hassdorf, R.; Shigeto, K.; Ono, T. Magnetic Vortex Core Observation in Circular Dots of Permalloy. *Science* **2000**, *289*, 930–932.

(152) Wachowiak, A.; Wiebe, J.; Bode, M.; Pietzsch, O.; Morgenstern, M.; Wiesendanger, R. Direct Observation of Internal Spin Structure of Magnetic Vortex Cores. *Science* **2002**, *298*, 577–580.

(153) Mukai, N.; Leonov, A. O. Skyrmion and meron ordering in quasi-two-dimensional chiral magnets. *Phys. Rev. B* **2022**, *106*, 224428.

(154) Augustin, M.; Jenkins, S.; Evans, R. F. L.; Novoselov, K. S.; Santos, E. J. G. Properties and dynamics of meron topological spin textures in the two-dimensional magnet $CrCl_3$. *Nat. Commun.* **2021**, *12*, 185.

(155) Gao, N.; Je, S. G.; Im, M. Y.; Choi, J. W.; Yang, M.; Li, Q.; Wang, T. Y.; Lee, S.; Han, H. S.; Lee, K. S.; Chao, W.; Hwang, C.; Li, J.; Qiu, Z. Q. Creation and annihilation of topological meron pairs in in-plane magnetized films. *Nat. Commun.* **2019**, *10*, 5603.

(156) Rizzo, D. J.; McLeod, A. S.; Carnahan, C.; Telford, E. J.; Dismukes, A. H.; Wiscons, R. A.; Dong, Y.; Nuckolls, C.; Dean, C. R.; Pasupathy, A. N.; Roy, X.; Xiao, D.; Basov, D. N. Visualizing Atomically Layered Magnetism in CrSBr. *Adv. Mater.* **2022**, *34*, 2201000.

(157) Purbawati, A. et al. In-Plane Magnetic Domains and NÃ©el-like Domain Walls in Thin Flakes of the Room Temperature $CrTe_2$ Van der Waals Ferromagnet. *ACS Appl. Mater. Interfaces* **2020**, *12*, 30702–30710.

(158) Yu, X. Z.; Koshibae, W.; Tokunaga, Y.; Shibata, K.; Taguchi, Y.; Nagaosa, N.; Tokura, Y. Transformation between meron and skyrmion topological spin textures in a chiral magnet. *Nature* **2018**, *564*, 95–98.

(159) Wang, Z.; Su, Y.; Lin, S.-Z.; Batista, C. D. Meron, skyrmion, and vortex crystals in centrosymmetric tetragonal magnets. *Phys. Rev. B* **2021**, *103*, 104408.

(160) Das, S.; Hong, Z.; McCarter, M.; Shafer, P.; Shao, Y.-T.; Muller, D. A.; Martin, L. W.; Ramesh, R. A new era in ferroelectrics. *APL Mater.* **2020**, *8*, 120902.

(161) Bachmann, D.; Lianeris, M.; Komineas, S. Meron configurations in easy-plane chiral magnets. *Phys. Rev. B* **2023**, *108*, 014402.

(162) Hamill, A. et al. Two-fold symmetric superconductivity in few-layer $NbSe_2$. *Nat. Phys.* **2021**, *17*, 949–954.

(163) Xi, X.; Wang, Z.; Zhao, W.; Park, J.-H.; Law, K. T.; Berger, H.; Forró, L.; Shan, J.; Mak, K. F. Ising pairing in superconducting $NbSe_2$ atomic layers. *Nat. Phys.* **2016**, *12*, 139–143.